SANDIA REPORT
SAND96–2925 • UC–1303
Unlimited Release
Printed December 1996

Engineered Photocatalysts for Detoxification of Waste Water

Sabir A. Majumder, Michael R. Prairie, John A. Shelnutt,
Gail N. Ryba, James E. Miller, Terry J. Garino, Shahed U.M. Khan

Prepared by
Sandia National Laboratories
Albuquerque, New Mexico 87185 and Livermore, California 94550
for the United States Department of Energy
under Contract DE-AC04-94AL85000

Approved for public release; distribution is unlimited.

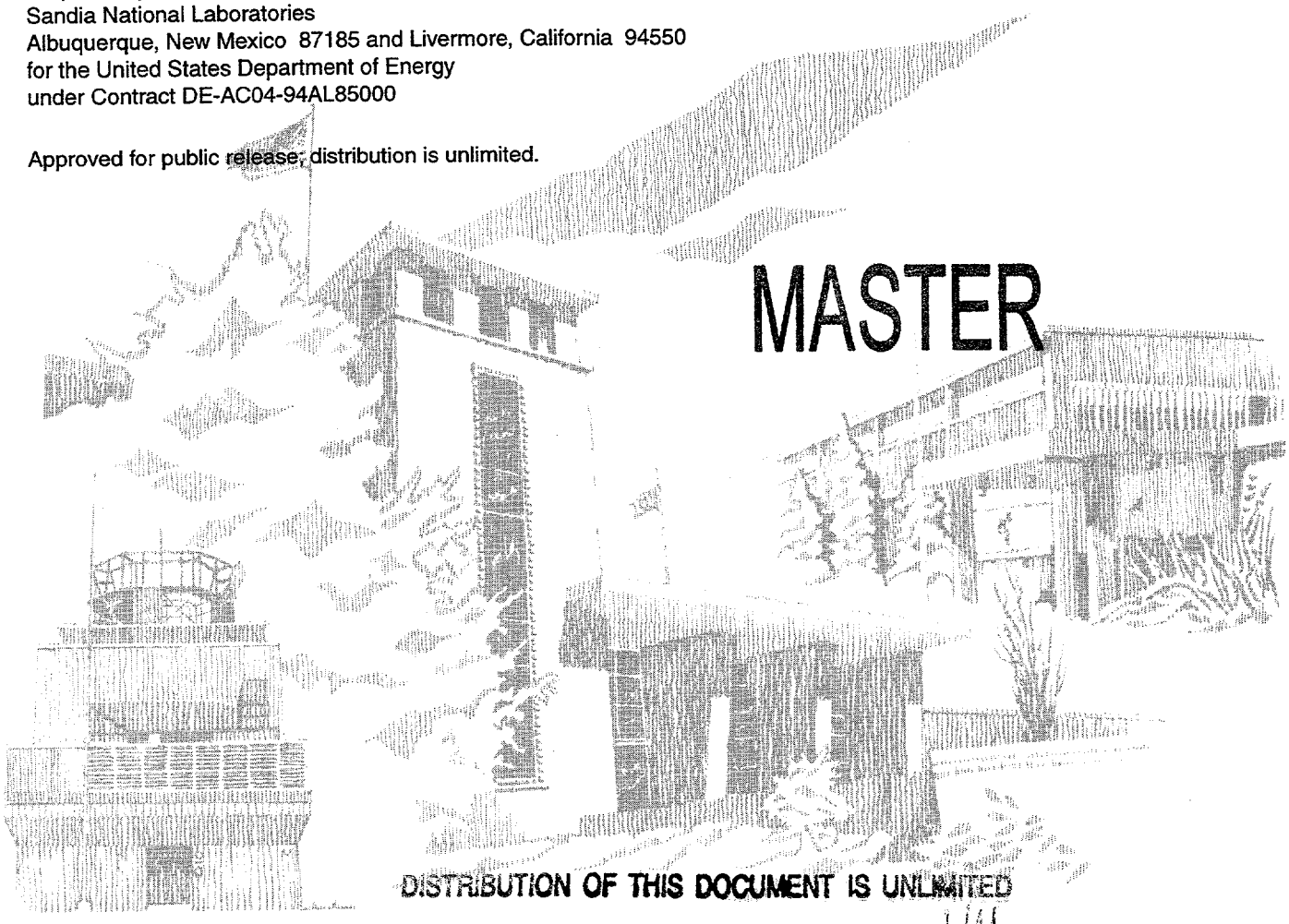

Issued by Sandia National Laboratories, operated for the United States Department of Energy by Sandia Corporation, a Lockheed Martin Company.

Available to DOE and DOE contractors from
Office of Scientific and Technical Information
PO Box 62
Oak Ridge, TN 37831

Prices available from (615) 576-8401, FTS 626-8401

Available to the public from
National Technical Information Service
US Department of Commerce
5285 Port Royal Rd
Springfield, VA 22161

NTIS price codes
Printed copy: A07
Microfiche copy: A01

SAND 96-2925
Unlimited Release
Printed December 1996

Distribution
Category UC-1303

Engineered Photocatalysts for Detoxification of Waste Water

Sabir A. Majumder and Michael R. Prairie
Solar Thermal Technology Department

John A. Shelnutt, Gail N. Ryba, and James E. Miller
Fuel Science Department

Terry J. Garino
Ceramic Processing Science Department

Sandia National Laboratories
Albuquerque, NM 87185

Shahed U.M. Khan,
Department of Chemistry and Biochemistry
Duquesne University, Pittsburgh, PA 15282

Abstract

This report describes progress on the development of engineered photocatalysts for the detoxification of water polluted with toxic organic compounds and heavy metals. We examined a range of different oxide supports (titania, alumina, magnesia and manganese dioxide) for tin uroporphyrin and investigated the efficacy of a few different porphyrins. A water-soluble octaacetic-acid-tetraphenylporphyrin and its derivatives have been synthesized and characterized in an attempt to design a porphyrin catalyst with a larger binding pocket. We have also investigated photocatalytic processes on both single crystal and powder forms of semiconducting SiC with an ultimate goal of developing a dual-semiconductor system combining TiO_2 and SiC. Mathematical modeling was also performed to identify parameters that can improve the efficiency of SiC-based photocatalytic systems. Although the conceptual TiO_2/SiC photodiode shows some promises for photoreduction processes, SiC itself was found to be an inefficient photocatalyst when combined with TiO_2. Alternative semiconductors with bandgap and band potentials similar to SiC should be tested in the future for further development and a practical utilization of the dual photodiode concept.

Intentionally Left Blank

Acknowledgments

This work was supported by the United States Department of Energy under Contract DE-AC04-94AL85000. Sandia is a multiprogram laboratory operated by Sandia Corporation, a Lockheed Martin Company, for the United States Department of Energy.

We also acknowledge the contributions made by Bradley D. Craig, Bertha M. Stange, Lindsey R. Evans, Sheryl L. Martinez, Thomas H. Madden, Aree Hanprasopwattana, Min Ruan, Steven K. Showalter, J. David Hobbs and Abhaya K. Datye at different phases of this three-year long Laboratory-Directed Research and Development (LDRD) project.

Summary

Solar detoxification provides an attractive new approach for the treatment of polluted water. The best available photodetoxification technology uses a titania (TiO_2) photocatalyst because it is active, robust, and non-toxic. Photogenerated electrons and holes lead to simultaneous oxidation and reduction, respectively, of the electroactive species. Unfortunately, titania absorbs only UV light. In order to utilize visible light, tin porphyrins (SnP) adsorbed onto semiconducting titania and non-conducting alumina (Al_2O_3) were investigated spectroscopically. SnP-modified titania shows enhanced ability to photocatalytically destroy two test compounds salicylic acid (SA) and aniline (AN). The presence of oxygen is a requirement in detoxification reactions independent of the nature of the supporting particles. The photodestruction of SA and AN was optimized using visible light, and with an optimal fractional coverage of tin uroporphyrin (SnUroP) on alumina of 0.3. The photolabile porphyrins in aqueous solution were found to be photostable on alumina in contrast to their rapid breakdown on titania. We also examined a range of other oxide supports like magnesia and manganese dioxide for testing photoactivity from SnUroP.

On the basis of our observations from the photocatalytic behaviors of SnUroP, we attempted to design biomimetic catalysts for isolation and detoxification of dilute toxic waste components; a water-soluble octaacetic-acid-tetraphenylporphyrin (OAATPP) and its derivatives, which absorb visible light and have a larger binding pocket, have been synthesized and characterized. Red shifts of 19-36 nm in the absorption bands of the newly synthesized nonplanar Ni-derivatives of OAATPP are noted when compared to planar NiTPP. Raman studies also indicate nonplanar conformations for NiOAATPP-series. At low pH (<3) or in 4.5-M NaCl,

conditions under which planar octaacidporphyrins (NiUroP) form π-π aggregates resulting in spectroscopic changes, NiOAATPP shows no such changes. The absence of π-π aggregation for NiOAATPP is attributed to the steric crowding from the peripheral substituents. For this OAATPP-series, axial ligand affinity is decreased by their nonplanarity and increased by electron-withdrawing substituents. The tin-derivative of OAATPP is yet to be synthesized for its potential application in solar detoxification of aqueous pollutants. However, they should be effective since tin porphyrins show reasonable excited state lifetimes which enables efficient electron transfer to the target molecules as opposed to short lifetimes of nickel derivatives.

In an attempt to engineer a photocatalyst that is more effective for the removal of heavy metals, we built and tested a dual-semiconductor system based on single-crystal electrodes composed of n- TiO_2 (anode) and p-SiC (cathode). We have also investigated photocatalytic processes on both crystalline and powder forms of semiconducting SiC with an ultimate goal of developing a dual-semiconductor system combining TiO_2 and SiC. Although both of these materials possess similar bandgaps, the band positions are different and an effective combination is expected to provide a larger range of redox potentials for oxidative and reductive photoprocesses when compared to the redox potentials provided by either of these individual materials. Removing the passive oxide overlayer was particularly important for exploiting photocatalytic processes on SiC. Photoreductions of methyl orange and chromium metal using aqueous suspensions of SiC powder showed a potential for developing a new generation of photocatalysts. A composite of TiO_2/SiC was prepared by thermochemical deposition of TiO_2 onto SiC powder. Photoelectrochemical properties of both single crystal SiC and metal-coated SiC were investigated using cyclic voltammetry, the metal thin layers being gold, platinum, silver and

titanium. This was done to investigate, in a controlled manner, the effect of oxide formation on SiC and possible methods of passivation.

We have performed kinetic photo-experiments on aqueous suspensions of SiC and TiO_2 powders using the reduction of methyl orange as a probe. An effective combination of these materials is expected to provide a larger range of redox potentials for oxidative and reductive photoprocesses when compared to the redox potentials provided by either of these individual materials. First, we have found that etching SiC with 50% HF solution for a period of two hours is necessary before any photoreduction occurs. Furthermore, investigation of SiC powders with transmission electron microscopy has confirmed that the HF-treatment removes an amorphous SiO_2 layer from the surface. We have found that the initial rate of photoreduction of methyl orange (to hydrazine) decreases with increasing pH (for the range 4.4 - 9.0), because of a relative unavailability of a specific form of methyl orange at pH higher than 6.5. However, when compared with TiO_2, the photoreduction of methyl orange by SiC is slower by an order of magnitude even at low pH. Nevertheless, we found that SiC can be used to remove Cr^{+6} from aqueous solution in the presence of Na_2EDTA, a hole scavenger. These experimental evidences indicate that the redox processes on SiC most likely occur via processes similar to those known for TiO_2.

Mathematical modeling was also performed to identify parameters that can improve the efficiency of SiC-based photocatalytic systems. A theoretical model has been developed to match semiconducting photocathode and photoanode materials for efficient reduction of metal ions and oxidation of toxic organics present in polluted water. In this model, the physical properties such as bandgaps, band position, doping density, etc. of both p- and n-type semiconductors and also

the properties of donor and acceptor species in solution were incorporated. Computer experiments were carried out to establish which p-type semiconductor (e.g., p-SiC, p-SiC(Pt)), in conjunction with the n- TiO_2 semiconductor, would be the most efficient partner. Examination of these factors provides a guideline to select the best p-type semiconductor to use in conjunction with the n- TiO_2 semiconductor for efficient detoxification of polluted water. Some of the results from theoretical model are found to be in direct contrast with our experimental results.

Much has been learned by Sandia through this LDRD project. We have tested some of our initial ideas and now have a better understanding of the phenomena of porphyrin- and TiO_2-based photoactivities. We submitted one patent application based on this project on enhanced photodetoxification of water using visible-light-absorbing metalloporphyrins on semiconducting TiO_2 and nonconducting Al_2O_3 suspensions. Although the conceptual TiO_2/SiC photodiode shows some promises for photoreduction processes, SiC itself was found to be an inefficient photocatalyst when combined with TiO_2. Alternative semiconductors with bandgap and band potentials similar to SiC should be tested in the future for further development and a practical utilization of the dual photodiode concept.

TABLE OF CONTENT

LIST OF FIGURES

LIST OF TABLES

Intentionally Left Blank

Chapter 1

General Introduction

1.0. Background

The catalytic and photocatalytic activities observed in nature can be utilized to develop processes that are industrially, economically, and environmentally important. For example, treatment of dilute aqueous toxic waste represents a problem of international importance. There is a present need to develop processes that can be used to detoxify various classes of chemical wastes.

During the last two decades, extensive research programs have been pursued in the area of heterogeneous photocatalysis with semiconducting particulate systems for the photooxidation of waste and polluted water, splitting of water, oxidation of hydrogen sulfide, and applications in paints and pigments. Most of the work found in the literature regarding heterogeneous photocatalytic processes deals with powder suspensions. Semiconductors used as photocatalysts include TiO_2,[1-16] ZnO,[17] CdS,[18,19] and Fe_2O_3.[20-22] The stability of semiconducting particulates in the chemical environments of interest is a primary requirement for their use as photocatalysts. This condition is only met by a few n-type semiconductors, particularly by TiO_2. Strontium titanate has similar structure and stability to TiO_2. However, large bandgaps of these oxide semiconductors requires UV irradiation for photocatalytic processes to occur. Low-bandgap semiconductors such as CdS and Fe_2O_3 have been employed but have suffered limited photoactivities and lack of reproducibility. In the case of CdS, irreversible corrosion occurs.[23-26]

Titanium dioxide photocatalysis has received widespread attention as a means for harnessing solar energy to treat polluted water.[1-4] Much of the emphasis is being placed on destroying volatile organic compounds that are found in contaminated groundwater.[5-7] Besides treating water contaminated with organic chemicals, it is also well known that TiO_2

photocatalysis can be effective for removing heavy metals from water.[4,8-10] In this process, a dissolved metal in a positive valence state is reduced, usually to the metallic form, and is caused to deposit on the photocatalyst. The photoreduction of metals requires oxidation that usually occurs through oxidative degradation of organics in order to maintain electroneutrality. Consequently, both oxidative destruction of organics and reductive removal of metals can be accomplished simultaneously.[4,8]

The energy available for use by TiO_2 ($\lambda \leq 400$ nm) only comprises about 4% of the solar spectrum (see **Figure 1.1**).[7,27] Much higher solar utilization efficiencies could be achieved through the development of photocatalysts capable of using visible light (45% of the sunlight) to drive photocatalytic waste detoxification chemistry. This might be accomplished by adsorption of appropriate dye molecules onto suitable surfaces.[28] Metalloporphyrins are a class of chemical compounds (dyes) which work as photocatalysts in nature. These tetrapyrroles have strong light absorption ability throughout the visible region.[29] It has been demonstrated by various laboratories that a number of metalloporphyrins are capable of driving a wide variety of photochemical reactions in aqueous solutions.[30,31] It has also been demonstrated that the photocatalytic activity of these dyes can be enhanced by immobilizing them on appropriate surfaces.[32]

A second major limitation of TiO_2 is that it does not provide the reduction potential necessary for many metals of environmental interest. However, other semiconductors with a considerable reducing capacity lack oxidizing power. The desired reduction potential could be achieved by developing a binary system combining n-TiO_2 (TiO_2 is naturally n-type) and a suitable p-type semiconductor whose band potentials are more negative than those for TiO_2. This

proposed binary photodiode will retain the photooxidative power of TiO_2 valence band while exhibiting a conduction band characteristic of the p-type material. We have used p-SiC, in conjunction with n-TiO_2, to investigate the possible effectiveness of the TiO_2/SiC photodiode. An effective combination of these materials is expected to provide a larger range of redox potential for oxidative and reductive photoprocesses when compared to the redox potentials provided by either of these individual catalysts. Both of these semiconductors have large bandgaps (>3.0 eV) but the band edges of SiC are positioned at more negative potential than those of TiO_2. Thus, the effective bandgap of the proposed photodiode is increased to ~4.5 eV which is expected to be photoactive under the illumination conditions of the individual semiconductors.

1.1. TiO_2-Structure and Energetics

There are three naturally occurring crystal phases of titanium dioxide: rutile, anatase, and brookhite. Most of the electrochemical and photocatalytic work to date have been performed on rutile or anatase, or a mixture of the two. Both rutile and anatase have tetragonal unit cells, and both structures contain slightly distorted TiO_6 octahedra. Rutile is thermodynamically more stable than anatase at room temperature; the free energy change for anatase to rutile is -5.4 kJ/mol.[33]

The absorption and reflection properties of rutile have been studied extensively. At 4 K, the short wavelength absorption edge for rutile is 410 nm (bandgap energy = 3.05 eV).[34,35] The lowest energy electronic absorption at 3.05 eV is an indirect transition. On the other hand, the bandgap of anatase is reported as 3.2 eV.[36] The absorption coefficients for both crystal phases are reported as ~10^5 cm^{-1} at 340 nm.[37]

Ultraviolet radiation below ~390 nm stimulates valence-band electrons in TiO_2 particles that are suspended in contaminated water. These electrons are promoted to the conduction band

(e^-_{cb}), creating holes in the valence band (h^+_{vb}). These electron/hole pairs can either recombine, producing thermal energy, or interact with the external environment to perform oxidation and reduction reactions. **Figure 1.2** shows that the position of the TiO_2 bands shift toward more reducing potentials as pH increases. However, the bandgap itself stays constant at about 3.2 eV (for the anatase form). This means that it always requires photons of below 390 nm, while the ability of the resultant electrons and holes to perform redox chemistry can be manipulated via pH, an external variable.

1.1.0. TiO_2 During Photocatalysis

The holes at the TiO_2 valence band can migrate to the catalyst surface and either can oxidize an adsorbed species directly or can react with water and adsorbed OH^- to produce hydroxyl radicals that are powerful oxidizers capable of attacking dissolved organics. For both cases of oxidative pathways, the final products are reported to be water, carbon dioxide and other simple and non-toxic inorganic products. The electrons, in turn, react with dissolved oxygen to form superoxide anions (O_2^-) that also form hydroxyl radicals after further reactions.[2,4,8] Alternatively, the electrons can react with dissolved metal cations of the proper reduction potentials. Along with the TiO_2 bandgap, **Figure 1.2** also shows the standard redox potentials of various metals, O_2, and OH^-. In theory, any species falling between TiO_2's conduction and valence bands can interact with the electrons and holes. The photoredox chemistry on the TiO_2-water interface is depicted schematically in **Figure 1.3**.

A major factor affecting the efficiency of photocatalytic reactions is electron/hole recombination. The recombination rate increases linearly with the production of the electron and hole concentrations. Therefore, if reduction reactions are able to rapidly deplete the

concentration of conduction-band electrons, then the electron/hole recombination rate falls off and overall oxidation efficiency increases. Similarly, if valence-band holes are rapidly filled by oxidation reactions, then reduction efficiency increases. The net effect is that the reduction of metals enhances the oxidation of organics. Enhancement of the reduction process is more complicated, however, because oxidation normally occurs via hydroxyl radicals.

1.2. Metalloporphyrins

These conjugated large organometallic compounds comprise a diverse class of complex molecules that possess a wide spectrum of photochemical and catalytic behaviors.[29-31,38-42] Metalloporphyrins are attractive candidates for many photochemical processes because of their strong absorption cross-sections throughout the visible region and their high chemical stability.[29,43] The potential to use metalloporphyrins as photocatalysts and photosensitizers for many chemical processes is enhanced because of the ability to control their functional properties by changing their central metal ion and tailoring the peripheral groups of the macrocycles.

Porphyrins are capable of complexing with virtually any metal in the periodic table. The properties of the metal affect the catalytic activity of the metalloporphyrin. Additionally, the metal may be axially ligated (five- or six-coordinate) which also affects metalloporphyrin catalytic activity. **Figure 1.4** shows the porphyrin skeleton which has four *meso* positions (C_m carbons) and eight pyrrole positions (C_β carbons) available for substitution. The variability of the metal, axial ligands, and peripheral substituents, allows the synthesis and characterization of numerous new porphyrin structures not encountered in nature. These variable parameters make the porphyrins attractive potential catalysts.[44]

The overall efficiency of the photocatalysts and photosensitizers is critically dependent upon both their equilibrium structures and their structural dynamics. Catalyst development is enhanced by using a multi-faceted approach that relies upon both the spectroscopic determination of structure-function relationships and computer aided molecular design (CAMD) of potentially useful metalloporphyrins. These methodologies are used in an iterative fashion. First, tetrapyrrole-containing natural enzymes are investigated to determine the structural characteristics that are important for catalytic activity. In the next step, synthetic metalloporphyrin analogs which exhibit the desired structure are designed and modeled. The most feasible metalloporphyrin prototypes are then synthesized and characterized. Finally, the potential metalloporphyrin catalysts are tested for activity and stability. Further improvements in design are realized as additional information becomes available about catalytic efficiency.

Structural distortions of metalloporphyrins are vital in controlling the interactions and binding between the macrocycle and its substrates in the vicinity. Most of the designed metalloporphyrin catalysts are highly substituted and therefore sterically crowded at the periphery. Three types of distortions that are observed in the metalloporphyrins are shown in **Figure 1.5**.

1.3. Specific Systems Investigated

1.3.0. Metalloporphyrins

The different metalloporphyrins that were investigated in this project are shown in **Figure 1.6**. They fall into two general classes: (a) octa-substituted porphyrins and (b) dodeca-substituted porphyrins. The basic porphyrin skeletons are porphine (P), octaethylporphyrin (OEP), tetraphenylporphyrin (TPP) and uroporphyrin I (UroP). Only the tin(IV)- and nickel(II)-derivatives, for example, Ni(II)UroP, $Sn(IV)Cl_2$UroP and $Sn(IV)Cl_2$ tetrakis(*p*-

carboxyphenyl)porphyrin (SnTCPP) were used for the photocatalytic detoxification studies. Both UroP and TCPP classes of porphyrins contain carboxylate groups attached to the porphyrin ring and, thus, can interact electrostatically with an oxide surface. The metal centers for the porphyrins were chosen based on their excited state life time. Metalloporphyrins with longer life time (for our case, SnUroP) interacts more efficiently with their immediate environment and reactants therein when compared to those metalloporphyrins with shorter life time (for our case, NiUroP). The dodeca-substituted porphyrins investigated under this LDRD project are the newly synthesized nickel-derivatives of octaacetic-acid-tetraphenylporphyrin (OAATPP), its octamethylester (OAATPP-OME), octahydroxyethyl-tetraphenylporphyrin (OHETPP), and octaacetic acid-tetra(*p*-nitrophenyl)porphyrin-octamethylester (OAATNPP-OME). The tin-analogs of this series were also tried to synthesize but with limited success. The photophysical properties of the nickel-analogs were characterized using spectroscopic methods.

1.3.1. Metalloporphyrins Immobilized on Surfaces

Porphyrins with carboxylic acid peripheral substituents are known to adsorb readily onto TiO_2 surfaces.[32,45] The photocatalytic activity of these molecular dyes can be enhanced by immobilizing them on appropriate surfaces. We have used TiO_2 as well as Al_2O_3, MgO, MnO_2, ZrO, etc. for immobilizing metalloporphyrins and tested their abilities as photocatalysts for degrading model toxins. A general protocol for this photodegradation process is shown in **Figure 1.7**. The alumina surface is photochemically different than the traditional photocatalyst TiO_2 since alumina has no useful semiconducting properties in relation to the solar spectrum, whereas TiO_2 has a bandgap that is able to utilize UV photons to initiate photochemistry. In this report,

results obtained using TiO_2 and Al_2O_3 surfaces are presented because other surfaces were either not active as support material or were not suitable for their expected catalytic activities.

1.3.2. Newly Synthesized Nickel Porphyrins

From experiments of solar photocatalytic destruction of model organic compounds it was found that SnUroP, with eight alternating acetate and propionate groups attached to β-pyrrole positions, works as an efficient photocatalyst. Since the pK_a values are different for the proton dissociations from acetic acid and propionic acid groups for any electrostatic interaction with the supporting surface, it was decided to synthesize uroporphyrin analogs with all eight carboxylate groups being same. Accordingly, Ni(II) complexes of octaacetic acid-tetraphenylporphyrin (OAATPP) and their derivatives were synthesized.[42] The four phenyl or nitrophenyl groups were attached to the bridging methine carbons of the NiOAATPP-series to determine the electronic effects asserted by the peripheral substituents on the porphyrin macrocyclic structure. Various spectroscopic methods, namely, proton NMR, ^{13}C NMR, mass spectroscopy, EXAFS, UV-visible absorption, and Raman spectroscopy, have been used to characterize these newly synthesized porphyrins.

The free acid forms of the above mentioned tetraphenylporphyrins possessing eight acetic acid groups are highly soluble in water. These porphyrins are found to be highly nonplanar as a result of the steric crowding of the twelve peripheral substituents. Prior to their synthesis, molecular mechanics calculations of OAATPP series indicated nonplanar saddle conformations. The effects of nonplanarity on the physical properties of Ni(II) derivatives of octaacetic acid-tetraphenylporphyrin (OAATPP), its octamethylester (OAATPP-OME), octahydroxyethyl-tetraphenylporphyrin (OHETPP), and octaacetic acid-tetra(*p*-nitrophenyl)porphyrin-

octamethylester (OAATNPP-OME) were investigated. The structures of these new porphyrins are shown in **Figure 1.6(b)**. Since acetic acid and ester moieties are more electron-withdrawing than alkyl, hydroxyethyl and acetate substituents, and the nitrophenyl meso substituent is more electron withdrawing than the unsubstituted phenyl group, distinct chemical properties are also expected for these nickel porphyrins because of the differing electronic properties. Thus, both electronic effects and nonplanarity effects must be considered when correlating spectral differences and chemical properties.

1.3.3. Silicon Carbide

As discussed earlier, the large bandgap n-TiO_2 can be used as a stable solar energy material for photodetoxification of toxic materials present in polluted water.[1-16] However, the efficiency of a system having a single semiconducting material is not high enough for a practical application. Additionally, TiO_2 alone does not have the potential to reduce a large set of metals of environmental interest.[4,8] Hence, development of a *binary* system which involves both n- and p-type semiconducting materials is desirable.

Stable p-type semiconducting materials may be useful for coupling with n-TiO_2 to develop a photodiode system for simultaneous photooxidation of organics and photoreduction of toxic materials present in polluted water. A high band gap p-SiC (Eg ~3 eV) semiconductor has been identified[46,47] which could be coupled with the high band gap n-TiO_2 (Eg = 3 eV) to develop an efficient binary photocatalytic system. The binary system is expected to provide a larger bandgap (with two, rather than one UV photon) as well as a wider range of redox potential when compared to those of the individual semiconducting. The proposed binary photoelectrochemical system is depicted in **Figure 1.8.** A successful development of a novel SiC/TiO_2 photocatalytic

diode would extend the effective bandgap from 3.0 eV (for each of the components) to ~4.5 eV by using two ultraviolet photons (for more detail, see the Introduction section in Chapter 4).

1.4. Report Outline

Photocatalytic activities of metalloporphyrins immobilized on different surfaces are presented in chapter 2. The active tin porphyrins are found to be photolabile on semiconducting titania but photostable on non-conducting alumina. Adsorption of porphyrins onto the support materials at pHs below the points of zero charge (pzc) of the respective surfaces (pzc's for TiO_2 and Al_2O_3 surfaces are 6.0 and 7.8, respectively) and the presence of oxygen during the photo-experiments are crucial for photocatalytic degradation with these developed catalysts.

Characterization of a newly synthesized class of water-soluble dodeca-substituted porphyrins is presented in chapter 3. Nickel-derivatives show interesting nonplanar structures, aggregation behaviors and ligand binding properties. The information gathered from these new porphyrins is expected to lead to the design and synthesis of suitable porphyrins for their applications in water detoxification.

Chapter 4 describes our efforts in engineering a binary photocatalyst based on single crystal electrodes composed of n-TiO_2 (anode) and p-SiC (cathode). Kinetic results of the photoreduction of methyl orange using TiO_2 and SiC powders are also presented where the unpassivated SiC shows a photoreduction efficiency of one order of magnitude lower than TiO_2. Finally, a theoretical model was developed to identify parameters that can improve the efficiency of SiC-based photocatalytic systems.

1.5. Figures

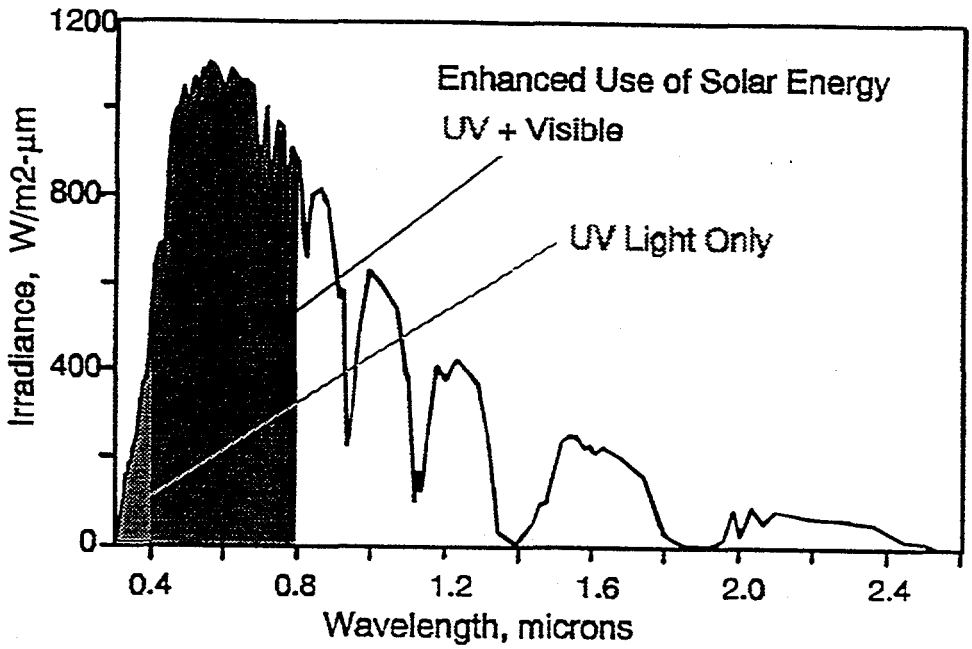

Figure 1.1. Direct normal solar spectrum (air mass 1.5). Only the ultraviolet (light shaded region, $\lambda < 400$ nm) is used by the bare TiO_2 for the charge separation through bandgap excitation. Shaded region (dark, $\lambda > 400$ nm) shows portion of solar spectrum used by different metalloporphyrins.

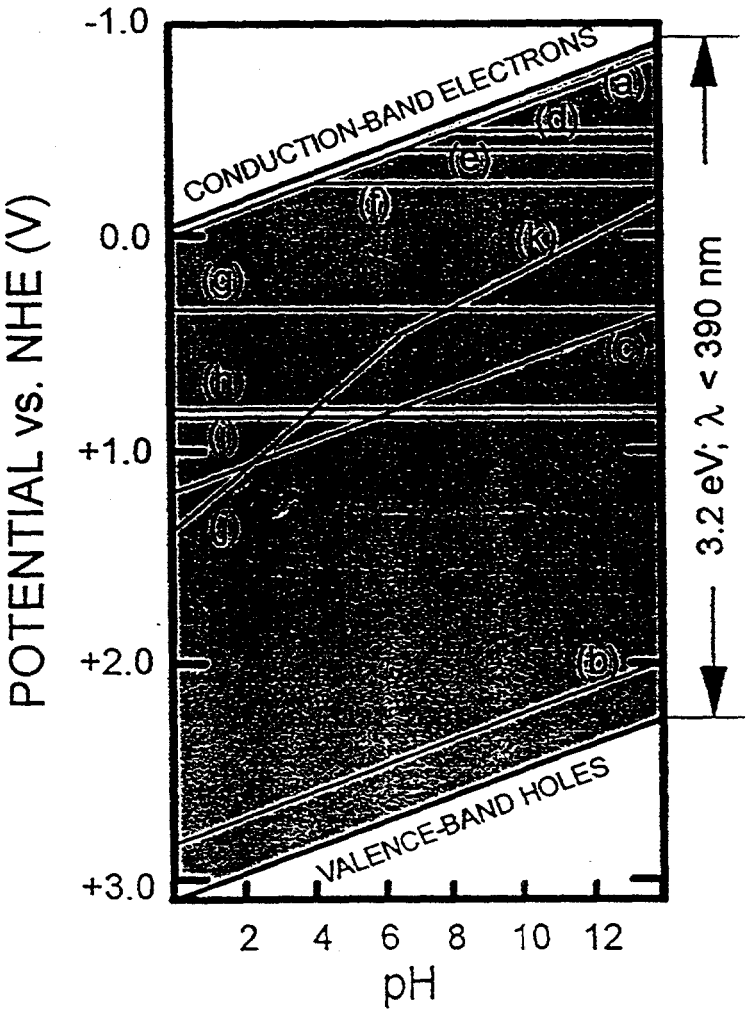

Figure 1.2. The bandgap of TiO_2 (anatase) relative to the redox potential of a variety of important reactions. (a) H_2/H^+; (b) $OH^-/OH^\bullet$; (c) H_2O/O_2; (d) $O_2^{-\bullet}/O_2$; (e) Cd/Cd^{2+}; (f) Ni/Ni^{2+}; (g) Cu/Cu^{2+}; (h) Ag/Ag^+; (i) Hg/Hg^{2+}; (j) Pt/Pt^{2+}; (k) Cr^{4+}/Cr^{3+}.

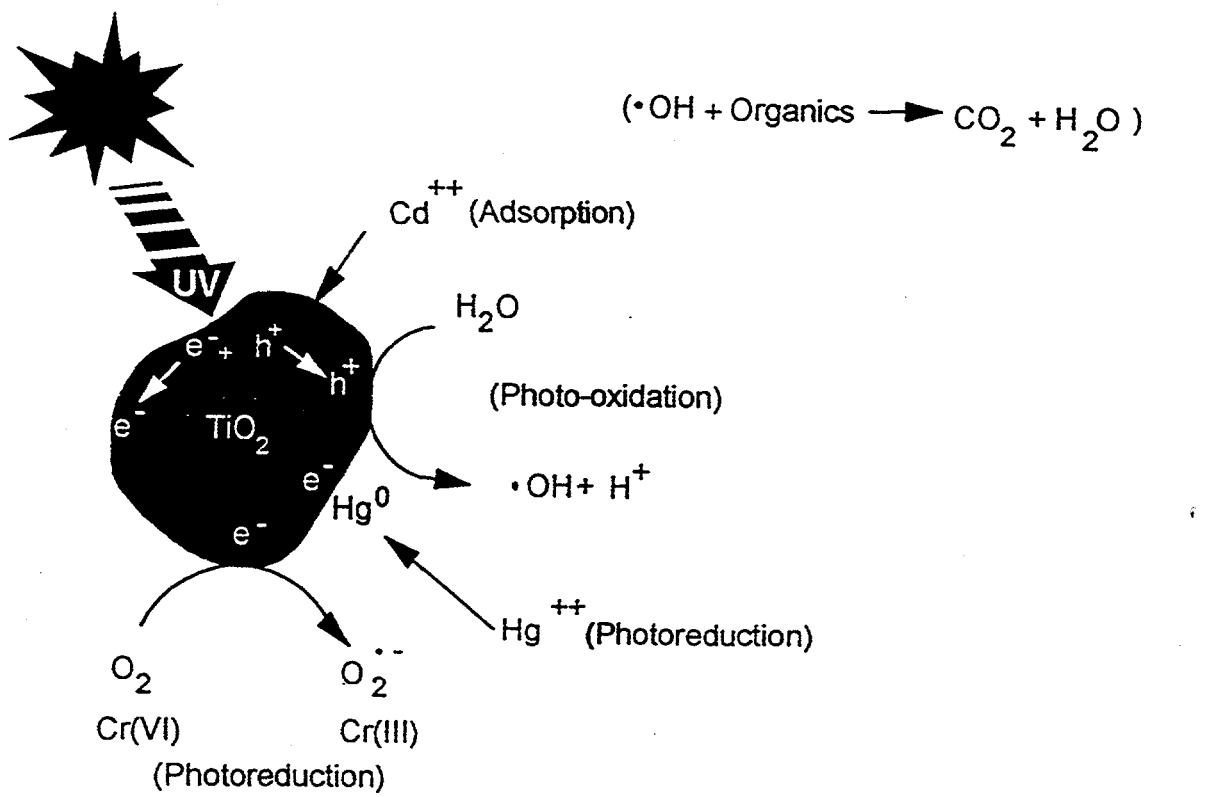

Figure 1.3. Photo-induced redox processes on the surface of a semiconducting TiO_2 particle when suspended in an aqueous medium. Chemical processes of adsorption, photooxidation, photoreduction, and radical formation from water and H_2O_2 on the water-titania interface are shown schematically. The final step of the photo-initiated oxidative degradation of organic compounds to simpler molecules CO_2 and H_2O is also shown.

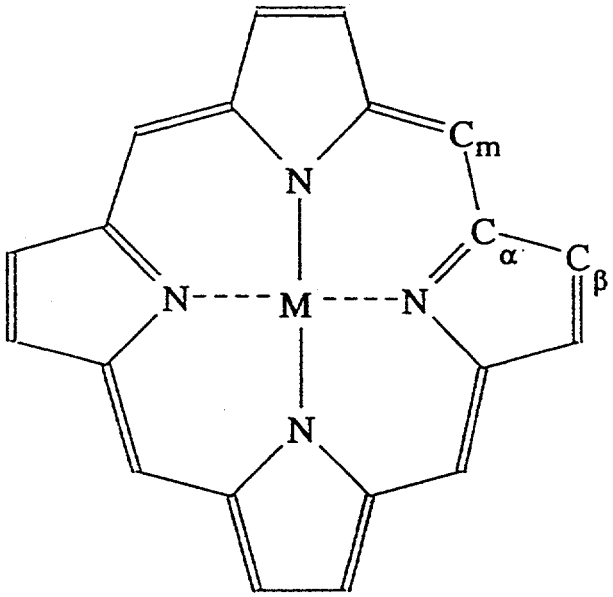

Figure 1.4. The basic metalloporphyrin skeleton with the atom types shown. There are twenty carbons (8 C_β, 8 C_α and 4 C_m) and four nitrogens.

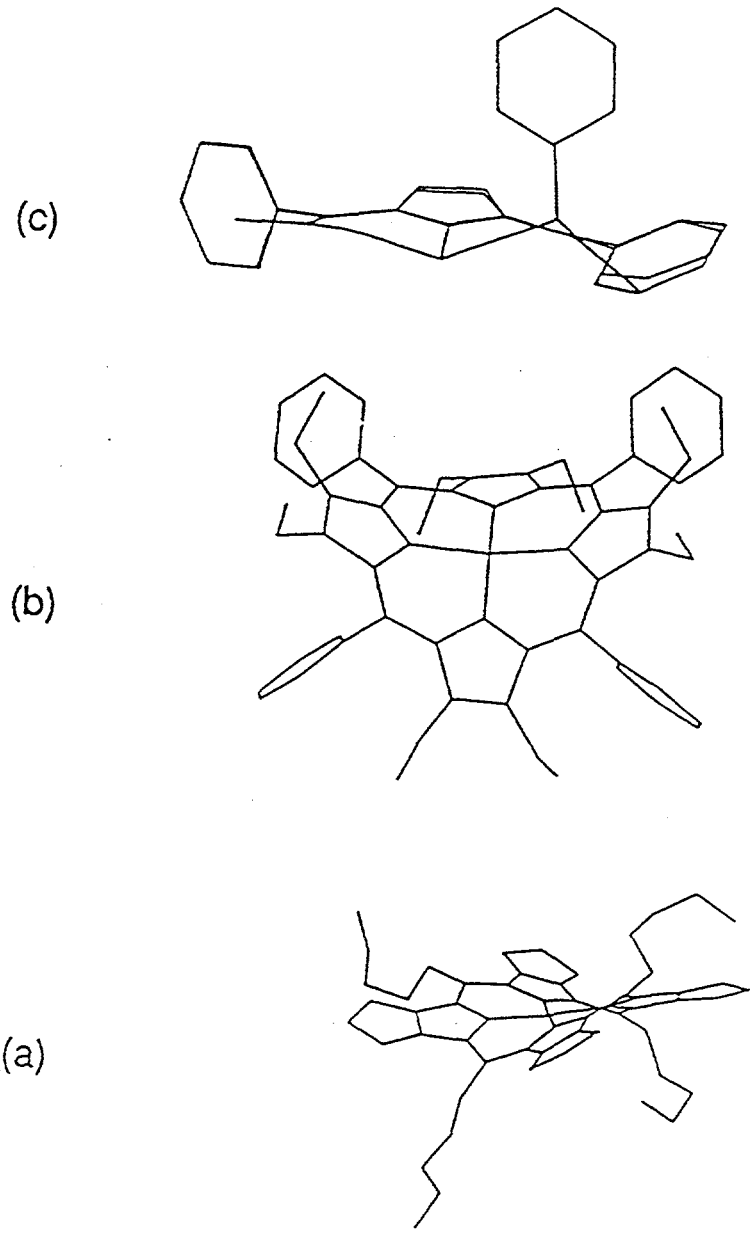

Figure 1.5. Three types of nonplanar distortions exhibited by metalloporphyrins: (a) ruffling, (b) saddle-shaped and (c) an asymmetric distortion in which a single pyrrole ring is tilted with respect to the mean porphyrin plane.

(a)

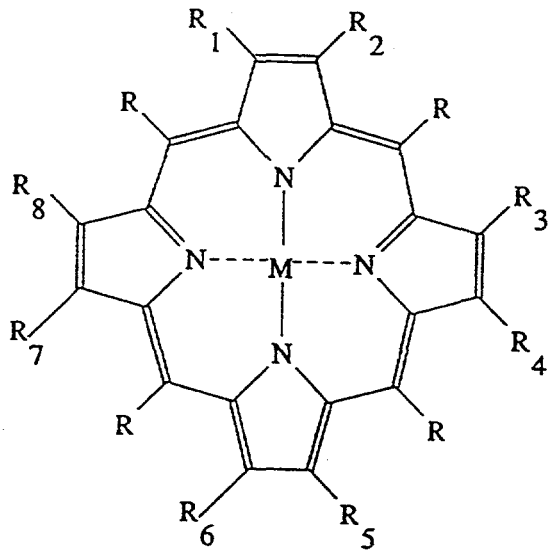

R_1-R_8 = H	R = H	(P)
R_1-R_8 = CH_2CH_3	R = H	(OEP)
R_1-R_8 = H	R = C_6H_5	(TPP)
R_1-R_8 = H	R = C_6H_5COOH	(TCPP)
$R_1 = R_3 = R_5 = R_8$ = CH_3 $R_2 = R_4$ = $CH{=}CH_2$ $R_6 = R_7$ = C_2H_4COOH	R = H	(PP)
$R_1 = R_3 = R_5 = R_8$ = CH_3 $R_2 = R_4$ = CH_2CH_3 $R_6 = R_7$ = C_2H_4COOH	R = H	(MP)
$R_1 = R_3 = R_5 = R_8$ = CH_3 $R_2 = R_4$ = $CH{=}CH_2$ $R_6 = R_7$ = $C_2H_4COOCH_3$	R = H	(PP-DME)
$R_1 = R_3 = R_5 = R_7$ = CH_2COOH $R_2 = R_4 = R_6 = R_8$ = C_2H_4COOH	R = H	(UroP)

Figure 1.6 (a). Metalloporphyrin structures: porphine (P), octaethylporphyrin (OEP), tetraphenylporphyrins (TPP), tetra(*p*-carboxyphenyl) porphyrin (TCPP), protoporphyrin IX (PP), PP-dimethylester (PP-DME), mesoporphyrin IX (MP), and uroporphyrin I (UroP).

(b)

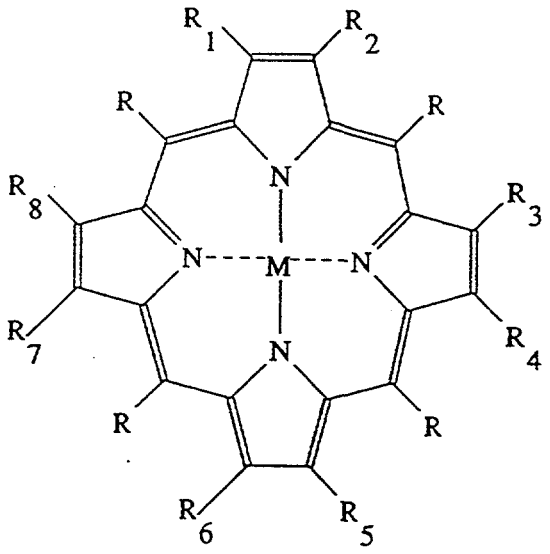

$R_1 = R_8 = CH_2CH_3$	$R = C_6H_5$	(OETPP)
$R_1 = R_8 = CH_2COOH$	$R = C_6H_5$	(OAATPP)
$R_1 = R_8 = CH_2COOCH_3$	$R = C_6H_5$	(OAATPP-OME)
$R_1 = R_8 = CH_2CH_2OH$	$R = C_6H_5$	(OHETPP)
$R_1 = R_8 = CH_2COOCH_3$	$R = C_6H_4NO_2$	(OAATPP-OME)

Figure 1.6 (b). Metalloporphyrin structures: dodeca-substituted porphyrins: octaethyl-tetraphenylporphyrin (OETPP), octaacetic-acid-tetraphenylporphyrin (OAATPP), octamethylester of OAATPP (OAATPP-OME), octahydroxyethyl-tetraphenylporphyrin (OHETPP), and tetra(*p*-nitrophenyl) of OAATPP-OME (OAATNP-OME).

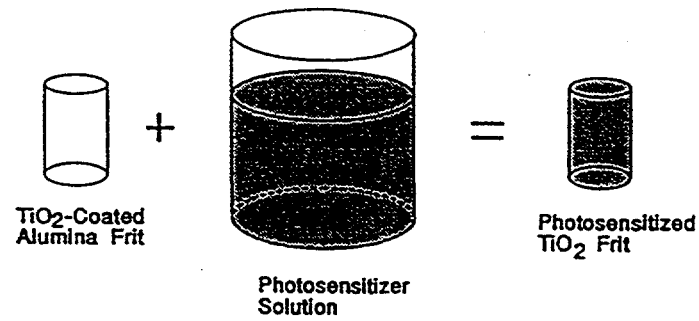

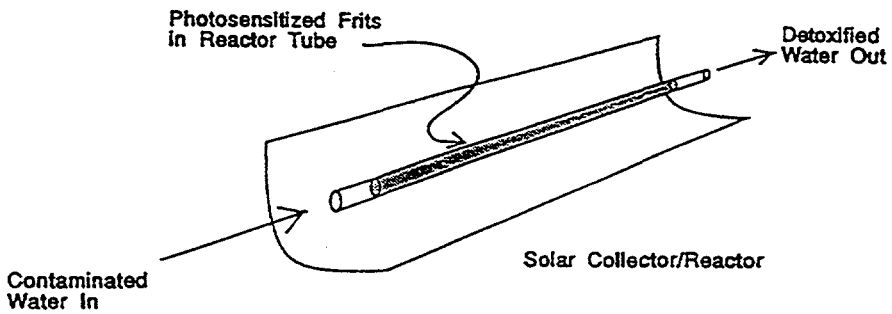

Figure 1.7. Schematic of a solar trough to collect a broader solar spectrum when dye molecules, immobilized on a support material, are used for photodegradation process.

TiO_2/SiC Photodiode

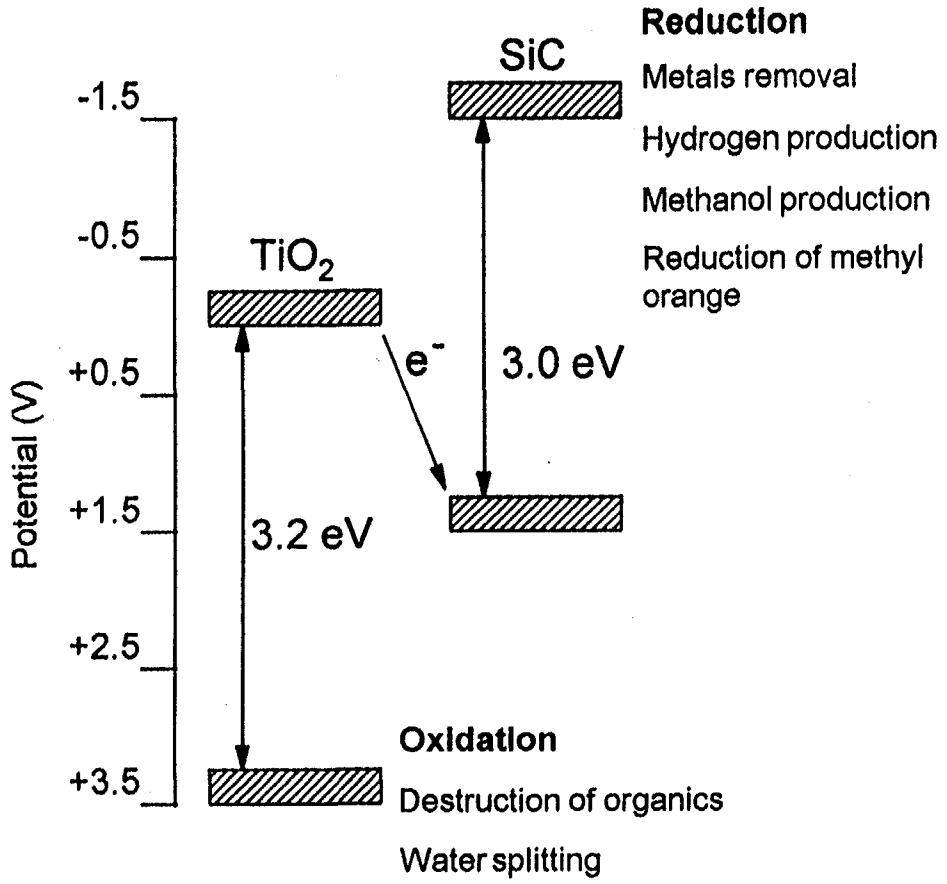

CONCEPTS

- Retains the oxidation potential of TiO_2 but increases the reduction power.
- Effective bandgap of ~4.5 eV.
- Needs photons with 3.0 eV or more.

Figure 1.8. Schematic diagram of coupled p-SiC and n-TiO_2 semiconductor

1.6. References

1. Ollis, D.F. *Environ. Sci. Technol.* **1985**, *19*, 480.

2. Mathews, R. W. *J. Catal.* **1988**, *111*, 264.

3. Turchi, C.S.; Ollis, D.F. *J. Catal.* **1990**, *122*, 178.

4. Prairie, M.R.; Evans, L.R.; Stange, B.M.; and Martinez, S.L. *Environ. Sci. & Technol.* **1993**, *27*, 1776.

5. Ahmed, S.; Ollis, D.F. *Solar Energy* **1984**, *32*, 597.

6. (a) Al-Ekabi, H.; Serpone, N. *J. Phys. Chem.* **1988**, *92*, 5726. (b) Serpone, N. *J. Photochem. Photobiol.* **1996**, *93*, 199.

7. Pacheco, J.; Yellowhorse, L. *Sandia National Laboratories Report SAND92-0385*, Albuquerque, NM, **1992**.

8. Madden, T.H.; Considerations in the Treatment of Metal-EDTA Complexes using TiO_2 Photocatalysis, *Masters Thesis*, University of New Mexico, **1996**.

9. Tanaka, K.; Harada, K.; and Murata, S. *Solar Energy* **1986**, *36*, 159.

10. Serpone, N.; Ah-You, Y.K.; Tran, T.P.; Harris, R.; Pelizzetti, E.; and Hidaka, H. *Solar Energy* **1987**, *39*, 491.

11. Schmelling, D.C.; Gray, K.A.; and Kamat, P.V. *Environ. Sci. & Technol.* **1996**, *30*, 2547.

12 Frank, S.N.; Bard, A.J. *J.Phys.Chem.* **1977**, *38*, 1484.

13 Pelizzetti E.; Surpone, N.; In *Electrocatalysis and Environment*, Schiavello, M. Ed.; Kluwer Acad. Pub. Boston; pp. 469-497, **1988**.

14 Xu, Y.; Chen, X. *Chem. & Industry* **1990**, *15*, 497.

15 Chen, L-C.; Chou, T-C. *J. Mol. Cat.* **1993**, *85*, 201.

16 Chen, L-C.; Chou, T-C. *Ind. Eng. Chem. Res.* **1993**, *32*, 1520.

17. Anpo, M.; Chiba, K.; Tomonari, M.; Coluccia, S.; Che, M.; and Fox, M.A. *Bull. Chem. Soc. Jpn.* **1991**, *64*, 543.

18. Davis, A.P.; Huang, C.P. *Water Res.* **1991**, *25*, 1273.

19 Mills, A.; Williums, G *J. Chm. Soc., Faraday Trans. I* **1987**, *83*, 2647.

20. Itoh, K.; Bockris, J.O'M. *J. Electrochem. Soc.* **1984**, *131*, 1266.

21. Maruthamuthu, P.; Ashokkumar, M.; and Venkatasubramanium, L.; *Bull. Chem. Soc. Jpn.* **1991**, *64*, 1933.

22. (a) Majumder, S.A.; Khan, S.U.M. *Int. J. Hydrogen Energy* **1994**, *19*, 881. (b) Majumder, S.A.; Photosplitting of water at surface modified single crystal p-Si and at thin film n-Fe_2O_3 and n-CdS photoelectrodes, *Masters Thesis*, Duquesne University, **1988**.

23. Frank, A.J.; Honda, K *J. Phys. Chem.* **1982**, *86*, 1933.

24. Gutierrez. M; Henglein, A. *Ber. Bunsen.-Ges. Phys. Chem.* **1983**, *87*, 474.

25. Kaneko, M.; Okada, T.; Teratani, S.; and Taya, K *Electrochem. Acta* **1987**, *32*, 1405.

26. Gerischer, H. *J. Electroanal. Chem.* **1975**, *58*, 263.

27. Boer, K. W. *Solar Energy*. **1977**, *19*, 525.

28. Majumder, S.A.; Environmental effects on structure-function relationships in metalloporphyrin-based catalytic systems, Ph.D. Dissertation, University of New Mexico, **1994**.

29. Smith, K.M.; In *Porphyrins and Metalloporphyrins*, K.M. Smith (Ed.), Elsevier Scientific Publishing, Amsterdam, pp 3-28, **1975**.

30. Shelnutt, J. A. *United States Patent 4,568,435*, **1986**.

31. Majumder, S.A.; Prairie, M.R.; Ondrias, M.R.; and Shelnutt, J.A.; In *Solar Engineering*, Stin, W.; Kreider, J.; Watanabe, K.(Eds.); pp. 9-14, *American Society of Mechanical Engineers*, **1992**.

32. (a) Moser, J.; Gratzel, M. *J. Am. Chem. Soc.* **1984**, *106*, 6557. (b) Kalyanasundaram, K.; Shelnutt, J. A.; and Gratzel, M. *Inorg. Chem.* **1988**, *27*, 2820. (c) Kalyanasundaram, K.; Vlachopoulos, N.; Krishnan, V.; Monnier, A.; and Gratzel, M. *J. Phys. Chem.* **1987**, *91*, 2342.

33. *The Oxide Handbook*, Samsonov, G.V. Ed.; IFI/Plenum, New York, p23, **1982**.

34. Grant, F.A. *Rev. Modern Phys.* **1959**, *31*, 646.

35. Cronemeyer, D.C. *Phys. Rev.* **1952**, *87*, 876.

36. Bickley, R.I. *Chem. Phys. of Solids and Their Surfaces* **1978**, *7*, 118.

37. Salvador, P. *Solar Energy Mater* **1982**, *6*, 241.

38. *The Porphyrins*; Dolphin, D., Ed.; Academic Press; New York; **1978-1983**; Vol. 1-8.

39. *Iron Porphyrins*; Lever, A.B.P., Gray, H.B., Eds.; Addison-Wesley: Reading, PA, **1983**; Vols. 1 and 2.

40. (a) Sparks, L.D.; Medforth, C.J.; Park, M.-S.; Chamberlain, J.R.; Ondrias, M.R.; Senge, M.O.; Smith, K.M.; and Shelnutt, J.A. *J. Am. Chem. Soc.* **1993**, *115*, 581. (b) Medforth, C.J.; Senge, M.O; Smith, K.M.; Sparks, L.D.; and Shelnutt,. J.A. *J. Am. Chem. Soc.* **1992**, *114*, 9859. (c) Shelnutt, J.A.; Medforth, C.J.; Berber, M.D.; Barkigia, K.M.; and Smith, K.M. *J. Am. Chem. Soc.* **1991**, *113*, 4077.

41. Gouterman, M.; Rentzepis, P.M.; and Straub, K.D.; In *Porphyrins*, ACS Symposium Series 321, **1986**.

42. Miura, M.; Majumder, S.A.; Hobbs, J.D.; Renner, M.W.; Furenlid, L.R.; and Shelnutt, J.A. *Inorganic Chemistry* **1993**, *33*, 6078.

43. Gouterman, M. in *The Porphyrins*, Dolphin, D., Ed., Academic Press, New York; **1978**; Vol. 3, Chapter 1.

44. (a) *Biomimetic Chemistry*; Dolphin, D., Ed.; ACS Press, Washington, D.C.; **1980**. (b) *Photochemistry of Polypyridine and Porphyrin Complexes*; Kalyanasundaram, Academic Press; **1992**.

45. (a) Nasr, C; Vinodgopal, K; Fisher, L; Hotchandani, S.; Chattopadhyay, A.K.; and Kamat, P.V. *J. Phys. Chem.* **1996**, *100*, 8436. (b) Vinodgopal, K; Wynkoop, E.; and Kamat, P.V. *Environ. Sc. & Tech.* **1996**, *30*, 1660.

46. *Gmelin Handbook of Inorganic Chemistry*, 8th edition, supplement volume B 3; Katscher, H.; Sangster, R.; and Schroder, F. Eds.; Spring-Verlag, **1986**.

47. Lauermann, I. *The Photoelectrochemistry of Silicon Carbide*, Ph.D. Dissertation, Solar Energy Institute, Hannover, Germany, **1994**.

Chapter 2

Visible Light-Initiated Photocatalytic Detoxification of Salicylic Acid and Aniline by Adsorption of Porphyrins onto Titania (TiO_2) and Alumina (Al_2O_3) Substrates

2.0. Introduction

The photocatalytic activity of porphyrin dyes can be enhanced by immobilizing them on appropriate surfaces.[1-7] Photosensitization of TiO_2 by porphyrins and other dyes has been observed using flash photolysis techniques[1,2,8] and photoelectrochemical techniques.[9-11] The dye absorbs visible light, not utilized by bare TiO_2, initiating photochemical redox reactions by electron transfer between the TiO_2 surface and the dye molecules, thereby improving the utilization of the available solar energy to drive the detoxification process.

An energy diagram of this sunlight-driven process through dye-coated TiO_2 is shown in **Figure 2.1.** Relevant redox potentials of tin porphyrin (SnP) are indicated based on those of $Sn(OH)_2$octaethylporphyrin reported by Felton et.al.[12] The absorption of visible light by a SnP molecule can lead to a redox cycle that generates reactive porphyrin species (e.g., the anion and/or cation) that can directly attack a target organic compound. Alternatively, the removal of TiO_2 conduction band electrons by reduction of porphyrin triplet excited state (SnP^*/SnP^-) at 1.1 V vs. NHE would prevent rapid electron-hole recombination. Thus, TiO_2 valence band holes can react more efficiently with the target organic compound. Either one or combination of the above described energy transfer pathways between excited TiO_2 and SnP molecules would lead to an enhancement of photodetoxification of contaminants in water.

Metalloporphyrins with carboxylic acid peripheral substituents are known to adsorb readily onto the TiO_2 surface.[4,5,8] Consequently, the abilities of NiUroP, SnUroP and SnTCPP were investigated to enhance destruction of organic compounds. Salicylic acid (SA) was used as a model organic compound and aniline (AN) was used as a real toxin to investigate the photocatalytic effects on different substrates. The structures of these metalloporphyrins are

shown in **Figure 2.2.** NiUroP was used to investigate the adsorption of porphyrin, because it has no redox active excited state. In contrast, both of the SnPs have a long-lived triplet excited state that can itself initiate redox chemistry.

The main objective of this work is to utilize the electron transfer between the dyes and TiO_2 through the adsorption of suitable porphyrins to the TiO_2 semiconductor surface and, thereby, to enhance solar photocatalytic detoxification on the surface. A second objective is to develop an understanding of the mechanism of porphyrin-enhanced solar detoxification. A third goal of this work is to stabilize the photodegradable photocatalysts on the surface to obtain the optimal photocatalytic effect over a long period of time. Finally, immobilizing metalloporphyrins on non-conducting substrates like alumina, may allow for the determination of their inherent photocatalytic properties under conditions where they do not degrade.

2.1. Materials and Methods

Al_2O_3 and TiO_2 powders were obtained from Degussa and Tioxide. The uroporphyrins were obtained from Porphyrin Products (Logan, UT) and SnTCPP was obtained from Mid Century Chemical (Posen, IL). All porphyrins were used without further purification. Reagent grade chemicals from Fisher Scientific and Aldrich Chemical were used as purchased. The water used for preparing samples was carbon filtered and deionized to a conductivity of ≤ 3.0 μmho-cm.

Dye-coated Al_2O_3 and TiO_2 samples were prepared by adding solid substrate and salicylic acid (SA) to a tin-porphyrin (SnP) solution (300 ml) for a final composition of 15 mM SnP, 0.1w% TiO_2 or 0.2w% Al_2O_3, and 217 mM SA (pH 5.0 and 6.0). The mixture gives a cloudy white dispersion in the absence of porphyrin, but in the presence of porphyrin gives either a cloudy pink (high pH) or a cloudy green (low pH) mixture for the case of TiO_2. The change of

color from pink (which is the color of the unadsorbed SnP in solution) to green is due to the adsorption of SnP onto TiO_2 and its subsequent reduction on the surface. No such color changes are seen with Al_2O_3 substrates. The bulk of the TiO_2 or Al_2O_3 preparations settles out without stirring. Components were added in different orders and in varying compositions to determine the effect of competitive adsorption onto the TiO_2 surface.[13,14] The amount of porphyrin adsorbed onto the TiO_2 surface was measured by following the decrease in the Soret band of the porphyrin while the pH of the solution was adjusted to various values in the range 3-11 with constant stirring. Similar adsorption experiments were performed with Al_2O_3. Substrate samples, both in presence and absence of SnPs, were adjusted to the operating pH (4.5, 5.0, or 6.0) depending on the porphyrin used for that sample.

A large mouth 1500 ml jacketed pot reactor (Cal-Glass, Costa Mesa, CA) and a 100 W UV mercury vapor lamp (Spectroline Model MB-100 with a Sylvania Par 38 mercury bulb; 7000 mW/cm^2 UV at 365 nm at a distance of 40 cm) were used for laboratory-scale photocatalytic detoxification experiments (see **Figure 2.3**).[15] The outer jacket allowed constant temperature (~25°C) experiments. A quartz lid and a UV filter were sealed in place with an O-ring between the UV lamp and the sample mixture to select only the visible portion of the lamp's spectrum ($\lambda >$ 390 nm). The 390-nm UV cut off filter with $A_{360} = 3.0$, $A_{390} = 1.1$, and $A_{400} = 0.2$ O.D. was considered as the best possible combination to allow sufficient absorption of light by SnP, but also to block UV-excitation in the TiO_2 photocatalyst.

The apparatus allowed experiments to be done under ambient-oxygen and constant nitrogen-purging conditions. Oxygen free experiments were carried out by purging nitrogen (900 cm^3/min, 20 °C, 1 atm) through a stainless steel frit into the reaction solution for 15 min prior to

and continued throughout the experiment. The contents of the reactor were magnetically stirred throughout each experiment. Samples (2 ml) were collected at various time intervals up to 500 minutes for immediate analysis using a HP8452A UV-visible spectrophotometer. All batch experiments were performed using 300 ml solution or suspension. The samples were filtered through 0.2 m Teflon syringe filters to remove the catalyst before spectral analysis. For some samples, total organic carbon (TOC) analysis was performed using a Shimadzu TOC 5000.

2.2. Results and Discussion

As mentioned in the introduction, photocatalysis is a complicated interfacial process on the surface of the semiconducting TiO_2 particles. The photoactivity of metalloporphyrin adds additional complexity to this process. The present discussion of the photochemical and photophysical processes with the photodetoxification of organic compounds involves the following: photoactive TiO_2 and metalloporphyrin and aqueous medium, photoinactive nonconducting Al_2O_3, point of zero charges of the supporting surfaces for metalloporphyrins, competitive adsorption of metalloporphyrins and target molecules onto the surfaces of alumina and titania, metalloporphyrin-mediated dispersion of TiO_2, pH-dependent activities of the photocatalysts, presence of oxygen and wavelength of the incoming photons.

2.2.0. Photocatalytic Activity of Tin(IV) Porphyrins

The spectra of solutions of SnUroP alone and of SA alone are shown in **Figure 2.4**. SnUroP shows a strong absorption band at 402 nm, but only weak UV absorbance. SA has a strong UV absorption band at 296 nm and other far UV bands, but does not absorb in the visible region. A broad and flat absorption band in the 200-340 nm range was (**Figure 2.4(b)**) observed when the suspension of SnUroP adsorbed onto TiO_2 particles is irradiated. This continuous UV

absorption band is from TiO_2 fine particles solubilized in suspension (see below) since in the absence of porphyrin no such absorption band was observed from the filtered solution of irradiated TiO_2 suspension. A part of this band may also be due to scattering of larger particles in the filtered solution using 0.2 μ-filter subsequent to the centrifugation. Additionally, the solution was transparent and no precipitation was observed upon further centrifugation of the solution under investigation.

The unsupported Sn porphyrins in solution show photoactivity for the conversion, but not destruction of salicylic acid, using visible light only. As shown in **Figure 2.5**, photocatalytic conversion of SA is indicated by the increase in absorbance near 260 nm between the SA absorption peaks at 230 and 296 nm, the increase in absorbance in the wing (near 325 nm) on the red side of the 296-nm absorption band, and other changes in the SA absorption spectrum after irradiation by visible light for 90 minutes. It is important to note here that no new absorption bands are observed near 260 nm when a SnUroP solution is illuminated under similar conditions but a chlorin band at 420 nm appeared due to the photo-induced ring reduction of porphyrin.[16] The conversion products of SA are thought to be slightly modified aromatic ring compounds that are yet to be identified. During 90 minutes of irradiation with visible light, considerable ring reduction of SnUroP was observed in presence of SA, as indicated by a gradual decrease in the 402-nm band and appearance of the chlorin at 420 nm (**Figure 2.5**). The rate of ring reduction of SnUroP was observed to be faster in the presence of SA which indicates a light-affected interaction between SnUroP and SA since these spectral changes were not observed in the room light over a long period of time. The initial pink color of SnUroP solution changes to green; from the absorption spectrum of the green pigment, the reduction product is mostly the Sn urochlorin[16] in which the β-carbons of one pyrrole ring of the porphyrin are reduced. Sn urophlorins[16] may

also be formed during irradiation. In contrast to the observed photo-induced ring reduction of SnUroP, SnTCPP does not photodecompose in the absence of the support although similar conversion of SA was observed under visible light illumination (data not shown).

Experiments with solutions of SnUroP and AN also exhibit photoactivity as shown in **Figure 2.5**. However, spectral changes for the SnUroP/AN system are more dramatic than for the SnUroP/SA system in the absence of any support. The 280-nm absorption band of AN is buried under the increased broad absorption in the 250-380 nm region during a visible light irradiation. Consequently, the 230-nm band was used for the subsequent analysis of the data obtained in presence of aniline (AN).

2.2.1. Photosensitization of TiO_2

Combination of either of the two porphyrins, SnUroP or SnTCPP, with TiO_2 yields a colored TiO_2 powder due to the absorption of visible light by the Sn porphyrin adsorbed onto the suspended TiO_2 particles. **Figure 2.4(a)** shows strong absorption bands of SnUroP in solution at 402, 536 and 574 nm. The disappearance of these absorption bands upon filtration of the suspension of TiO_2/SnUroP system indicates a complete adsorption of SnUroP onto the TiO_2 surface (see **Figures 2.4** and **2.6**). This phenomenon of adsorption is pH-dependent since binding to TiO_2 occurs at lower pH for SnTCPP (pH 4.5) than for SnUroP (pH 6.0). The pH-dependent adsorption of SnUroP molecules and dispersion of TiO_2 particles are shown in **Figure 2.6**.

As a first step in developing a more stable photosensitizer, the stability of the two Sn porphyrins (SnPs) on the TiO_2 surface and in solution were compared. The degree of degradation for the porphyrin/TiO_2 system was determined by removal of the porphyrin from the surface by raising the pH, and subsequently obtaining the absorption spectrum. In ambient room light,

adsorbed SnUroP is substantially degraded to the chlorin in 3-4 hours. In contrast, SnTCPP adsorbed onto TiO_2 at pH 4.5 is unchanged under ambient light, but ultimately photodegrades under more intense irradiation. This observation suggests that the more oxidatively stable porphyrins like SnTCPP, are more stable on TiO_2 than are electron-rich porphyrins like SnUroP. Under intense illumination with visible light, a similar result was noted for solutions of free SnUroP and SnTCPP.

The attachment of SnUroP to the semiconductor surface enhanced the destruction rate of SA as described below (see **Figures 2.7 and 2.8**). However, the SnUroP alone is photoactive and the determination of the degree of enhancement of TiO_2 photoactivity is complicated by the porphyrin-induced generation of a SA intermediate products (see **Figures 2.5, 2.7**) as described above. Control experiments in which SnUroP-sensitized TiO_2 was irradiated, in absence of SA, showed no additional peaks in the UV region. We conclude that there is no interference from the SnUroP degradation products. A second complication is caused by the dispersion of small TiO_2 particles in the pH range above 5. This increased UV absorption that is caused by fine TiO_2 dispersion is shown in **Figure 2.4(b)**. Examination of the porphyrin-induced dispersion phenomena is described below.

2.2.2. Porphyrin-Mediated Dispersion of TiO_2

An increase of UV absorbance (200-340 nm) resulting from dispersion of fine TiO_2 particles is demonstrated by UV-visible spectra of the porphyrin-treated TiO_2 samples shown in **Figure 2.4(b)**. The broad absorption band from 200 nm to 340 nm is attributed to the bandgap absorption of the porphyrin-stabilized dispersion of fine TiO_2 particles that cannot be removed

from solution by centrifugation. The dispersed fine particles represent only a small fraction of TiO_2 in the sample, but nevertheless exhibit the characteristic absorption band edge of TiO_2.

In the absence of porphyrin, dispersion of fine particles for P-25 grade TiO_2 occurs at high (>9) and low (<3) pH, but not in the pH range from 4 to 8. This is illustrated in **Figure 2.6**, where the absorbance due to the bandgap of the fine particles at 296 nm is plotted versus pH. The bandgap absorption is relatively flat at wavelengths less than 300 nm, so the absorption at 296 nm was used to quantify the concentration of dispersed TiO_2 (see **Figures 2.4(b) and 2.6**). High positive (low pH) or negative (high pH) charge on the surface apparently breaks up aggregates of small TiO_2 particles resulting in the observed colloidal dispersion in the pH regions far from 6, the point of zero (pzc) charge for TiO_2.[17]

The presence of SnUroP shifts the pH range in which dispersion occurs as illustrated in **Figure 2.6**. The dispersion is observed above pH 5, but not below. As the pH is lowered, the first of the eight acid substituents of uroporphyrin is protonated at about pH 6.6.[18] This is also the pH range in which SnUroP starts to be adsorbed onto the surface (see **Figure 2.6**). Although the aggregation of uroporphyrins typically is observed below pH 7 for four- and five-coordinate metal complexes, aggregation does not occur for six-coordinate metals like Sn.[18] This suggests that either (i) Sn uroporphyrin interacts dynamically with the surface in the pH range from 5 to 8 and the interaction results in the dispersion of TiO_2 or (ii) adsorption of SnUroP onto the surface in this range acts to maintain a high negative charge on the porphyrin modified surface. In the latter case for example, a $SnUroP^{-x}$ molecule (with $0 \leq x \leq 8$ acid groups deprotonated) might bind to a $-OH_2^+$ group on the surface changing the charge at that location from +1 to 1-x, i.e., the charge of the $-OH_2$-$SnUroP^{-x+1}$ surface group. Thus, for more than one deprotonated group on

the porphyrin, binding results in replacing the positively charged functional group with a negatively charged one.

Below pH 5, negatively charged carboxylate groups of the porphyrin molecule are attracted to regions of positive charge on the TiO_2 surface. However, binding of the porphyrin to the substrate now neutralizes the charged regions, preventing the electrostatic repulsion that might break up aggregates of small TiO_2 particles. This is because the porphyrin substituents are nearly all protonated (and 1-x is close to 0). The large aromatic ring of the porphyrin also acts to modify the surface properties of the TiO_2 particles in a way that may promote aggregation of these particles. For example, when fully coated with neutral porphyrins, the surface is more hydrophobic.

In the absence of SA, the porphyrin-mediated TiO_2 dispersion process at pH 6.0 as a function of irradiation time was followed. The absorption due to the dispersed TiO_2 rapidly disappears over the first 30 minutes of irradiation. This decrease in the amount of dispersed TiO_2 is most likely a result of the rapid destruction of the porphyrin, since TiO_2 dispersion does not occur at pH 6 unless porphyrin is present. Destruction of the porphyrin is also confirmed visually by the bleaching of the porphyrin adsorption bands in the photosensitized TiO_2.

SnTCPP does not appear to influence dispersion as strongly as SnUroP (data not shown). However, enhanced dispersion is found to occur in the region between pH 5 and pH 9, a region where bare P-25 grade TiO_2 dispersion is not observed. Finally, the presence of SA does not induce the dispersion of fine TiO_2 particles, nor does its presence effect the pH dependence of the porphyrin-induced dispersion process. Its presence however may influence the degree of dispersion.

2.2.3. Enhanced Photocatalytic Detoxification on TiO_2

Our primary goal is the enhancement of TiO_2 redox reactions to destroy toxins, by using the visible light absorbed by a photosensitizer. At wavelengths longer than 400 nm, weak absorption by the band edge in TiO_2 still produces electron-hole pairs in the semiconductor. These holes (and electrons) normally initiate the destructive redox chemistry. For the photosensitized TiO_2, absorption of visible light by the porphyrin results in the formation of the excited triplet state by analogy with homogeneous chemistry. The redox potentials of the porphyrin are altered in the excited state and these new potentially excited states are then available either (1) to interact with electrons and/or holes of TiO_2, (2) to add species like superoxide, hydroxyl radicals, etc. with different redox properties that can modify rates of destructive reaction pathways, or (3) to participate directly in detoxification redox reactions with SA.

Visible-light assisted reactions occurring in a solution containing SA and the porphyrin-sensitized TiO_2 were monitored as a function of irradiation time to determine if the destruction of SA was enhanced by the presence of the metalloporphyrin dye. UV-visible spectra of samples taken at various irradiation times for un-sensitized (bare TiO_2) and dye-sensitized systems are shown in **Figures 2.7(a) and 2.7(b)**, respectively. Both the SA/TiO_2 and SA/TiO_2/SnUroP mixtures were initially at pH 5; TiO_2 from Tioxide was used. It can be mentioned here that for both of the above mentioned experiments, a UV-filter (390 nm cut-off) was used to ensure the passage of photons where $\lambda \geq 390$nm.

For the SA/TiO_2 mixture, enough absorption into the edge of the conduction band occurs to generate electron-hole pairs so the destruction of SA occurs, but at a slower rate compared

with UV irradiation of the solution. Also, the rise in absorbance to the red of the 296-nm SA peak and in the valley (at about 260 nm) between the 296- and 230-nm peaks shows evidence of the formation of a SA degradation product. Note that clear isosbestic points are located on both sides of the 296 nm band, indicating the formation of a single SA degradation product that absorbs in the UV.

The destruction of SA by TiO_2/SnUroP systems results in a more complicated spectral profile as shown in **Figure 2.7(b)**. A much larger rise in the UV absorbance below 340 nm is observed. This likely results from the formation of a much greater concentration of the intermediate SA product. It is speculated that the intermediate is similar, if not the same, as the intermediate formed at a much lower concentration in the absence of the porphyrin. For instance, notice the rapid filling-in of the valley at 260 nm and the increase in the absorbance just to the red of the 296-nm SA band. The dispersion phenomenon described earlier may also play a role in increasing the UV absorbance, but should not be significant in the data obtained at pH 5 (**Figures 2.7(a) and 2.7(b)**) since only visible light is used for these cases. As discussed earlier and shown in **Figure 2.6,** the porphyrin-mediated dispersion of TiO_2 particles is at a minimum at pH 5. Additionally, the use of UV cut-off filter in these experiments has further minimized the electron-hole separation due to the bandgap excitation of TiO_2 particles.

Using the spectra illustrated in **Figures 2.7(a) and 2.7(b)**, the rates of destruction of SA were estimated and compared. The absorbance peak at 296 nm (without any background correction), a measure of the conversion and destruction of SA, is plotted as a function of irradiation time in **Figure 2.8** for photosensitized (TiO_2/SnUroP) and bare TiO_2. The rate of SA destruction is enhanced by SnUroP adsorption onto the TiO_2 when only visible light is used.

Difficulty in measuring the destruction rate is that the absorbance of the initial SA peak (at 296 nm) for the bare TiO_2 system is only 69% of the SA absorbance in the TiO_2/SnUroP system, indicating a competitive adsorption between SnUroP and SA onto the TiO_2 surface. In other words, in spite of the fact that the same concentration of SA (30 ppm) was added for both cases of bare and SnUroP-coated 0.1% TiO_2 suspension, 15 and 22-ppm SA were detected from the supernate aqueous mixture of TiO_2/SA and TiO_2/SnUroP/SA systems, respectively, at the beginning of the experiments. A larger fraction of the SA (50%) has adsorbed onto the bare TiO_2 surface because of the lack of competition with the other adsorbent SnUroP. Upon illumination, SA is destroyed on the surface, allowing more SA to adsorb from solution and, thus, contributes to the decrease in absorbance at 296 nm. The decrease in absorbance at 296 nm fits with a first-order rate of destruction of SA.

As mentioned above, despite the complication described above, it is clear that the rate of SA destruction is enhanced by SnUroP adsorption onto the TiO_2 when only visible light is used for the excitation source. The enhancement in the detoxification rate is apparent in the slope of the curve for the photosensitized TiO_2 within 30 minutes of illumination. The pseudo first order rate in the first 20 minutes is about 2.5 times faster than the destruction rate for bare TiO_2. The SA peak at 230 nm evolves in a similar way with illumination time. It should be pointed out here that in the case of an unfiltered light source of UV and visible photons the rate of destruction of SA on the bare TiO_2 was much higher than TiO_2/SnUroP system. This is because upon an exposure to UV light, unsupported metalloporphyrin decomposes rapidly and at even faster rate when adsorbed onto TiO_2 surface since the separated electrons and holes due to bandgap absorption attack porphyrin oxidatively directly.

The absorbance at 260 nm (A260) is predominantly a result of formation of the initial SA degradation product (**Figure 2.8**). In the absence of SnUroP, the absorbance shows a steady, slow increase over the first 60 minutes. In contrast, when SnUroP is present, A260 increases very rapidly to a maximum in the first 30 minutes and then decreases. Thus, the behavior of A260 indicates a strong increase in the initial rate of formation of the initial SA product followed by its further destruction at a rate consistent with that exhibited by bare TiO_2.

2.2.4. Photocatalytic Degradation by Al_2O_3-supported Sn Porphyrins

Alumina itself is nonconducting material and, thus, completely inert for any photoredox chemical processes. However, alumina is known to provide a catalytic surface for many chemical reactions.[19,20] Moreover, SnUroP and SnTCPP themselves possess the photoactivity in aqueous solutions as discussed earlier in this chapter. Ring reduced photoproducts of SnUroP like chlorin and florin were observed under visible light illumination and this process was enhanced when UV photons were combined with visible photons. Photoproducts of SA and AN were also observed when these target molecules were added to the porphyrin solutions in absence of any support materials (see **Figure 2.5**). SnUroP in solution converted the target molecules into some intermediate products, as determined from absorbance changes at 260 nm and 252 nm for SA and AN, respectively. It very likely that the photo-interactions between target molecules and SnUroP in solution are stoicheometric rather than catalytic. However, negligible photodegradation of SA or AN is observed with either the porphyrin or alumina alone. The disappearance (due to degradation) of characteristic absorption bands at 296 nm and 230 nm for SA and AN, respectively, occurs only when porphyrin is immobilized on the alumina surface.

Both SnUroP and SnTCPP, adsorbed onto aqueous suspensions of powdered Al_2O_3 at pH 6, were photocatalytically active toward oxidative degradation of SA and AN. When SA was added to the suspension of 0.2% Al_2O_3, an adsorption process took place similar to that observed in the case of TiO_2 (see above). Combining either of the two porphyrins, SnUroP or SnTCPP, with Al_2O_3 yields a colored Al_2O_3 powder which was indicative of the absorption of visible light by the adsorbed Sn porphyrin. Binding of porphyrins to the alumina surface occurred below the pzc of the surface (7.8 for alumina)[21] as shown in **Figure 2.9** and colored porphyrin-coated alumina powder was obtained when filtered and dried.

Aniline, the other target molecule, did not bind to the alumina surface presumably due to the same reason it did not bind to the titania surface. **Figure 2.10** shows the photodegradation of SA and AN when SnUroP/Al_2O_3 catalyst was used under UV and visible light irradiation. Use of either filtered ($\lambda > 390$ nm) or unfiltered UV light in these experiments with porphyrin-coated alumina did not make a considerable difference in the rate of photodegradation, although a modest increase in the initial rate was observed when a combination of UV and visible light was used instead of visible light only. This is because alumina is a passive material that provides a surface for the porphyrin which remains photostable even under UV irradiation.

The time-dependent plots of the disappearance of SA and AN under various illumination conditions are shown in **Figures 2.11 and 2.12**, respectively, when Al_2O_3/SnUroP catalyst was used. The rapid disappearance of the SA absorption band at 296 nm is observed. To test whether the disappearance is due to photo-induced adsorption of SA onto the alumina surface, similar photo-experiments were performed after replacing the target SA with AN which does not adsorb onto the surface under the experimental conditions. Thus, the disappearance of the AN

absorption band must result from SnUroP-mediated photocatalysis (see **Figure 2.12**). However, a brownish yellow and oily layer on the surface of the suspension was observed which was removed during filtration process for subsequent spectral analysis. This apparently photo-induced polymerization of aniline was not observed unless SnUroP was immobilized onto Al_2O_3. The mineralization of SA and removal of AN were also analyzed with total organic carbon (TOC) analyzer (data not shown) which supported the above results.

The degradation of the target molecule AN is limited by the formation of an intermediate (absorption band at 252 nm), which is evidently less susceptible to photodegradation. This intermediate is presumably similar to the photochemical polymerization product of aniline (AN) identified in previous electrochemical studies.[22,23] When UV and visible photons are used together, however, the initial rate of disappearance of the AN peak at 230 nm on the Al_2O_3/SnUroP surface is faster than that on bare TiO_2 under similar experimental conditions. No intermediate formation is observed on the TiO_2 surface.

The commonly used photocatalyst for solar detoxification, TiO_2, shows very little activity for the destruction of AN under visible light irradiation. Photo-induced removal rates of AN using both UV and visible light are similar for bare TiO_2 and SnUroP/Al_2O_3 systems (**Figure 2.12**). Addition of UV light only marginally increases the activity of the porphyrins supported on alumina. However, the formation of a yellowish brown oily semisolid compound from the target AN on the surface of the reaction admixture during the course of photo-experiment can not be considered as photodegradation, but rather photocatalytic polymerization.[22]

A comparison between the activities of photodestruction of SA and AN by porphyrin adsorbed photocatalysts onto TiO_2 and Al_2O_3 surfaces are shown in **Figure 2.13** for similar

experimental conditions. It is clear from this figure that SnP/Al_2O_3 system offers a more efficient and stable photocatalytic system than SnP/TiO_2. Although enhanced photoactivity was observed with SnP/TiO_2 compared to that of bare TiO_2, the porphyrin was unstable under illumination.

2.2.5. Effect of Molecular Oxygen

When the experiments which provided **Figures 2.11, 2.12 and 2.13** were repeated in the absence of O_2 under a nitrogen atmosphere, no degradation of SA and AN were observed. This suggests that O_2 is required for both destruction of SA and formation of the SA intermediate species on both SnUroP/TiO_2 and SnUroP/Al_2O_3. SnUroP is known to photosensitize the formation of singlet O_2 with quantum yield of 0.6.[24,25] Thus, singlet oxygen could be involved in formation of the SA intermediate. The bare TiO_2 surface also requires oxygen for the destruction of SA and other target organic molecules. This requirement is maintained in the presence of dyes as well.

2.2.6. Mechanisms of Sn Porphyrin-Based Photocatalysis

A number of possible mechanisms could lead to enhancement of photocatalytic activity. First, the absorption of visible light by the porphyrin could lead to a redox cycle that generates reactive porphyrin species (e.g., the anion and/or cation) that directly attack SA. Evidence for such a process is found in the rapid conversion of SA to some species regardless of whether TiO_2 is present or not. The enhancement would then be explained if the SA product is more labile than SA.

A second mechanism of photosensitization involves the removal of conduction band electrons by reduction of the porphyrin triplet state at +1.1 V vs. NHE. Removal of electrons from TiO_2 would prevent rapid electron-hole recombination, leaving the strongly oxidizing hole

for reaction with either adsorbed SA or with hydroxyl ion. Both of these pathways lead to the destruction of SA.[13,14] This is equivalent to the enhancement observed when metal ions and other additives are used to extract conduction band electrons from TiO_2.[15] This mechanism would be consistent with the production of reduced porphyrin products. Reduction of Sn porphyrins is known to result in a long lived radical anion (at -0.66 V for SnUroP) that eventually decomposes unless it is re-oxidized soon to the neutral porphyrin. Indeed, inclusion of methyl viologen, an electron acceptor (-0.45 V) does seem to protect the porphyrin from degradation beyond the Sn chlorin.

Enhancement mechanisms involving porphyrin oxidation chemistry via the oxidation of either the triplet state at -0.13 V or the neutral porphyrin at >1.64 V by valence band holes also cannot be ruled out. Most likely, either oxidative or reductive reactions of the porphyrin initiate the destruction of the porphyrin. Determination of a complete mechanism of porphyrin degradation on TiO_2 will allow us to design more stable photosensitizers.

Irradiation under anaerobic conditions shows that oxygen is necessary for the photodegradation reaction to occur for both SA and AN with SnP/Al_2O_3. This indicates that both SA and AN are degraded by an oxidative pathway possibly similar to that involved in detoxification with bare TiO_2. In TiO_2-based photocatalysis, molecular oxygen consumes conduction band e- to form superoxide ion which interacts with hydroxyl anion to form the hydroxyl radicals necessary for oxidative destruction. Similarly, tin porphyrin anion on Al_2O_3 can release an electron to O_2 for simultaneous reoxidation of the porphyrin molecule and formation of superoxide. The initial reduction of porphyrin is likely through the donation of electron from SA

or AN, the target molecules. A schematic diagram of electron transfer between the excited SnUroP and other reactive species are shown in **Figure 2.14**.

The total photodegradation of organic compounds by porphyrin photocatalysts on alumina is limited by competition between the oxygen molecule and the organic molecule for the photoexcited triplet state of the photocatalyst.[26] A schematic diagram for this competition is shown in **Figure 2.15**. Upon photoexcitation of a metalloporphyrin molecule, an excited porphyrin triplet state is formed that can either react with an oxygen molecule to form a singlet oxygen or react with an organic target like AN to form a negatively charged porphyrin through the oxidation of AN. The reduced porphyrin molecule can further react with molecular oxygen to produce superoxide which attacks target organic molecules resulting in oxidative degradation or polymerization. This process returns the porphyrin molecule to its ground state. Consequently, the porphyrin follows a photocatalytic cycle with an oxidative attack on the target organic molecule. The rate constant k for the formation of singlet oxygen[26] is 10^9 M^{-1} s^{-1} and if the rate constant k' for the formation of reduced porphyrin is assumed to be same as k, the second pathway of the formation of the superoxide is dominant only when the AN concentration is higher than the molecular oxygen concentration. Otherwise, the triplet porphyrin excited state forms a oxidized porphyrin cation which is susceptible towards degradation. However, the lack of oxygen forbids the formation of superoxide necessary for the expected oxidized species from the target molecule. Since the ambient oxygen concentration is 0.2 mM, the concentration of AN needs be maintained greater than 0.2 mM. According to this scheme, the depletion of target molecules to a level lower than 0.2 mM would greatly slow down the oxidative degradation of the target molecule. This suggests that total degradation of all target molecules is not practically achievable at ambient oxygen pressure; this is consistent with our results. In contrast, the absence of oxygen

will terminate the process completely which is also consistent with our results. This mechanism matches the general consensus that the formation of the superoxide ion is the driving force for the ultimate photodegradation of organic compounds.

The above mechanism is yet to be proven with further evidences. The complex nature of photophysical and photochemical processes at the interface and photo-induced changes in target molecules make it difficult to derive a generic mechanism from our results. More systematic experiments are required for the verification of the above mentioned explanations. One way to approach is to perform the studies in a gas-phase reactor with an on-line GC/MS system as well as Raman spectroscopy. GC/MS system can be useful in probing and identifying the reaction intermediates while Raman can be useful in probing the transient species in a homogeneous reaction solution.

2.3. Conclusions

Two tin porphyrins were investigated with regard to their ability to enhance the destruction rate of salicylic acid (SA) and aniline (AN) when they are adsorbed onto semiconducting TiO_2 and non-conducting Al_2O_3. Adsorption occurs below the point of zero charge of the respective oxides. Interaction of porphyrins with TiO_2 modifies the colloidal properties of TiO_2 particles. Porphyrin-modified TiO_2 shows enhanced ability to photocatalytically destroy SA and AN. The complete mechanism of enhancement remains to be determined, although this study confirms previous literature reports that the presence of O_2 is a requirement in detoxification reactions independent of the nature of the supporting particles.

Tin porphyrins are destroyed during the detoxification reactions when supported on TiO_2. SnTCPP shows greater stability than SnUroP on TiO_2. The photodestruction of adsorbed

porphyrins was minimized when a nonconducting alumina support is used. In this case, Sn porphyrins still function as photocatalysts for the destruction of SA and AN, but the proposed photochemical mechanisms clearly differs from those operative in aqueous solutions of SnPs. In addition, the initial rates of photodegradation of SA and AN on SnP-coated Al_2O_3 are much higher than that on the bare TiO_2 when both UV and visible photons are used. However, the differences are more dramatic when only visible light ($\lambda \geq 390$ nm) is used. The photocatalytic activity of SnUroP/Al_2O_3 was retained even after recycling with fresh SA or AN.

Formation of intermediate photoproducts is more pronounced in SnUroP/Al_2O_3 than in the case of bare TiO_2. This observation indicates a potential for the development of a mixed support of TiO_2 and Al_2O_3 for dye molecules. The behaviors of metalloporphyrins on a mixed support of TiO_2 and Al_2O_3 will be the determining factor for a successful utilization of visible photons.

The mechanisms of photocatalytic destruction on oxide surfaces, especially when dye molecules are involved, are not quite understood yet. Further experiments in aqueous phase are necessary to evaluate the proposed mechanisms. Also, detofification experiments in gas phase would provide answers to some of the developed questions from the aqueous phase experiments. Immobilization of porphyrins in new supports like zeolites can also be pursued for their stability and activity.

2.4. Figures

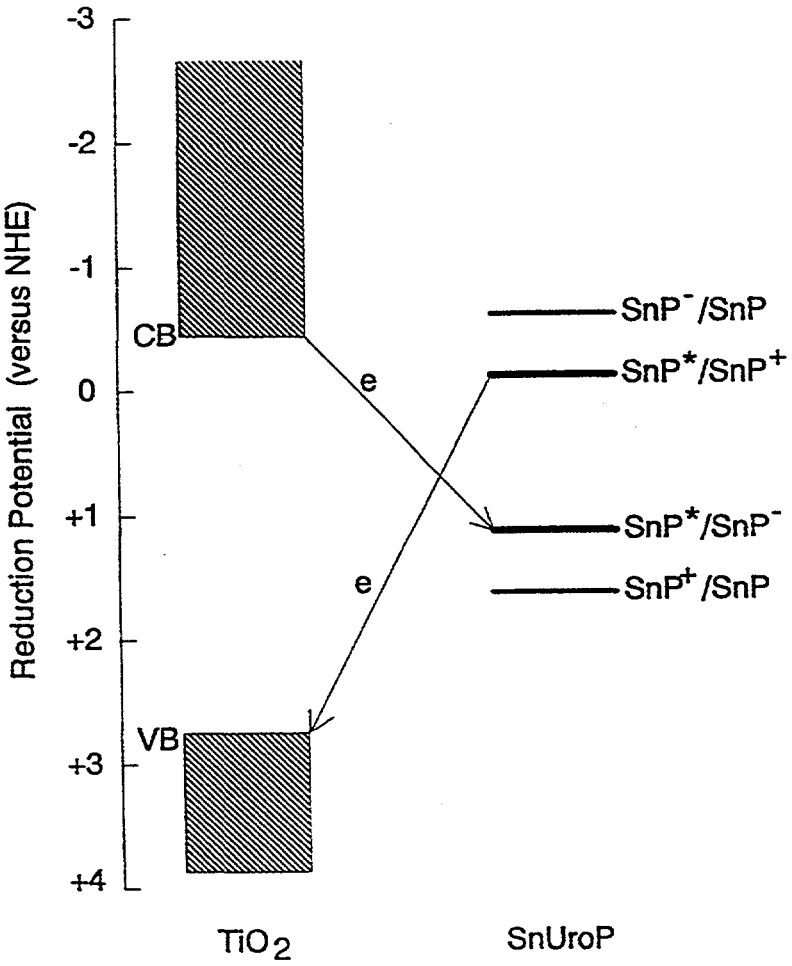

Figure 2.1. Energy levels of Sn porphyrin (SnP) states in relation to TiO_2 bands.

Sn(IV) Tetra(p-carboxyphenyl)porphyrin

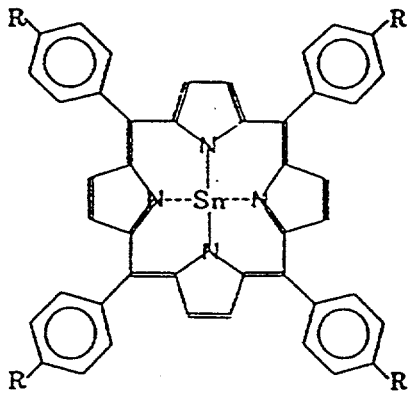

R = -COOH

Sn(IV) Uroporphyrin

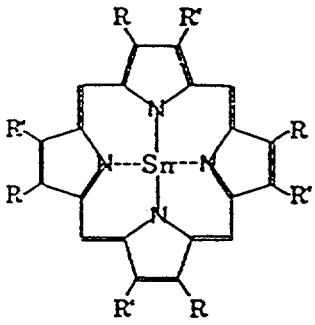

R = $-CH_2CH_2COOH$
R' = $-CH_2COOH$

Figure 2.2. Structures of tin porphyrins (SnPs) used for the current studies of photocatalytic degradation of organic molecules.

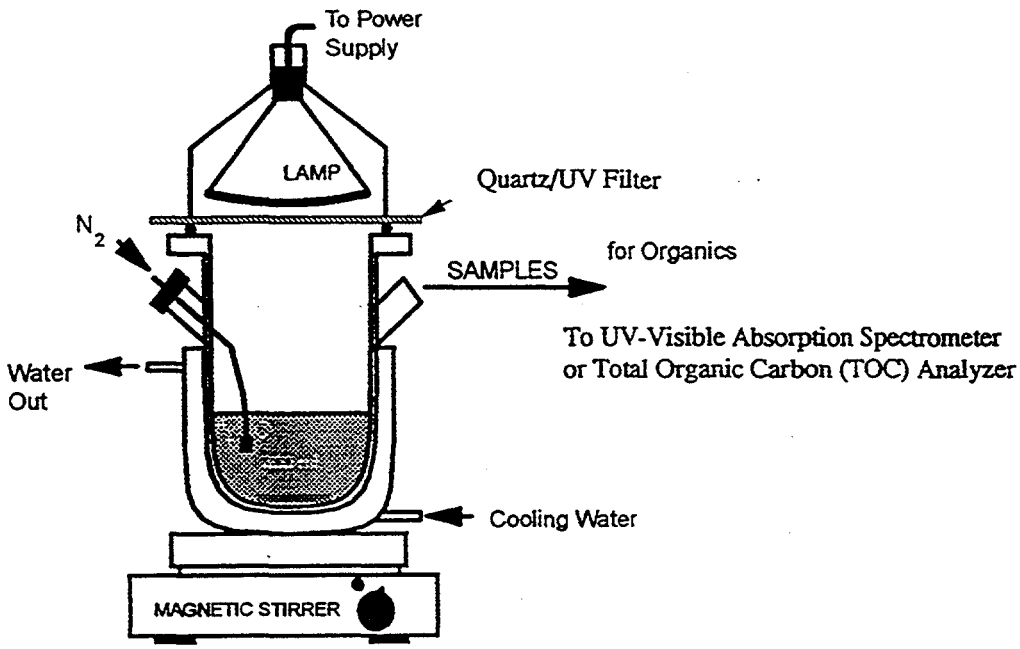

Figure 2.3. Schematic diagram of the laboratory batch (pot) photoreactor.

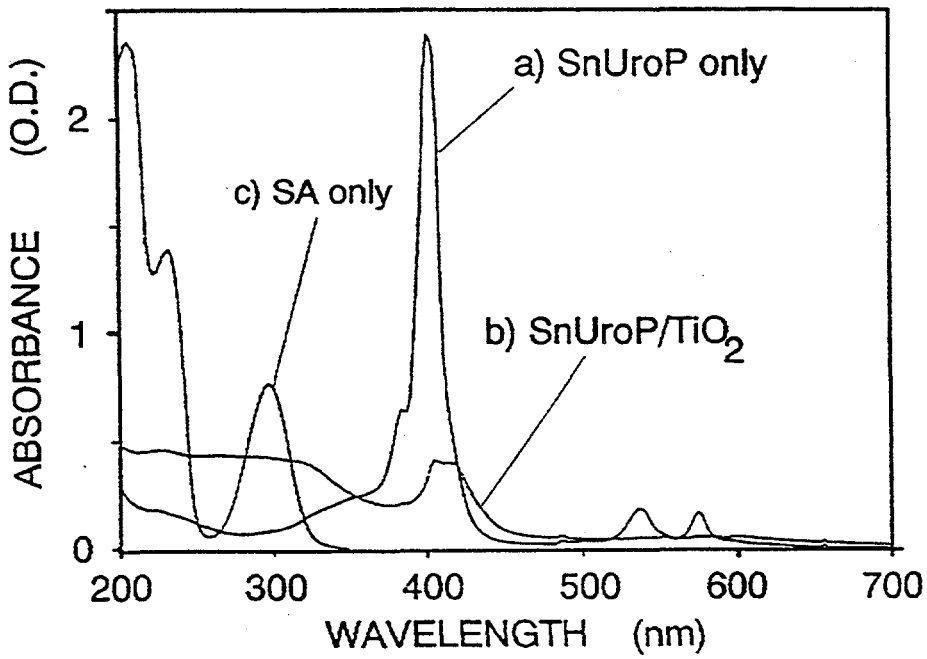

Figure 2.4. Absorption spectra of (a) SnUroP, (b) photosensitized by adsorption of SnUroP, and (c) salicylic acid only at pH 6.

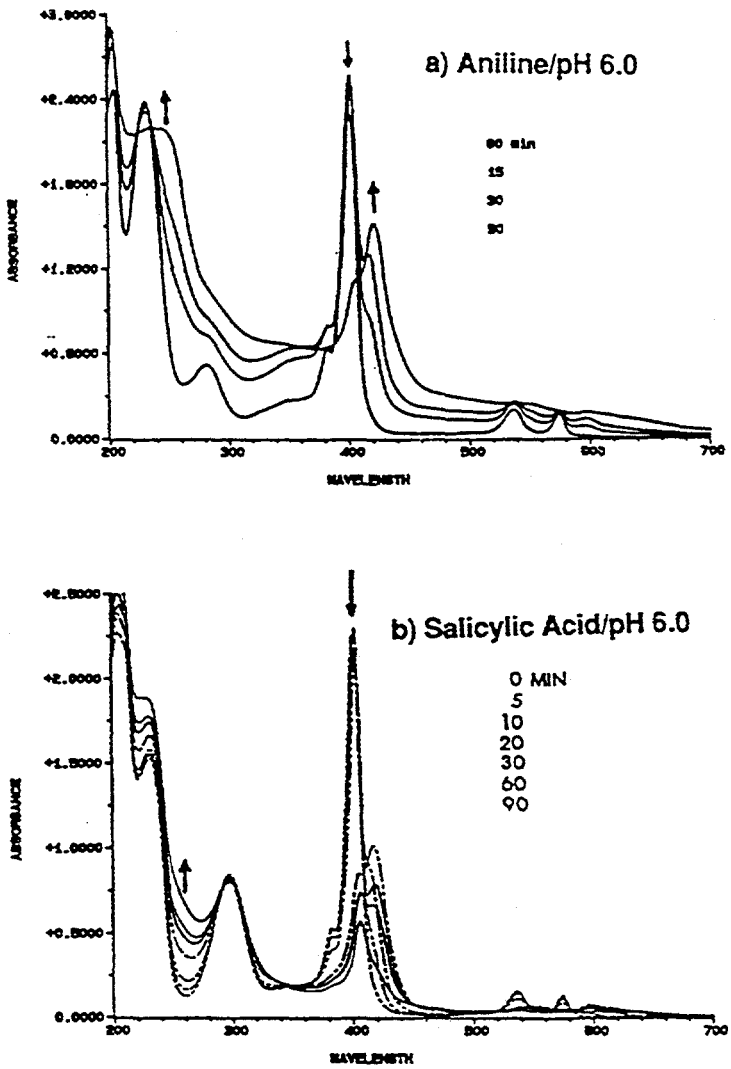

Figure 2.5. Photocatalytic activity of SnUroP (without any support) under a visible light ($\lambda >$ 390 nm) illumination. Absorption spectra of solutions of uroporphyrin (SnUroP) containing either (a) aniline (AN) or (b) salicylic acid (SA), in absence of any support, showing the photocatalytic conversion of salicylic acid. pH of both suspensions were 6.0 and illumination periods are shown for each samples.

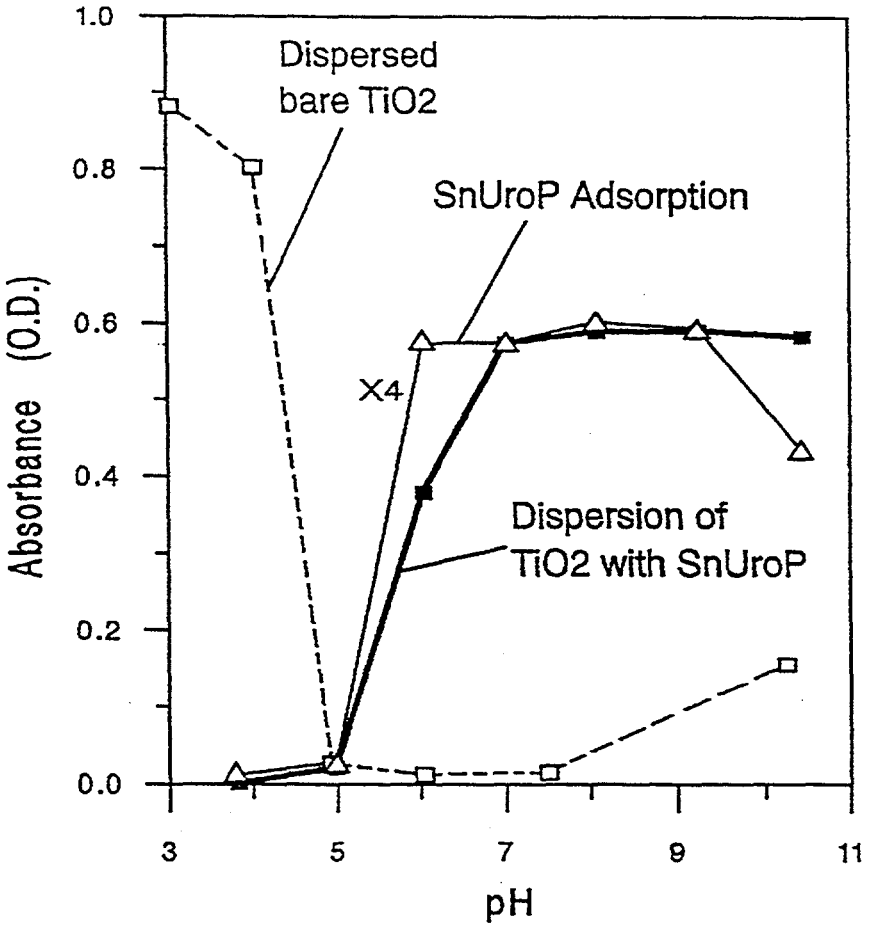

Figure 2.6. pH dependence of the dispersion of small TiO_2 particles for bare TiO_2 (broken line) and for TiO_2 coated with SnUroP (bold solid line, measured by the conduction band absorbance at 296 nm), and the adsorption of SnUroP onto TiO_2 (thin solid line, measured by the Soret band absorbance at 402 nm of the SnUroP remaining in solution).

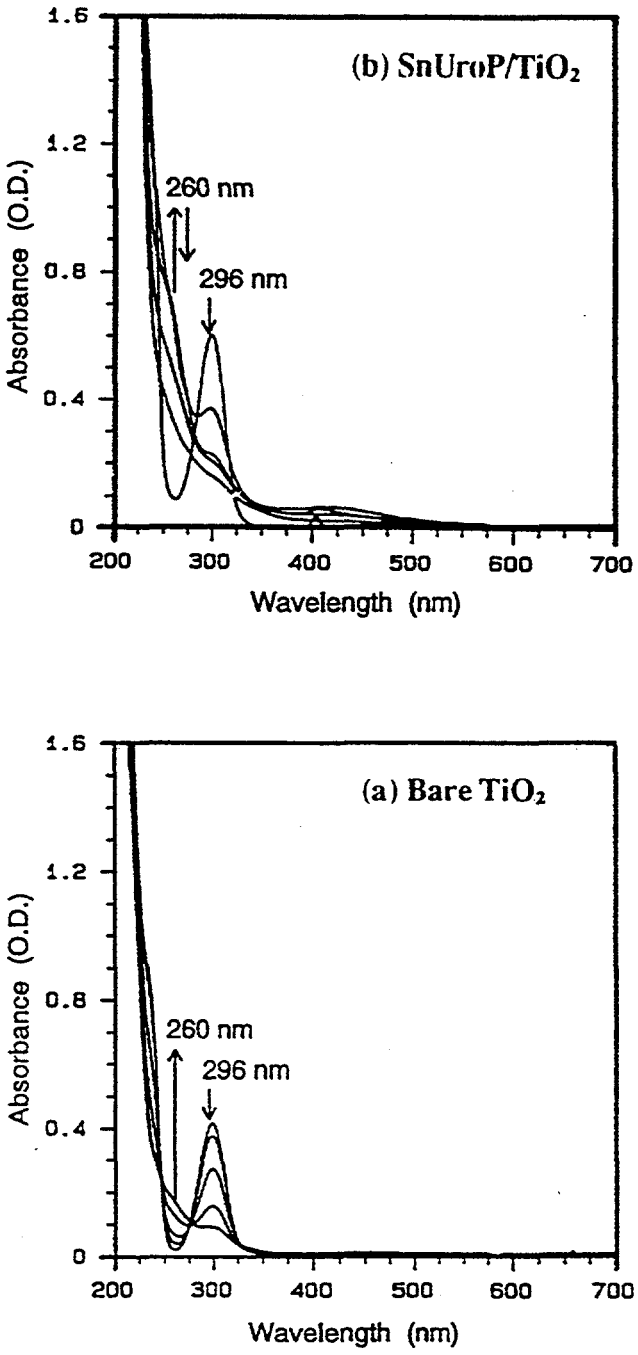

Figure 2.7. Change in the UV-visible absorption spectrum upon irradiation of aqueous mixtures of (a) colloidal TiO_2 and salicylic acid at pH 5 (SA/TiO_2) and (b) SnUroP-modified colloidal TiO_2 and salicylic acid at pH 5 (SA/TiO_2/SnUroP). Spectra are taken at 0, 5, 20, 40, and 60 minutes.

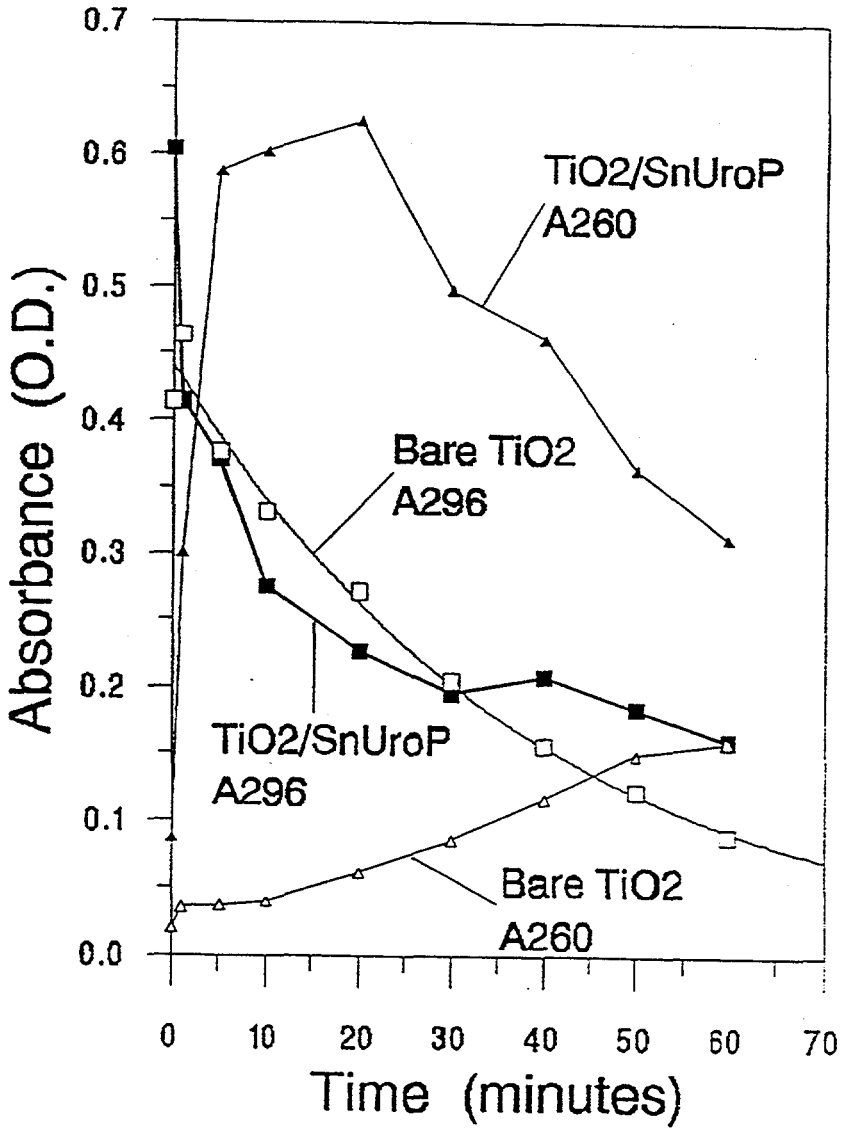

Figure 2.8. Enhancement of salicylic acid detoxification using SnUroP as a photosensitizer. Salicylic acid absorbance at 296 and 260 nm (1-cm cell) is plotted against irradiation time. The curve through the data points for bare TiO_2 at 296 nm is an exponential fit.

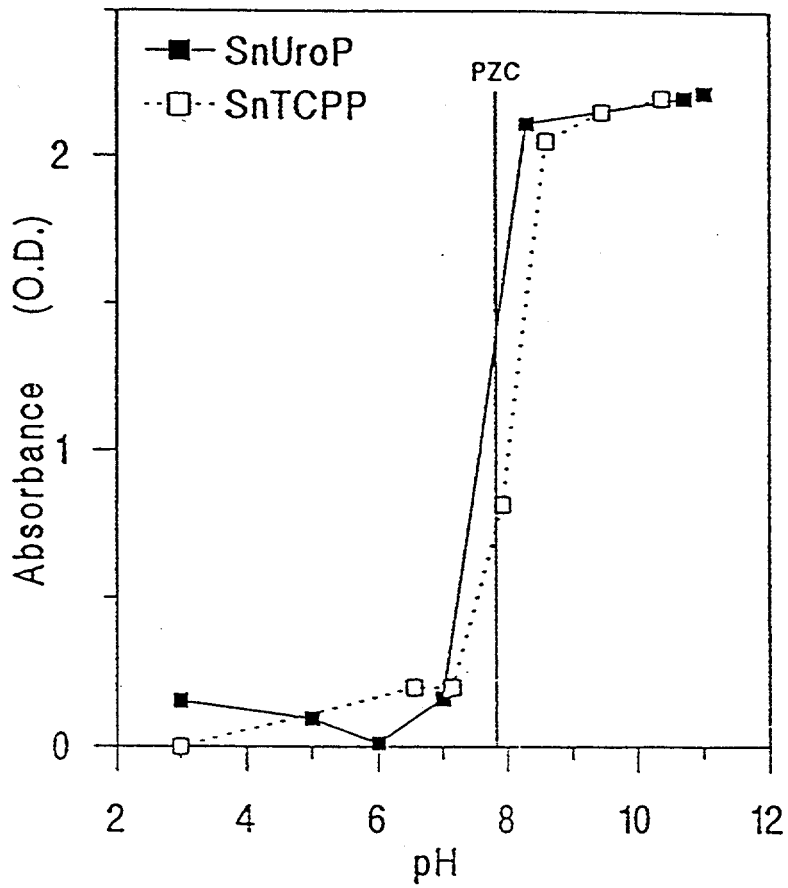

Figure 2.9. pH dependence of the adsorption of SnUroP (solid line) and SnTCPP (broken line) onto Al_2O_3 (measured by the Soret band absorbance, 402 nm and 422 nm for SnUroP and SnUroP respectively, remaining in solution). The point of zero charge (PZC) of Al_2O_3 is also shown by the vertical line at pH 7.8.

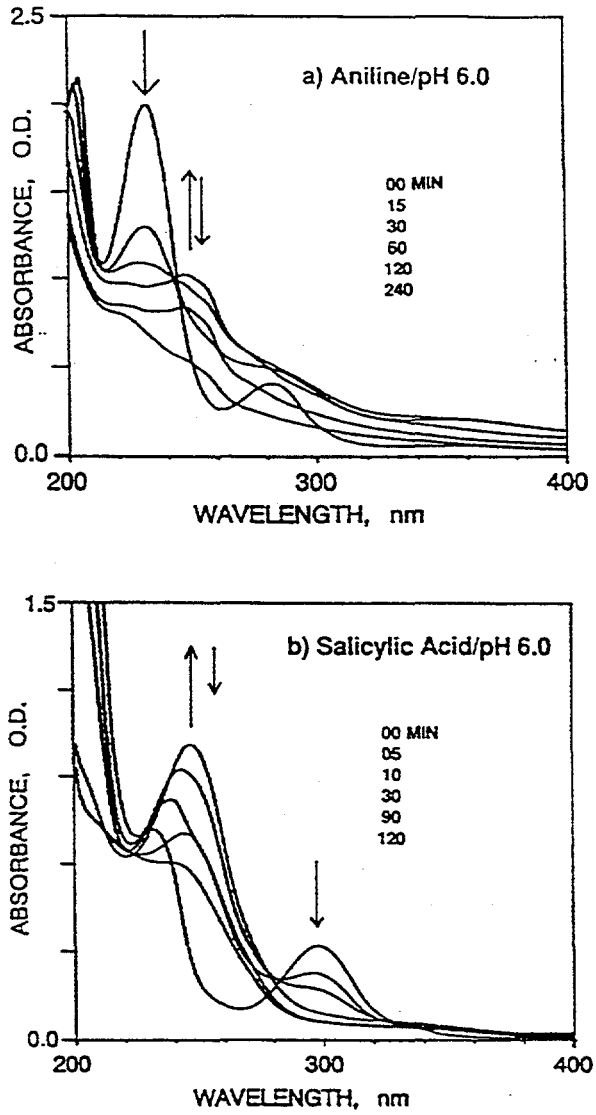

Figure 2.10. a) Photo-induced removal of aniline and b) photodegradation of salicylic acid by SnUroP adsorbed onto Al_2O_3 under UV and visible light illumination. The pH of both suspensions were 6.0 and illumination periods are shown for each samples.

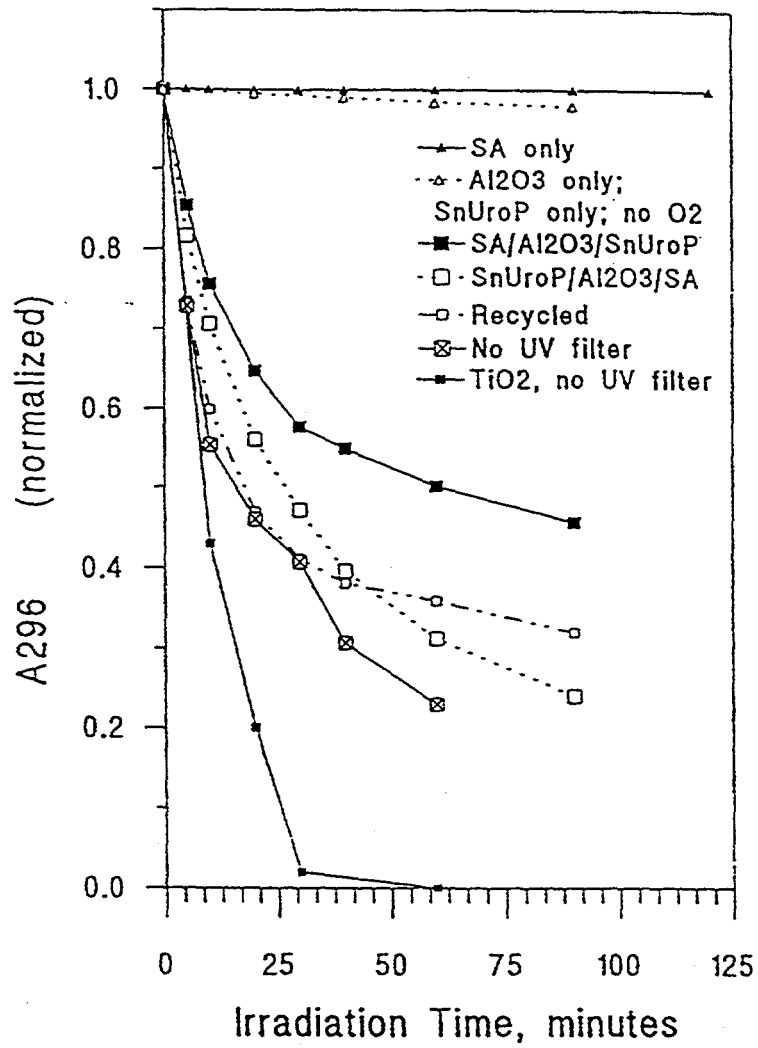

Figure 2.11. Photodegradation of salicylic acid (SA) using SnUroP as a photocatalyst on Al_2O_3. Normalized values of SA absorbance at 296 nm (1-cm cell) are plotted against irradiation time. No UV filter was used for the two bottom curves. The bottom curve with bare TiO_2 under UV and visible light irradiation is shown for comparison.

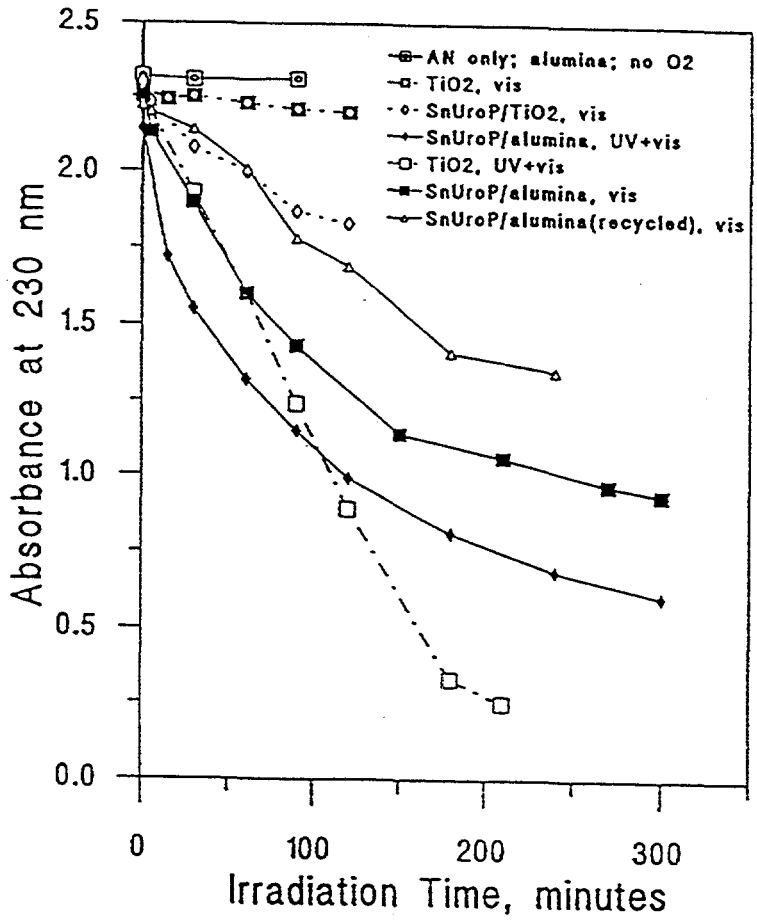

Figure 2.12. Photodegradation of aniline (AN) using SnUroP as a photocatalyst on Al_2O_3. Normalized values of AN absorbance at 230 nm (1-cm cell) are plotted against irradiation time. The bottom curve with bare TiO_2 under UV and visible irradiation is shown for comparison. The broken lines are referred to TiO_2 data under different conditions as indicated.

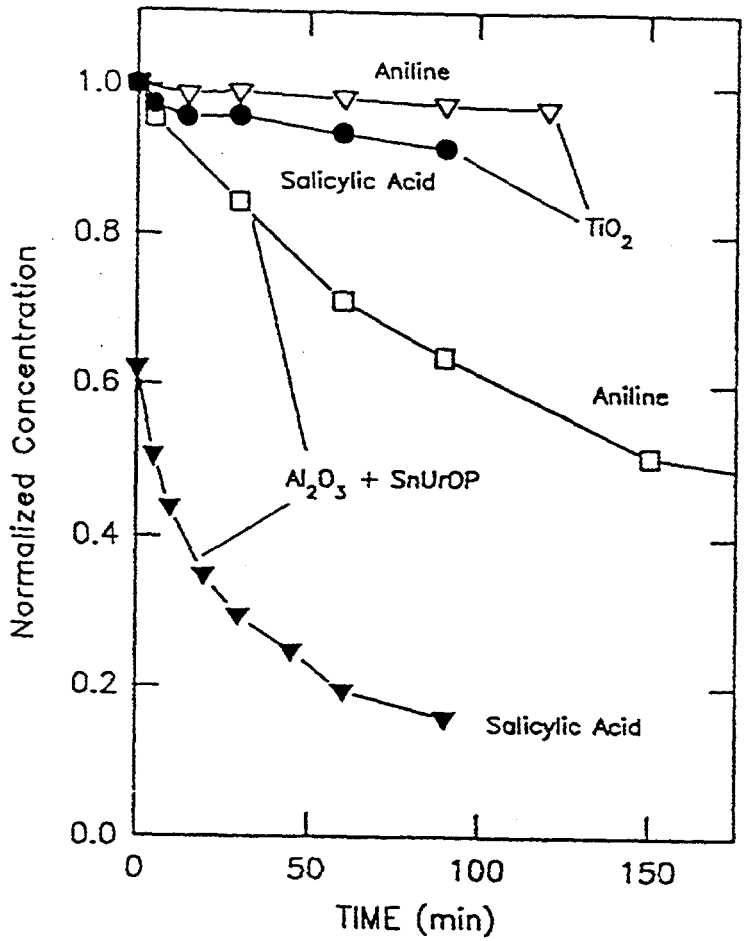

Figure 2.13. Photodegradation of salicylic acid (SA) and photo-induced removal of aniline (AN) by bare TiO_2 and $SnUroP/Al_2O_3$ photocatalysts using visible light only. Normalized values of absorbance from SA and AN are plotted against irradiation time as described in **Figures 2.11** and **2.12**.

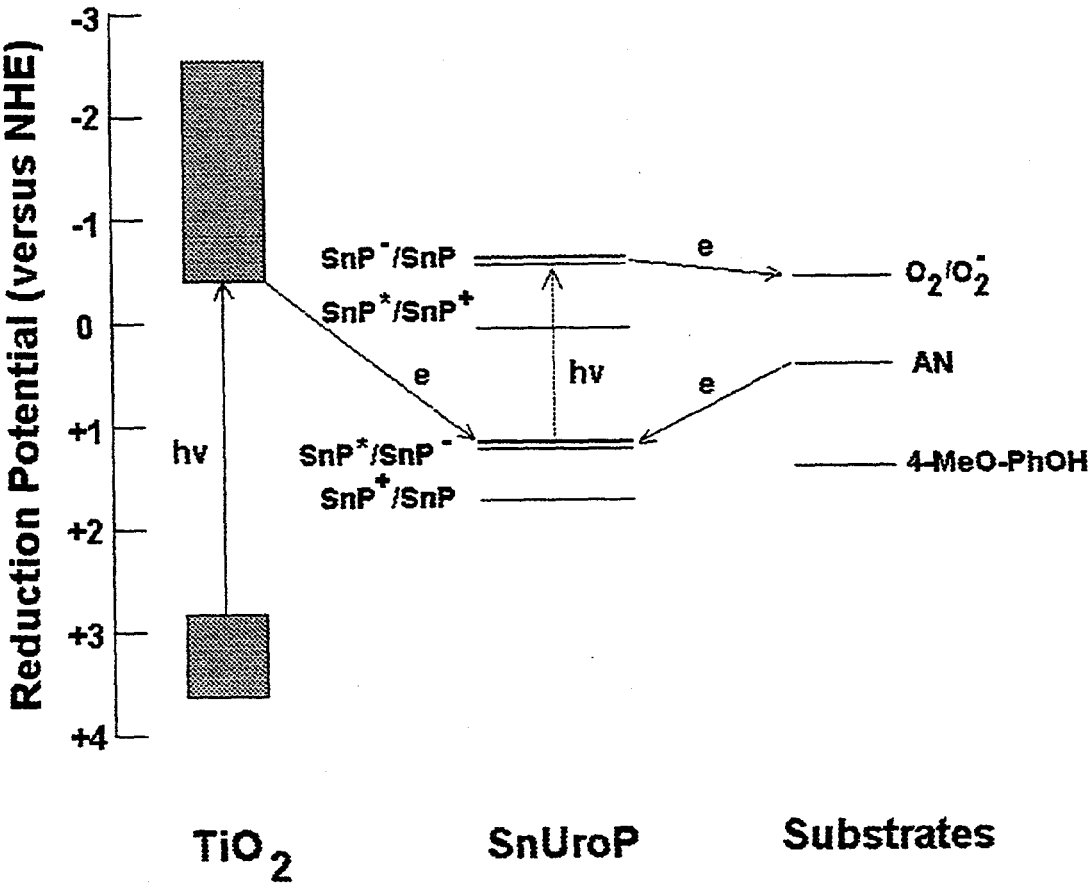

Figure 2.14. Schematic diagram for probable electron transfer between the excited states of SnUroP and other reactive species.

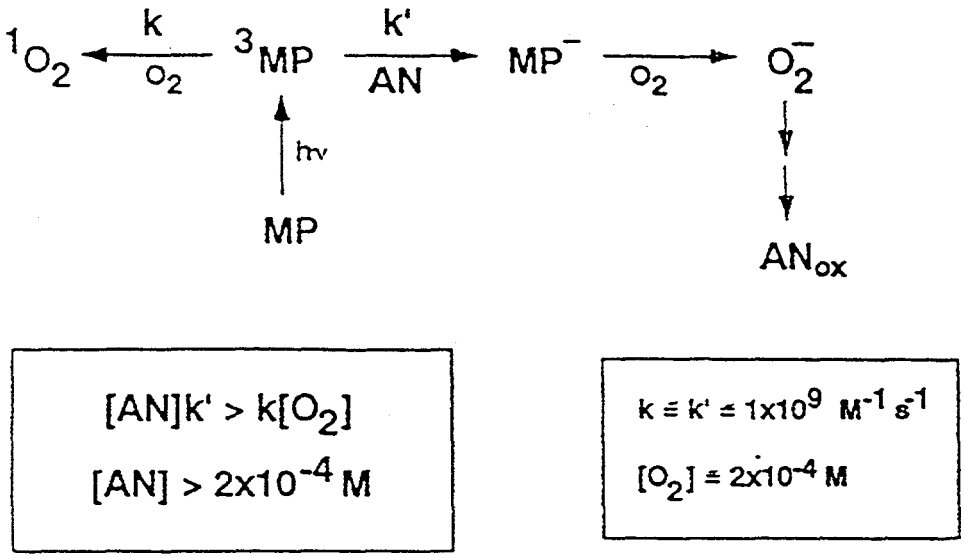

Figure 2.15. Probable mechanism of metalloporphyrin (MP)-initiated oxidative photodegradation or photo-induced removal of aniline (AN) on Al_2O_3.

2.5. References

1. Kadish, K.M.; Dubois, D.; Barbe, J.-M.; and Guilard, R. *Inorg. Chem.* **1991**, *30*, 4498.

2. (a) Kalyanasundaram, K.; Vlachopoulos, N.; Krishnan, V.; Monnier A.; and Gratzel, M. *J. Phys. Chem.* **1987**, *91*, 2342. (b) Kalyanasundaram, K.; Shelnutt J. A.; and Gratzel, M. *Inorg. Chem.* **1988**, *27*, 2820. (c) *Heterogeneous Photochamical Electron Transfer*; Gratzel, M.; CRC Press: Boca Raton, FL, 1989.

3. Pautet, F.; Daudon, M. *Tetrahedron Letters*, **1991**, *32*, 1457.

4. Majumder, S.A.; Prairie, M.R.; Ondrias, M.R.; and Shelnutt, J.A.; In *Solar Engineering*; Stine, W.; Kreider, J; and Watanabe, K., Eds.; Am. Asso. Mech. Eng. Book No. G0656A, **1992**, 9.

5. Fan, F.R.F.; Bard, A. J. *J. Am. Chem. Soc.* **1979**, *101*, 6139.

6. (a) Andreu, P.; Galiasso, R.; Morales, A.; Abrams, O.; Katan, O.; Pantoja, L.; Sojo, P.; and Vergara, E. *Proc. 7th Int. Congress on Catal.*, Tokyo, **1980**, *2*, 877. (b) Morales, A.; Galiasso, R. *Fuel*, **1982**, *61*, 13.

7. (a) Fukuzumi, S.; Mochizuki, S.; and Tanaka, T. *Isr. J. Chem.* **1987**, *28*, 29. (b) Kameyama, H.; Suzuki, H.; Amano, A. *Chem. Lett.* **1988**, 1117. (c) Battioni, P.; Lalier, J.P.; Barloy, L.; and Mansuy, D. *J. Chem. Soc., Chem. Commun.* 1989, 1149. (d) Barloy, L.; Battioni, P.; and Mansuy, D. *Ibid.* **1990**, 1365. (e) Nakamura, M.; Tatsumi, T.; and Tominaga, H. *Bull. Chem. Soc, Jpn.* **1990**, *63*, 3334. (f) Amadelli, R.; Bregola, M.; Carassiti, V.; and Maldotti, A. *J. Chem. Commun.* **1992**, 1355.

8. Moser, J.; Gratzel, M. *J. Am. Chem. Soc.* **1984**, *106*, 6557.

9. Fox, M.A.; Dulay, M.T. *Chem. Rev.* **1993**, *93*, 341.

10. Giraudeau, A.; Fan, F.R.F.; and Bard, A.J. *J. Am. Chem. Soc.* **1980**, *102*, 5137.

11. Kamat, P.V.; Fox, M.A. *Chem. Phys. Lett.* **1983**, *102*, 379.

12. Felton, R.H.; In *The Porphyrins*, vol. 5, Chapter 3, **1978**.

13. Mathews, R.W. *Wat. Res.* **1986**, *20*, 569.

14. Turchi, C. S.; Ollis, D. F. *J. Catal.* **1990**, *122*, 178.

15. Prairie, M.R.; Pacheco, J.E.; and Evans, L.R.; In *Solar Engineering*; Stine, W.; Kreider, J; Watanabe, K., Eds.; Am. Asso. Mech. Eng. Book No. G0656A, **1992**, 1.

16. Smith, K. M.; In *Porphyrin and Metalloporphyrins*, Smith, K. M.; Ed.; Elsevier Scientific Publishing, Amsterdam, **1975**; Chap. 1.

17. James, R. O., Stiglich, P. J., and Healy, T. W.; In *Adsorption from Aqueous Solutions*, P. H. Tewari, Ed.; Plenum Press, New York, **1981**, p. 19.

18. Shelnutt, J.A.; Dobry M. M.; and Satterlee, J.D. *J. Phys. Chem.* **1984**, *88*, 4980.

19. McNulty, G.S.; Cannon, K.; Schwartz, J. *J. Mol. Catal* **1981**, *11*, 397.

20. Dufour, P.; Houtman, C.; Santini, C.; Nedez, C.; Basset, J.M.; Hsu, L.Y.; and Shore, S,G. *J. Am. Chem. Soc.* **1992**, *114*, 4248.

21. Mieth, J.A.; Schwarz, J.A.; Huang Y.-J.; and Fung, S.C. *J. Catal.* **1990**, *122*, 202.

22. Mohilner, D.M.; Adams, R.N.; and Argersinger, Jr., W. J. *J. Am. Chem. Soc.* **1962**, *84*, 3618.

23. Yoneyama, H.; Takahashi, N.; and Kuwabata, S. *J. Chem. Commun.* **1992**, 716.

24. (a) Reddi, E.; Jori G.; and Rubaltelli, F. F. *J. Photochem. Photobiol. B: Biol.* **1991**, *8*, 159. (b) Kimel, S.; Tromberg, B.J.; Roberts, W.G.; and Berns, M.W. *Photochem. Photobiol.* **1989**, *50*, 175. (c) Cannistraro, S.; Jori, G.; and Vorst, A.V. *Photochem. Photobiophys.* **1982**, *3*, 353. (d) Venkatesan, R.; Periasamy, N.; and Srivastava, T. *Proc. Indian Acad. Sci.* **1992**, *104*, 713.

25. Shelnutt, J. A. *United States Patent 4,568,435*, **1986**.

26. Foote, C.S.; Doiron, D.R.; and Gomer, C.J., Eds.; Alan R. Liss Inc., New York, **1984**; p. 3.

Chapter 3

Synthesis and Spectroscopic Characterization of Octaacetic Acid-Tetraphenylporphyrins

3.0. Introduction

Metalloporphyrins with larger binding pockets and more dissociable peripheral groups are of great interest because they can provide more efficient electron transfer from the dye to the target molecules. The porphyrin core is increasingly distorted with the increase of the number of peripheral substitution. There is also current interest in the chemical and physical properties of nonplanar porphyrins and hydroporphyrins. In particular, nonplanar distortions of the macrocycle which result from steric interactions among the peripheral substituents have been investigated in order to understand the electron-transfer to their immediate environments.[1-3] These nonplanar structural distortions include the ruffled and/or saddle structures of the porphyrin macrocycle defined by Scheidt and Lee.[4] These nonplanar distortions are predicted to influence chemical processes such as the binding and release of axial ligands, redox properties of the porphyrin and the central metal ion, and electron-transport properties.[5-8] The inherent nonplanar structures of nickel porphyrins are particularly interesting and these nickel containing macrocycles have been investigated intensively in last decade since they provide relatively simple models for testing the effects of environmental and peripheral perturbations on the geometry of the porphyrin macrocycle.

This chapter describes the syntheses and physical properties of tetraphenylporphyrins possessing eight acetic acid groups at the β-pyrrole positions and the methylesters. The deprotonated free acid forms of these porphyrins are soluble in water. These porphyrins are highly nonplanar as a result of the steric crowding of the twelve peripheral substituents. The only other reports[9,10] on the synthesis of water-soluble porphyrins that are significantly distorted from planarity include octabromo- and octachloro-meso-tetrakis-(sulfonatophenyl)porphyrins and their

manganese and iron derivatives. However, these octahalogenated tetraphenylporphyrin derivatives are somewhat less sterically hindered and thus predicted to be less than the OAATPP derivatives described here (unpublished molecular mechanics results). In particular, the effects of nonplanarity on the physical properties of Ni(II) derivatives of octaaceticacid-tetraphenylporphyrin (**4:** OAATPP), its octamethylester (**3:** OAATPP-OME), octahydroxyethyl-tetraphenylporphyrin (**5:** OHETPP), and octaaceticacid-tetra(*p*-nitrophenyl)porphyrin-octamethylester (**6:** OAATNPP-OME) were investigated. The structures of these new porphyrins are shown in **Figure 3.1**.

Resonance Raman and UV-visible absorption spectroscopies were used to investigate the π–π aggregation behavior of nonplanar NiOAATPP in aqueous solution. The spectroscopic results for NiOAATPP are compared to the results for metallouroporphyrins (MUroPs) whose π–π self-aggregation[11-15] and π–π complex formation[14-17] have been investigated in detail. The MUroPs are convenient for such studies because they can exist in both aggregated and un-aggregated forms. The lack of appreciable aggregation of metal uroporphyrins at high pH (pH > 8) or at low concentrations (< 0.01 M) is attributed to electrostatic repulsion of the eight ionized acetic and propionic acid substituents at the β-carbon positions of the pyrrole rings. However, the uroporphyrins dimerize at low pH or upon addition of salt (> 1 M) because of shielding of the charges on the carboxylate groups. The Soret absorption band of the aggregates exhibits marked broadening and a blue shift of 10-15 nm (depending on the metal derivative) with respect to the Soret of the monomers. The α and β bands are also broadened but shift by a lesser extent to the red. In particular, the π–π aggregation of NiUroP (for both planar and nonplanar conformers), gives 1-5 cm^{-1} shifts to higher frequency in the structure-sensitive Raman lines.[12-15] Like

uroporphyrin, OAATPP contains eight ionizable acetic acid groups at the β-positions of the pyrrole rings, and might be expected to show similar aggregation behavior. However, as a result of the nonplanar distortion and resulting steric constraints on intermolecular interactions, π–π aggregates were not formed either at low pH or at high ionic strength.

Electronic effects may also play a role in determining the functionality of OAATPP and related nonplanar properties. For instance, acetic acid and acetic acid ester groups are more electron-withdrawing than alkyl, hydroxyethyl and acetate substituents and the nitrophenyl meso substituent is more electron-withdrawing than the unsubstituted phenyl group. Thus, distinct chemical properties are also expected for these nickel porphyrins and both electronic and conformational effects must be considered when correlating differences in spectral and chemical properties.

3.1. Materials and Methods

Preparation of Ni3: Pyrrole-3,4-diacetic acid dimethylester **1** was synthesized according to Chiusoli *et al.*[18] and then treated with benzaldehyde under Lindsey's cyclization conditions[19] using $BF_3 \cdot Et_2O$ as catalyst and dichlorodicyanobenzoquinone as oxidant to yield the porphyrin dication H_4OAATPP-OME, **$H_4$3** (**Figure 3.1**). (UV-visible (CH_2Cl_2) λ_{max} nm: 473, 701). Without further purification the evaporated residue was treated with $Ni(OAc)_2/CHCl_3$ at room temperature and the resultant NiOAATPP-OME, **Ni3**, was purified by preparative TLC (Analtech, Inc.) on silica with 5% acetone/CH_2Cl_2. Recrystallization in CH_2Cl_2/petroleum ether afforded **Ni3** in 12.5% yield from **1**. ^{1}H-NMR ($CDCl_3$): δ ppm 7.92-7.95 (m, 8H, o-ArH); 7.59-7.68 (m, 12H, m-, p-ArH); 3.33 (s, 24H, OCH_3); 3.25 (s, 16H, CH_2). ^{13}C-NMR (CD_3OD): (172.4, 145.7, 139.8, 138.9, 129.9, 129.0, 118.9, 52.0, 33.2). IR ($CHCl_3$): 1738 cm^{-1} (C=O),

UV-visible (CH_2Cl_2) λ_{max} nm (ε x 10^{-3}): 436 (231), 555 (16.2), 586 (8.1). Anal. Calcd. for $C_{68}H_{60}N_4O_{16}Ni \cdot H_2O$: C, 63.81; H, 5.04; N, 4.38. Found C, 63.81; H, 5.09; N, 4.30.

Preparation of Ni4: The octacarboxylate NiOAATPP was synthesized by saponification of the ester groups in **Ni3** using KOH/MeOH at reflux overnight. The evaporated residue was purified by ion exchange chromatography (Dowex 50X8-100 resin, H form; 1:1 MeOH:H_2O eluent) ^{1}H-NMR (d^6-acetone): 7.91-7.94 (m, 8H, o-ArH); 7.72-7.75 (m, 4H, p-ArH); 7.63-7.68 (m, 8H, m-ArH); 3.30 (s, 16H, CH_2), UV-visible (.1M KOH) λ_{max} nm: 432, 548, 582.

Preparation of Ni5: Porphyrin **Ni3** was treated with $LiAlH_4$ in THF[20] to yield NiOHETPP after purification with preparative TLC (5% MeOH/CH_2Cl_2). ^{1}H-NMR (CD_3OD): 7.98-8.01 (m, 8H, o-ArH); 7.70-7.73 (m, 12H, m,p-ArH); 3.03, 2.74-2.88, 2.12-2.27 (32H, CH_2CH_2). ^{13}C-NMR (CD_3OD): (147.4, 142.9, 139.7, 135.4, 130.2, 129.0, 119.0, 64.2). UV-visible (CH_2Cl_2) λ_{max} nm (ε x 10^{-3}): 436 (113), 555 (8.8), 590 (6.4). FAB MS (m/e): 1023 ($M^+ + H$).

Preparation of Ni6: The *p*-nitrophenyl analog was synthesized as was **Ni3** except that p-nitrobenzaldehyde was used for the cyclization. ^{1}H-NMR ($CDCl_3$): 8.52, 8.17 (AB quartet, 16H, ArH, J= 8.8 Hz); 3.39 (s, 24H, OCH_3); 3.22 (s, 16H, CH_2); UV-visible (CH_2Cl_2) λ_{max} nm (ε x 10^{-3}): 450 (143), 560 (14.4), 600 (8.8). Anal. Calcd. for $C_{68}H_{56}N_8O_{24}Ni$: C, 57.20; H, 3.95; N, 7.85. Found C, 57.29, H, 4.19, N, 7.46.

All of the above mentioned metalloporphyrins were synthesized at the Brookhaven National Laboratory, Upton, NY. Chemicals and solvents (packaged in Sure/Seal bottles for moisture-sensitive reactions) were purchased from Aldrich Chemical and used without further

purification. Ligand-binding and aggregation studies were carried out according to published procedures.[12,14]

Spectroscopic Methods: ^{1}H and ^{13}C NMR were run on a Bruker AM-300 spectrometer (Brookhaven National Laboratory, Upton, NY). Mass spectra were recorded on a Kratos MS 890 instrument equipped with a Sattlefield FAB gun using a nitrobenzyl alcohol matrix (Brookhaven National Laboratory, Upton, NY). Elemental analyses were carried out by Galbraith Laboratories, Inc. (Knoxville, TN). EXAFS studies are also performed at Brookhaven National Laboratory, NY. UV-visible spectra were obtained with a Hewlett Packard HP 8452A diode array spectrophotometer.

Resonance Raman spectra were obtained at room temperature using a dual-channel Raman spectrometer described earlier.[21] Peak positions for the Raman lines were determined from the fast-Fourier-transform smoothed spectra and corrected relative to the Raman lines of nickel octaethylporphyrin in methylene chloride.[22] Approximately 60 mW of either the 406.7-nm or the 413.1-nm laser excitation from a krypton ion laser (Coherent) was used to irradiate the samples contained in a dual-compartment rotating cell. The scattered light from the two samples was collected at 90^{o} to the direction of propagation and polarization of the exciting laser light. The scattered light was analyzed (SPEX 1401 double monochromator), detected by a cooled (-20 ^{o}C) Hamamatsu R928P photomultiplier tube, and the signal from the two samples separated electronically. Rotation of the sample cell at 50 Hz enabled the samples to be probed alternately and also prevented local heating of the samples. Each of the Raman spectra is the sum of 5-10 scans. Spectral resolution was 4 cm^{-1}. Sample integrity was checked periodically during the Raman experiment by examining individual scans. Also, UV-visible absorption spectra were

obtained before and after the Raman experiments. The individual Raman bands were subsequently decomposed using Lorentzian line shapes and a least-squares fitting procedure with a sloped, linear baseline to extract the positions, heights, and line widths of those bands.

3.2. Results and Discussion

The nickel derivatives of porphyrins **3**, **4**, **5**, and **6** have been characterized by NMR, UV-visible absorption, and resonance Raman spectroscopy and other methods. As the porphyrin macrocycle deviates from planarity as a result of increasing the steric crowding of the peripheral groups, the aromatic character decreases and results in NMR upfield shifts in the proton resonances from diminished ring current effects.[23] For **Ni3**, **Ni4**, **Ni5**, and **Ni6**, upfield shifts are noted for the phenyl and the β-methylene protons relative to more planar Ni porphyrins like uroporphyrin (UroP), tetraphenylporphyrin (TPP), and OEP. For example, the β-methylene protons of the acetic acid groups exhibit the largest upfield shift of 1.9 ppm; 5.0 ppm in NiUroP and 3.1 ppm in **Ni4** (each in 0.1 M $NaOH/D_2O$). A similar shift of 1.8 ppm is observed for the methylene protons in NiOEP and NiOETPP, which are 4.1 and 2.3 ppm (at coalescence) respectively.[2,23]

Recent NMR results for OETPPs have shown that the highly nonplanar macrocycle in solution undergoes a dynamic process of macrocycle inversion (the interconversion between nonplanar conformations).[2,3] This interconversion was monitored by following the temperature dependence of the β-methylene proton resonances. The methylene protons of **Ni3** show a slightly broad singlet at 293 K, indicating fast interconversion. This singlet broadens further and finally appears as an AB doublet upon cooling, indicating inequivalency of the protons. The coupling constant (J_{AB}= 17 Hz), is typical for geminal protons and indicates slow inversion of the saddle

conformation on the NMR time scale. The coalescence temperature for the methylene protons of **Ni2** is 293 K, whereas for **Ni3** and **Ni6**, it is 245 and 265 K, respectively. The corresponding free energy of activation, ΔG^* for **Ni2** and **Ni3** is 13.2 and 12.0 kcal mol^{-1}, respectively. The high barrier for NiOETPP could be explained if NiOETPP is more nonplanar than NiOAATPP-OME and NiOAATNPP-OME.

The conformation of the macrocyle can also be monitored by its optical absorption spectrum. The Soret and the Q absorption bands are red-shifted in nonplanar porphyrins when compared with planar porphyrins.[2,3] The UV-visible absorption spectra of NiTPP, NiOHETPP (**Ni5**), NiOAATPP (**Ni4**), NiOAATPP-OME (**Ni3**) and NiOAATNPP-OME (**Ni6**) in non-coordinating solvents are shown in **Figure 3.2**. 19-36-nm red shifts were observed for porphyrins **Ni3**-**Ni6** with respect to NiTPP, a planar porphyrin. Wavelengths of the absorption bands (λ_{max}) for this series of nickel porphyrins are listed in **Table 3.1**. The red shifts observed for the NiOAATPPs are comparable to those observed for porphyrins like NiOETPP that are known from the X-ray crystal structure to be highly nonplanar.[24] For the six-coordinate complexes (**Ni3** and **Ni6**) that are formed, a red shift with respect to six-coordinate NiTPP is also observed (**Figure 3.3**). The absorption spectrum of the 1-MeIm complex of **Ni6** looks like the spectrum of the dication ($\mathbf{H_46}$). However, demetallation has not occurred because evaporation of the coordinating solvent follow by dissolution in noncoordinating solvents gives the normal four-coordinate absorption spectrum. (Apparently, the nitro groups of NiOAATNPP-OME are electronically coupled to the macrocycle π–π transitions since the Soret band in methylene chloride is observed to be red-shifted by an additional 12 nm compared to that of OAATPP-

OME. Also for the six-coordinate **Ni6**, a very large red shift relative to other six-coordinate Ni porphyrins is observed.)

EXAFS studies directly confirm that **Ni3** has a highly nonplanar conformation. In particular, solution EXAFS results[25] for **Ni3** reveal short Ni-N distances of 1.92 (0.02) Å, which are comparable to those found in **Ni2** (1.906 (2) Å) for which the crystal structure shows a saddle-shaped conformation.[24] No planar nickel porphyrins have such short Ni-N distances.

Resonance Raman spectra for the nickel complexes of OAATPP, OAATPP-OME, OAATNPP-OME and OHETPP are shown in **Figure 3.4**, and the frequencies of some structure-sensitive porphyrin modes and a phenyl mode are listed in **Table 3.2**. An additional spectral feature is observed for the nitrophenyl derivative; the Raman line at 1345 cm^{-1} in spectrum C of **Figure 3.4** is probably the symmetric stretch of the nitro groups at the para positions of the meso-substituted phenyl groups.[8,26] The 1345-cm^{-1} Raman line of OAATNPP-OME is more enhanced with respect to ν_4 for laser excitation at 458 nm near the Soret than at 413 nm, possibly suggesting that porphyrin-NO_2 charge-transfer transitions are coupled to the π–π^* transitions.

Generally, the structure-sensitive Raman marker lines show large downshifts when compared to a planar nickel porphyrin, and the downshifts are a result of the nonplanar distortion of the macrocycles.[2,3] The relative sizes of the downshifts within a series of porphyrins can generally be used as a measure of the degree of macrocyclic distortion.[8,27,28] In particular, ν_4, ν_3, and ν_2 all downshift by 15 to 43 cm^{-1} for the distorted octaethyl- and octapropyl-tetraphenylporphyrins relative to planar NiOEP.[29,30] For the series of NiOAATPP derivatives

Table 3.1. Wavelength of absorption maxima (in nm) of nickel(II) porphyrins in various coordinating and non-coordinating solvents.

	water			CH_2Cl_2			1-methylimidazole			piperidine		
Porphyrins	γ	β	α	γ	β	α	γ	β	α	γ	β	α
NiUroP												
(4-coord.)	394	518	552									
+ NaCl	388	518	554									
NiOEP												
(4-coord.)	not soluble			391	517	551	392	514	550	396		552
(6-coord.)							418			419	542	574
NiTPP												
(4-coord.)	not soluble			414	527		418			414	519	
(6-coord.)							436	565	609	433	561	600
NiOETPP (**Ni2**)												
(4-coord.)	not soluble			433	552	586	434	552	588	435	553	590
NiOHETPP (**Ni5**)												
(4-coord.)	not soluble			434*	555*	588*	436	553	586	438	554	592
NiOAATPP (**Ni4**)												
(4-coord..)	431	549	587	435*	552*	589*	439	553	588	440	556	589
+ NaCl	431	550	587									
NiOAATPP-OME (**Ni3**)												
(4-coord.)	not soluble			438	554	584	438	554	584	440		
(6-coord.)							458			464		693
NiOAATNPP-OME (**Ni6**)												
(4-coord.)	not soluble			450	561	597						
(6-coord.)							476		704	489		717

*Spectra obtained in acetone. In CH_2Cl_2 and acetone, most Ni(II) porphyrins listed here give similar absorption spectra.

Table 3.2. Resonance Raman frequencies (cm^{-1}) of structure sensitive marker lines for Ni(II) porphyrins in non-coordinating solvents and under various aqueous conditions.

Nickel Porphyrin/ Solvent	ν_4	ν_3	ν_2	ν_ϕ
OEP /CH_2Cl_2	1383	1519	1600	----
TPP /CH_2Cl_2	1374	1470[a]	1572	1600
OETPP (**Ni2**) /CH_2Cl_2	1360	1504	1562	1597
OHETPP (**Ni5**) /acetone	1359	1504	1565	1598
OAATPP-OME (**Ni3**) /CH_2Cl_2	1368	1509	1574	1596
OAATNPP-OME (**Ni6**) /CH_2Cl_2	1370	1508	1576	1592
OAATPP (**Ni4**) /acetone[b]	1369	1509	1573	1597
H_2O/pH 3[b]	1370	1511	1577	1596
H_2O/pH 7[b]	1368	1510	1569	1599
H_2O/pH 13[b]	1367	1509	1568	1598
H_2O/pH 13/NaCl[b]	1367	1509	1567	1598

[a]The potential energy distribution of this mode is radically altered for TPP as compared to OEP and OETPP. [b]$\Sigma\sigma_m$ values are estimated to be between 0.00 and -0.32 depending on the degree of ionization of the eight acid substituents.

investigated here, these lines downshift by 8 to 35 cm^{-1} relative to NiOEP, and, therefore, must be nearly as highly distorted as NiOETPP. However, the NiOAATPP derivatives vary considerably in the electron-withdrawing properties of the substituents, and thus an electronic effect on the Raman frequencies is also possible.

To accurately interpret the frequency differences within this group of NiOAATPPs, it is important first to compare only porphyrins with similar electronic properties to determine the effect of structural differences. The acetate and the hydroxyethyl moieties of **Ni4** and **Ni5** have electronic properties that are the same as the ethyls of **Ni2**, but are sterically larger than the ethyls. These more bulky substituents would be expected to sterically induce larger distortions from planarity than observed for **Ni2**. However, neither **Ni4** nor **Ni5** show significantly lower frequencies than **Ni2**; in fact, **Ni4** shows significantly higher marker line frequencies than **Ni2** and **Ni5**, indicating *decreased* nonplanarity for **Ni4**. For NiOETPP and NiOHETPP, the nearly identical Raman frequencies can be attributed to similarities in the both the steric and electronic properties of these substituents.

The interpretation of the frequency differences in the structure-sensitive Raman lines for the *entire* series of NiOAATPPs solely in terms of differences in the degree of nonplanarity is not possible because of the conflicting dependence on the electronic effects of the peripheral substituents. A dependence of the position of the absorption bands on electron-withdrawing properties of the substituents is already known.[29] **Table 3.3** lists the sum of the Hammett constants[30] ($\Sigma\sigma_m$) for the substituents on each porphyrin of the series and these values can be used to estimate this electronic effect. In some cases, almost identical conformations are expected on the basis of the peripheral crowding, so that the electronic effect is clearly evident. For

Table 3.3. Sum of Hammett sigma values, $\Sigma\sigma_m$, of different nickel porphyrins and their relative binding to 1-methylimidazole at room temperature.

Nickel Porphyrin		$\Sigma\sigma_m$	% bound
OEP		- 0.56	5
OETPP	**Ni2**	- 0.32	0
OHETPP	**Ni5**	- 0.32	0
OAATPP (deprotonated)*	**Ni4**	- 0.32	0
OAATPP-OME	**Ni3**	0.00	25
TPP		0.24	70
OAATNPP-OME	**Ni6**	0.68	100

*$\Sigma\sigma_m$ values are estimated to be between 0.00 and -0.32 depending on the degree of ionization of the eight acid substituents.

example, NiOAATPP-OME and NiOAATNPP-OME should exhibit almost identical conformations because the *p*-NO_2 groups on the phenyls do not significantly increase the steric crowding. Thus, the 2-cm^{-1} differences in frequency noted for ν_4 and ν_2 are most likely a result of the larger electron-withdrawing effect of the nitrophenyl groups compared to the phenyls. In fact, the frequencies of ν_4 and ν_2 for the entire series of NiOAATPP derivatives show fair correlations with $\Sigma\sigma_m$ as illustrated in **Figure 3.5**. NiOETPP and NiOHETPP clearly exhibit unusually low frequencies relative to this linear relationship because of structural effects and for this reason were not included in the linear regressions. The frequency dependence of the remaining points is mostly electronic since the linear relationship with $\Sigma\sigma_m$ accounts for most of their frequency variation.

Similar dependence of ν_4 and ν_2 on the electron-withdrawing capacity of substituents has been observed for other conformationally homologous series of porphyrins, including a series of fluorinated dodecaphenylporphyrins ($DPPF_x$, x = 0, 20, 28, and 36).[31] In both the Fe(III)- and Ni(II)$DPPF_x$ series, ν_4 and ν_2 (but not ν_3) increase in proportion to the number of fluorines and to $\Sigma\sigma_m$. Further, molecular mechanics calculations indicate no structural differences among the Ni$DPPF_x$ series., indicating that the changes are entirely a result of the electron-withdrawing effect of the fluorines. The increases in Raman frequency with unit increase in $\Sigma\sigma_m$ for the NiOAATPP series reported here (slopes given in **Figure 3.5**) are about the same as for the $DPPF_x$ series, supporting the assertion that the electronic effect is the largest contributor for the NiOAATPP series.

In summary, while the shifts observed for the octaacidporphyrins are, in part, due to the electron-withdrawing/donating effect of the substituents, variations resulting from structural

changes are also evident. Structural differences are evident in the differences in frequency that occur for porphyrins with similar electronic properties as described above. From **Figure 3.5**, the data further suggests that the higher frequencies of ν_4, ν_3, and ν_2 for most of the porphyrins (**Ni4**, **Ni3** and probably **Ni6**) relative to **Ni2** and **Ni5** result in part from the more nonplanar conformation of the latter porphyrins. In addition, a more planar conformation for both **Ni3** and **Ni6** also accounts for their lower barriers to inversion (compared to **Ni2**) given by the NMR measurements.

One can ask whether the electron-withdrawing effect of the substituents actually causes a conformational change and whether it is this non-steric structural change that is measured by the shifts in the Raman lines. One possible answer to these questions is that the pyrrole rings become poorer σ-charge donors with decreasing electron-donating abilities of the substituents, and, as a result, the pyrrole nitrogen-nickel bond length increases, causing the macrocycle to become more planar. The increased planarity raises the marker line frequencies. Additional structural studies will be required to test this hypothesis.

The affinity for axial coordination of nitrogenous ligands is also thought to be effected by both electron-withdrawing substituents and nonplanarity of the macrocycle.[3a,24] Planar porphyrins such as NiOEP and NiTPP bind readily to nitrogenous ligands, whereas nonplanar NiOETPP does not and remains four-coordinate even though electronically NiOETPP ($\Sigma\sigma_m$ = -0.32) lies between NiOEP (-0.56) and NiTPP (0.24). In addition, the NiOAATPP-series of nonplanar porphyrins shows increased ligand affinity with an increase in electron-withdrawing capacity of the peripheral groups. **Table 3.3** shows a direct correlation between the overall electron-withdrawing capacity for different porphyrins and their relative binding of 1-methylimidazole (1-MeIm) in the neat

solvent. Similar trends in ligand affinity are also observed for pyridine and piperidine. The reason for this trend is that porphyrin dianion ligand does not fully neutralize the +2 charge on the Ni(II) ion, leaving Ni partially positively charged. The electron deficiency is primarily in its σ orbitals. Consequently, exogenous σ-donating ligands will generally bind axially via the empty $d_{z}2$ orbital. Electron-withdrawing peripheral substituents enhance the electron deficiency of the metal, leaving the nickel ion less coordinatively saturated and increasing the axial ligand affinity. The failure of NiOAATPP to bind 1-MeIm may be due to deprotonation of the acid groups in this solvent, which makes the acid groups more electron donating (the pK_a values for imidazole and the acetic acid groups are 7.0[32] and 6.5,[12] respectively).

The aggregation behavior of NiOAATPP in aqueous environments were also examined and compared it with that of planar NiUroP (see **Table 3.2** and **Figures 3.6** and **3.7**). NiUroP shows no evidence of aggregation in basic solutions, but upon addition of salt (>1 M) or acid (pH<6), π–π aggregates are formed.[12] Aggregation is caused by shielding of the -8 charge of the deprotonated acid groups and results in a large blue shift in the Soret absorption band (see **Figures 3.6A and 3.6B**). In addition, 1-5 cm^{-1} upshifts in the frequencies of the structure-sensitive Raman lines are observed upon salt-induced π–π dimerization of NiUroP.[12,14] In contrast with NiUroP, the UV-visible spectra of NiOAATPP show no evidence of aggregation under similar solution conditions (see **Figures 3.6C and 3.6D**). Further, the resonance Raman spectra for NiOAATPP (**Figure 3.7**) at different pH values and after adding NaCl at high pH show no evidence for aggregation. Similarly, no appreciable changes are observed upon addition of salt (**Figure 3.7C**). With an increase in pH (**Figure 3.7B**), structure-sensitive Raman lines shift

to lower frequencies due to the decreased electron-withdrawing capacity of the deprotonated acetic acid groups, but show no indication of aggregation.

3.3. Conclusions

The evidence from the NMR, EXAFS, optical and resonance Raman spectroscopies indicate that OAATPP and its derivatives have highly nonplanar conformations. While the Ni-N distance and the diminished ring current effects both indicate that the NiOAATPP-OME is nonplanar, the free energy of activation for macrocycle inversion and the resonance Raman frequencies suggest that NiOAATPP derivatives are probably more planar than NiOETPP. The structure-sensitive Raman lines and the optical absorption spectra are found to vary depending on the degree of porphyrin nonplanarity and also the electronic effects of the substituents.

The ligand binding affinity is dependent on both the macrocycle conformation and the electronic effects. Among the dodeca-substituted nonplanar porphyrins, ligand binding affinity appears to be directly correlated to electron-withdrawing ability as estimated from the Hammett σ_m constants of the peripheral substituents.

The nonplanar conformation of OAATPP prevents the known π–π aggregation of planar octaacidporphyrins like UroP. The spectra of NiOAATPP show no evidence of aggregation upon addition of salt (>1M) or acid (pH <6), unlike the more planar NiUroP which forms π–π aggregates under similar solution conditions. In an effort to exploit the unique aggregation properties of the OAATPP derivatives, a lipoporphyrin has been synthesized recently with a NiOAATPP-OME polar head group and long alkane tails. Using this new lipoporphyrin mixed Langmuir-Blodgett films of the lipoporphyrin were constructed with stearic acid. These films show no evidence of aggregation of the porphyrin macrocycles or of phase separation from the

stearic acid component that is typical of planar lipoporphyrins.[33] However, the water soluble tin analog of OAATPP is yet to be synthesized for its use as photocatalytic testing in solar detoxification.

3.4. Figures

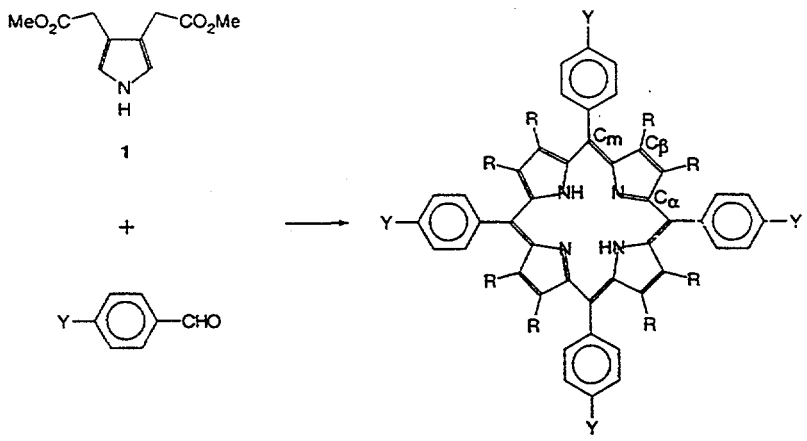

2, Y = H,	R = CH_2CH_3	OETPP
3, Y = H,	R = $CH_2CO_2CH_3$	OAATPP-OME
4, Y = H,	R = CH_2CO_2H	OAATPP
5, Y = H,	R = CH_2CH_2OH	OHETPP
6, Y = NO_2	R = $CH_2CO_2CH_3$	OAATNPP-OME

Figure 3-1. Structures of pyrrole-3,4-diacetic acid dimethylester (**1**) and various planar and nonplanar nickel porphyrins: OETPP (**2**), OAATPP-OME, (**3**), OAATPP (**4**), OHETPP, (**5**), and OAATNP-OME (**6**).

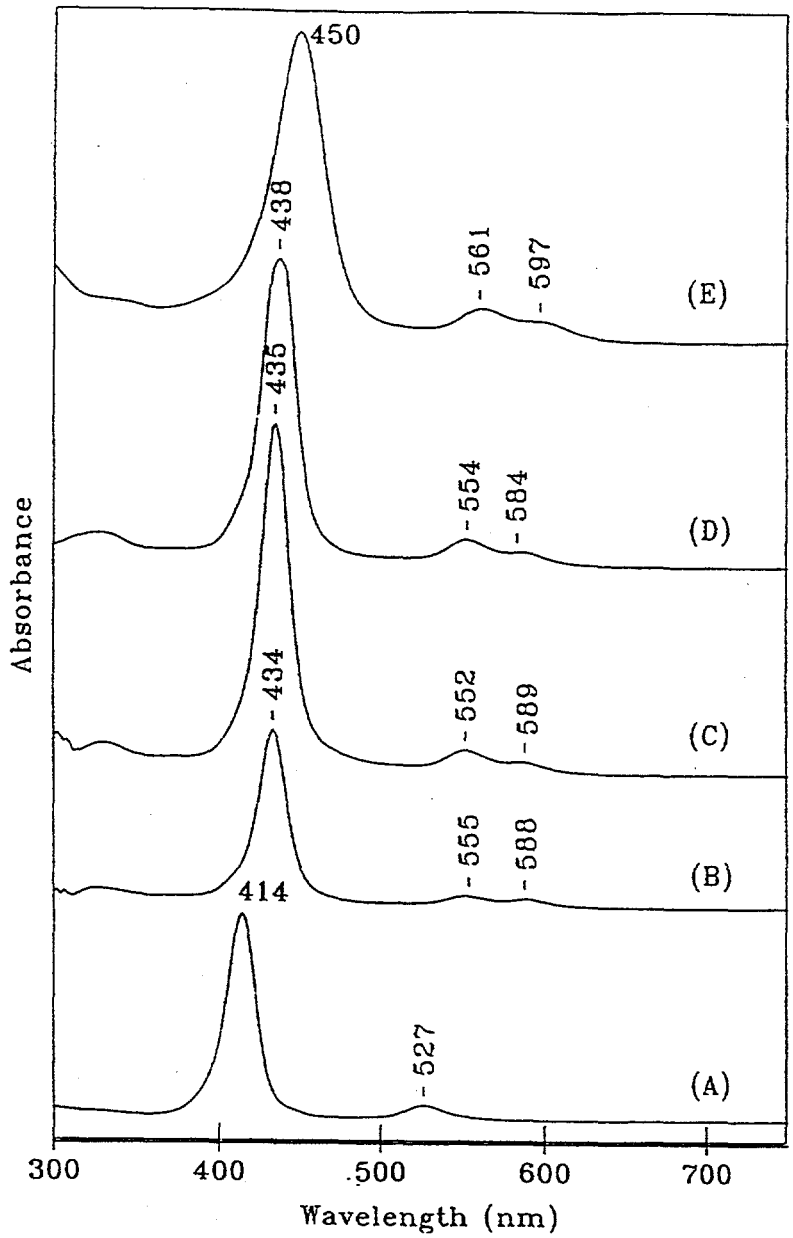

Figure 3-2. UV-visible absorption spectra of four-coordinate (A) NiTPP, (B) NiOHETPP (**Ni5**), (C) NiOAATPP (**Ni4**), (D) NiOAATPP-OME (**Ni3**), and (E) NiOAATNPP-OME (**Ni6**). Spectra were obtained in either neat methylene chloride or acetone.

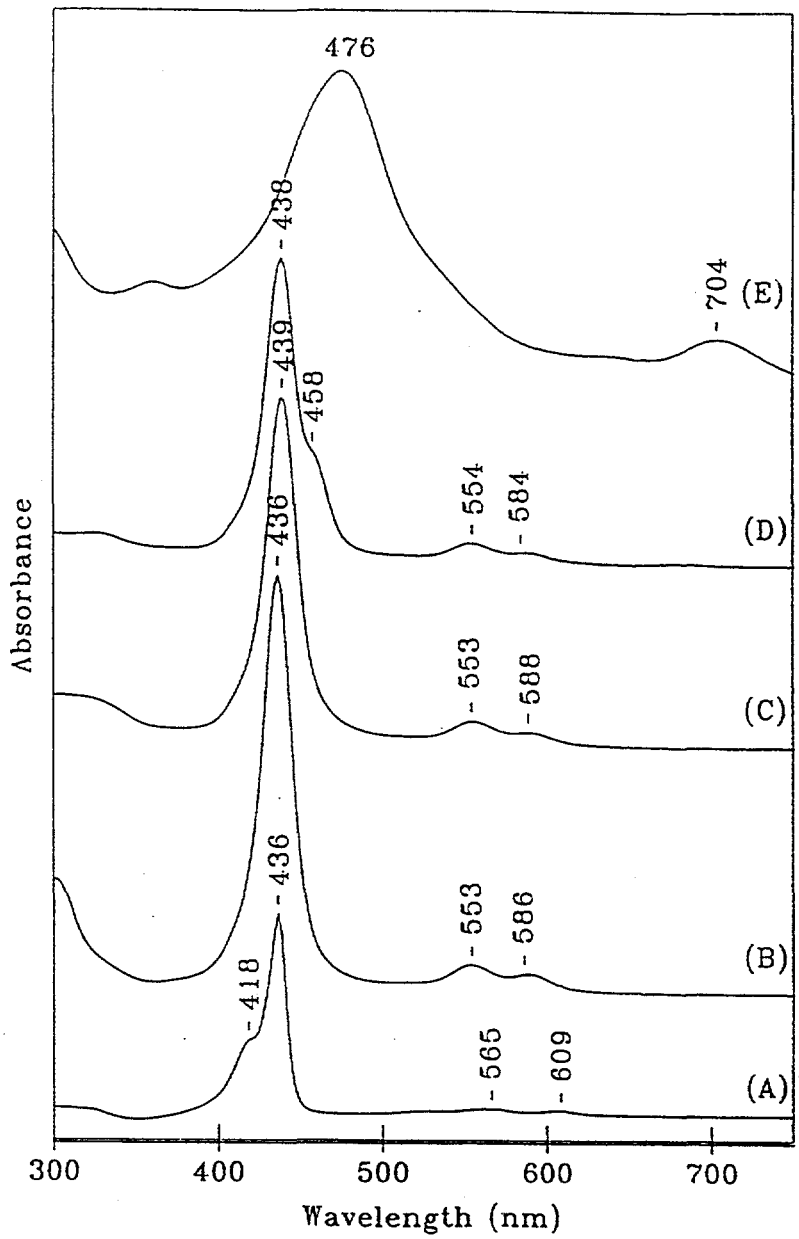

Figure 3-3. UV-visible absorption spectra of (A) NiTPP, (B) NiOHETPP (**Ni5**), (C) NiOAATPP (**Ni4**), (D) NiOAATPP-OME (**Ni3**), and (E) NiOAATNPP-OME (**Ni6**) in a coordinating solvent. All spectra were obtained in 1-methylimidazole.

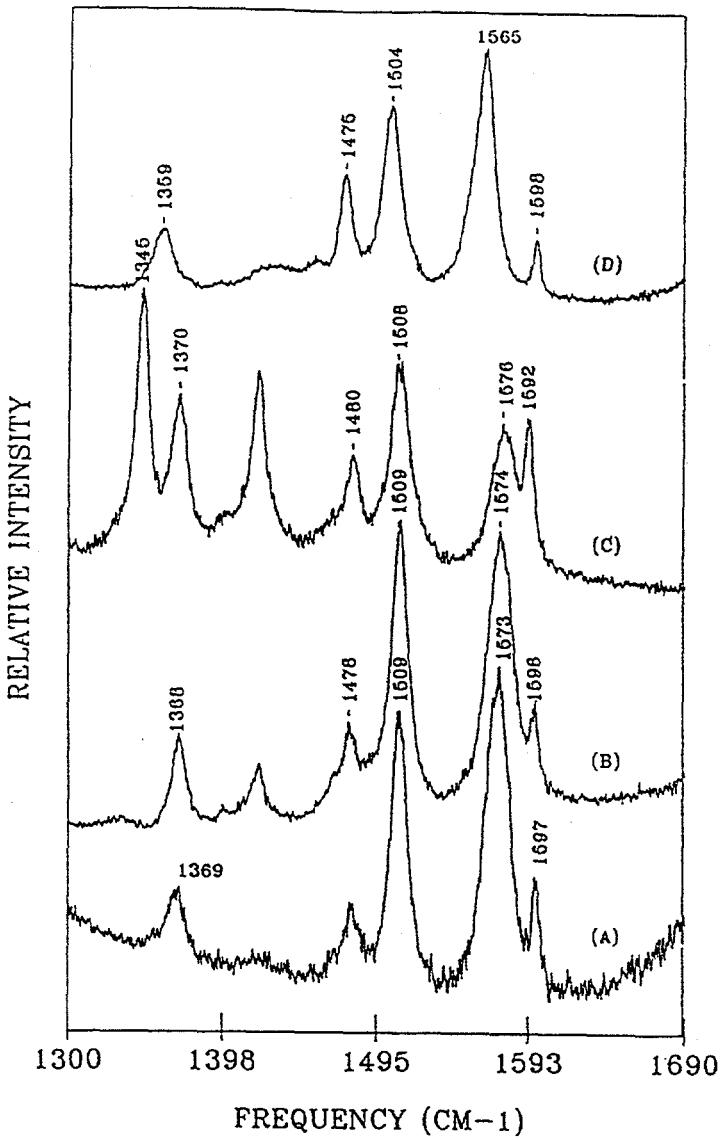

Figure 3-4. Resonance Raman spectra of (A) NiOAATPP, (B) NiOAATPP-OME, (C) NiOAATNPP-OME and (D) NiOHETPP. Solvent for porphyrin solution was either methylene chloride or acetone and a 413.1-nm laser excitation was used for obtaining Raman spectra.

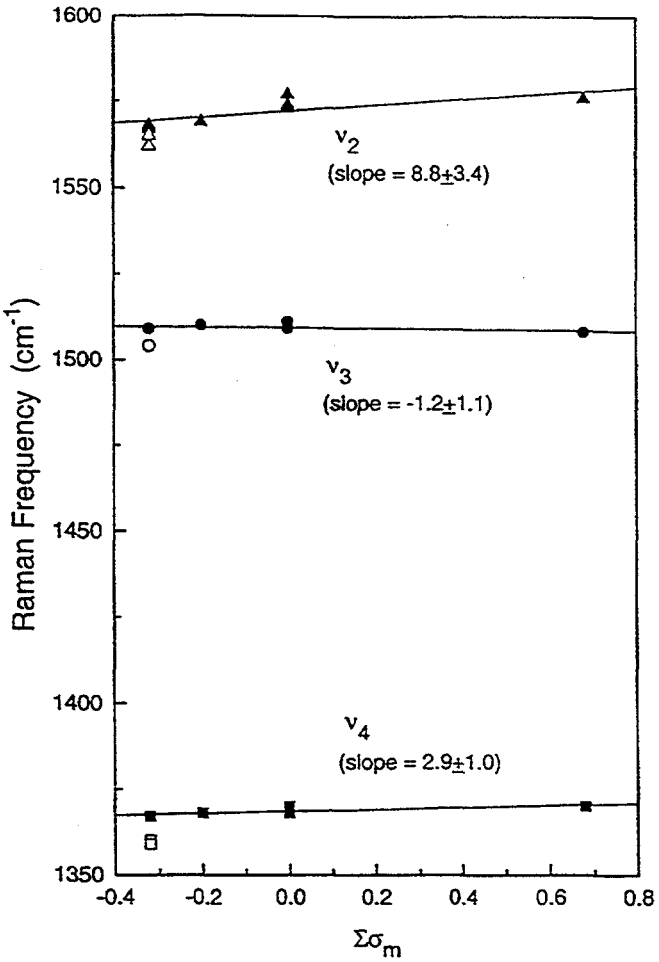

Figure 3-5. Linear relationships between the frequencies of the Raman lines ν_4, ν_3 and ν_2 for the nickel porphyrins listed in **Table 3-2** and the electron-withdrawing properties of the peripheral substituents as measured by $\Sigma\sigma_m$ given in **Table 3-3**. Nickel octaacid-tetraphenylporphyrins (solid symbols); NiOETPP and NiOHETPP (open symbols) Slopes of the lines and standard deviations are given in parenthesis. The slopes are, within error, the same as for the $FeDPPF_x$ series, except for ν_4 which has a significantly smaller slope for the nickel octaacid-tetraphenylporphyrins.

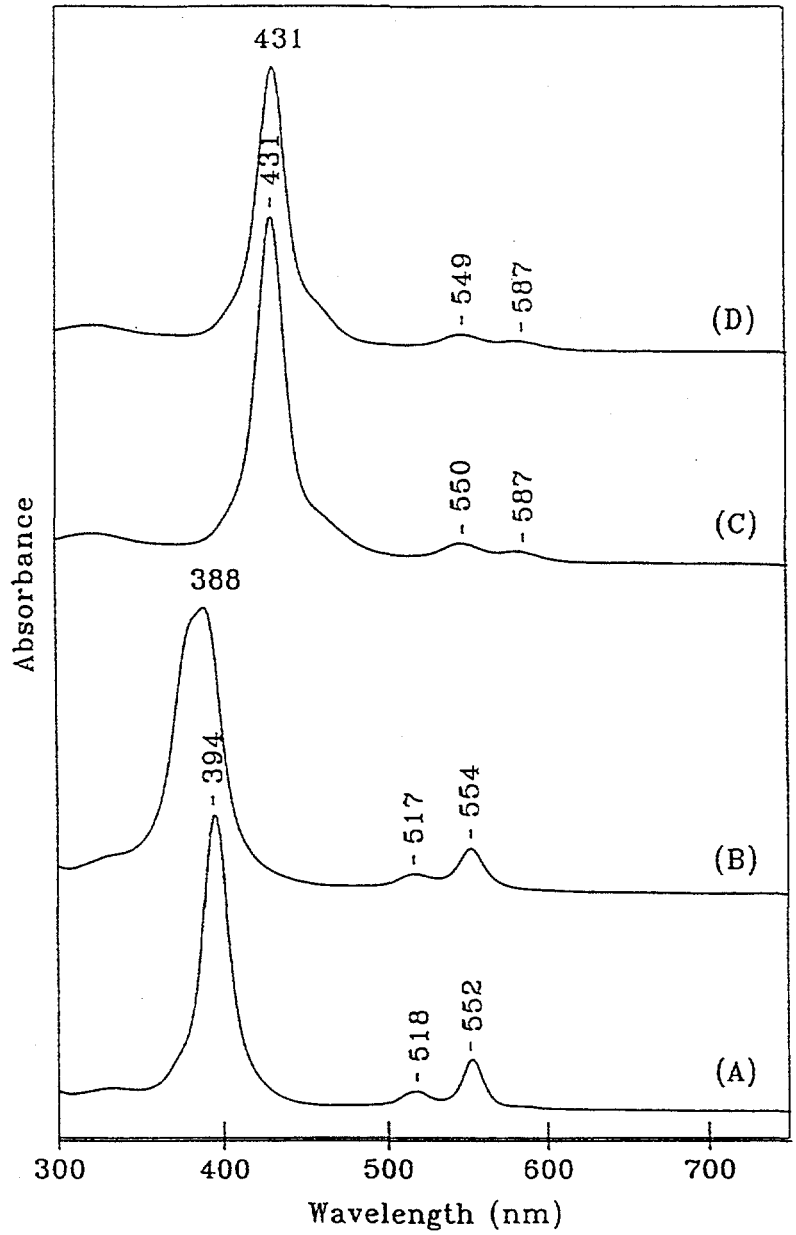

Figure 3-6. UV-visible absorption spectra of (A) NiUroP, (B) NiUroP plus 4.5 M NaCl, (C) NiOAATPP, and (D) NiOAATPP plus 4.5 M NaCl at pH 13.

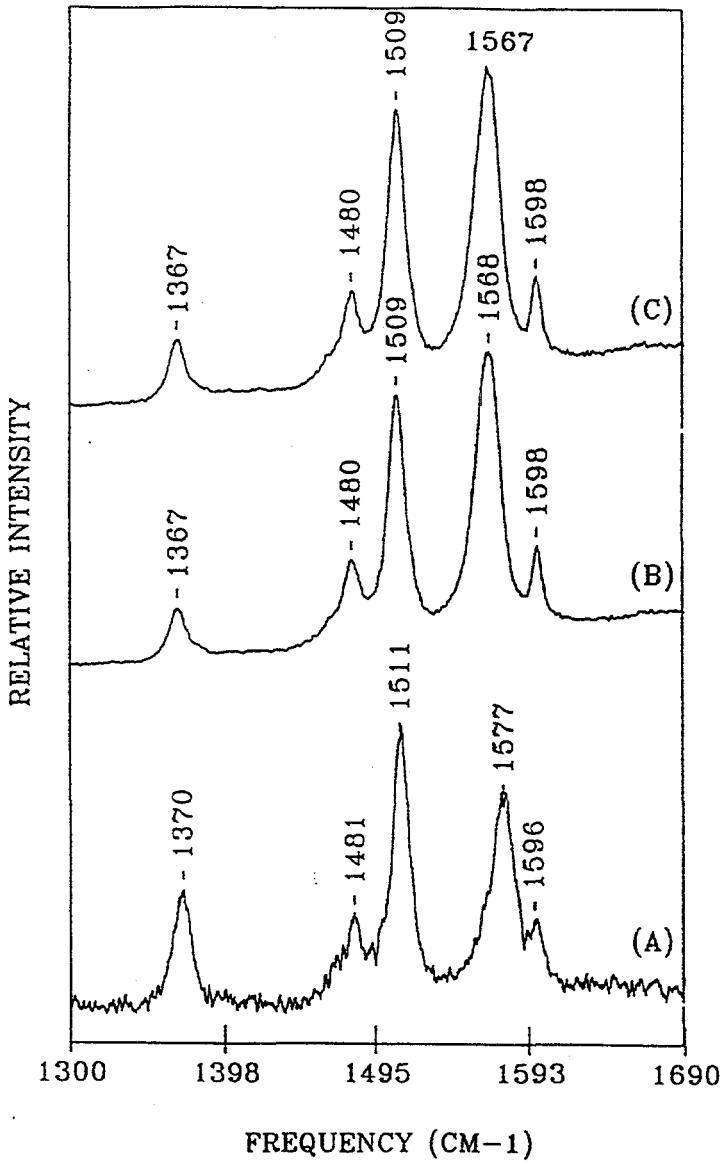

Figure 3-7. Resonance Raman spectra of aqueous solutions of NiOAATPP at (A) pH 3, (B) pH 13, and (C) pH 13 with added NaCl. A 413.1-nm laser line was used for obtaining Raman spectra.

3.5. References

1. Barkigia, K.M.; Berber, M.D.; Fajer, J.; Medforth, C.J.; Renner, M.W.; and Smith, K.M. *J. Am. Chem. Soc.* **1990**, *112*, 8851.

2. Sparks, L.D.; Medforth, C.J.; Park, M.-S.; Chamberlain, J.R.; Ondrias, M.R.; Senge, M.O.; Smith, K.M.; and Shelnutt, J.A. *J. Am. Chem. Soc.* **1993**, *115*, 581.

3. (a) Shelnutt, J.A.; Medforth, C.J.; Berber, M.D.; Barkigia, K.M.; and Smith, K.M. *J. Am. Chem. Soc.* **1991**, *113*, 4077. (b) Medforth, C.J.; Senge, M.O; Smith, K.M.; Sparks, L.D.; and Shelnutt,. J.A. *J. Am. Chem. Soc.* **1992**, *114*, 9859.

4. Scheidt, W.R.; Lee, Y.J. *Structure and Bonding* **1987**, *64*, 1.

5. Barkigia, K.M.; Chantranupong, L.; Smith, K.M.; and Fajer, J. *J. Am Chem. Soc.* **1988**, *110*, 7566.

6. (a) Kratky, C.; Waditschatka, R.; Angst, C.; Johansen, J.; Plaquerent, J.C.; Schreiber, J.; and Eschenmoser, A. *Helv. Chem. Acta* **1982**, *68*, 1312. (b) Waditschatka, R.; Kratky, C.; Juan, B.; Heinzer, J.; and Eschenmoser, A. *J.Chem. Soc. Chem. Commun.* **1985**, 1604.

7. Geno, M. K.; Halpern, J. *J. Am.. Chem. Soc.* **1987**, *109*, 1238.

8. Hobbs, J. D.; Majumder, S. A.; Luo, L.; Sickelsmith, G.A.; Quirke, J. M. E.; Medforth, C. J.; Smith, K.M.; and Shelnutt, J. A. *J. Am. Chem. Soc.* **1994**, *116*, 3261.

9. Hoffmann, P.; Labat, G.; Robert, A.; and Meunier, B. *Tetrahedron Lett.* **1990**, *31*, 1991.

10. Hoffmann, P.; Robert, A.; and Meunier, B. *Bull. Soc. Chim. Fr.*, **1992**, *129*, 85.

11. Blumberg, W.E.; Peisach, J. *J. Biol. Chem.* **1965**, *240*, 860.

12. Shelnutt, J.A.; Dobry, M.M.; and Satterlee, J.D. *J. Phys. Chem.* **1984**, *88*, 4980.

13. Shelnutt, J.A. *J. Phys. Chem.* **1984**, *88*, 4988.

14. Shelnutt, J.A. *J. Phys. Chem.* **1984**, *88*, 6121.

15. Alden, R.G.; Ondrias, M.R.; and Shelnutt, J.A. *J. Am. Chem. Soc.* **1990**, *112*, 691.

16. Mauzerall, D. *Biochemistry* **1965**, *4*, 1801.

17. Shelnutt, J.A. *J. Am. Chem. Soc.* **1983**, *105*, 7179.

18. Chiusoli, G. P.; Costa, M.; and Reverberi, S. *Syn.* **1989**, 262.

19. Lindsey, J. S.; Schreiman, I. C.; Hsu, H. C.; Kearney, P. C.; and Marguerettaz, A. M. *J. Org. Chem.* **1987**, *52*, 827.

20. Smith, K. M.; Eivazi, F.; and Martynenko, Z. *J. Org. Chem.* **1981**, *46*, 2189.

21. Shelnutt, J.A. *J. Phys. Chem.* **1983**, *87*, 605.

22. Li, X.-Y.; Czernuszewicz, R. S.; Kincaid, J. R.; Stein, P.; and Spiro, T. G. *J.Phys. Chem.* **1990**, *94*, 47.

23. Janson, T. R.; Katz J. J. In *The Porphyrins*, Vol. IV, D. Dolphin, Ed., Academic Press, **1973**; pp 1-59.

24. Barkigia, K. M.; Renner, M. W.; Furenlid, L. R.; Medforth, C. J.; Smith, K. M.; and Fajer, J. *J. Am. Chem. Soc.* **1993**, *115*, 3627.

25. Miura, M.; Renner, M. W.; Furenlid, L. R.; Fajer, J.; and Shelnutt, J. A. *unpublished results.*

26. Anderson, K.K.; Hobbs, J.D.; Luo, L.; Stanley, K.D.; Quirke, M.E.; and Shelnutt, J.A. *J. Am Chem. Soc.* **1993**, 115, 12346.

27. Shelnutt, J. A.; Majumder, S. A.; Sparks, L. D.; Hobbs, J. D.; Medforth, C. J.; Senge, M. O.; Smith, K. M.; Miura, M.; Luo, L.; and Quirke, J. M. E. *J. Raman Spectrosc.* **1992**, *23*, 523.

28. Sparks, L. D.; Anderson, K. K.; Medforth, C. J.; Smith, K. M.; and Shelnutt, J. A. *Inorg. Chem.* **1993**, submitted.

29. Meot-Ner, M.; Adler, A. D. *J. Am. Chem. Soc.* **1975**, *97*, 5107.

30. Hausch, C.; Leo, A. *Substituent Constants for Correlation Analysis in Chemistry and Biology*; John Wiley & Sons, New York, **1979**.

31. Taylor, K. K.; Majumder, S. A.; Hobbs, J. D.; Sparks, L. D.; Medforth, C. J.; Forsyth, T. P.; Smith, K. M.; and Shelnutt, J. A., *unpublished results.*

32. "The Merck Index" 9th Edition, Merck & Co., Rahway; **1976**. 4811.

33. Song, X.; Miura, M.; Xu, X.; Taylor, K. K.; Majumder, S. A.; Hobbs, J. D.; Cesarano, J.; and Shelnutt, J. A., *Langmuir* **1996**, *12*, 2019.

Chapter 4

Development and Testing of TiO_2/SiC Photodiode System

4.0. Introduction

TiO_2 has a bandgap of 3.0 volt and is used as an efficient photocatalyst for some redox systems in aqueous environment. Different metals like Cr(VI), Hg(II), Ag(I), Au(III), Pt(IV) and Pd(II) are easily reduced and removed from solution by TiO_2 particles used as photocatalysts.[1-3] However, Ni(II) and Cd(II) cannot be treated with titania. Cu(II) can be treated, but its treatment is very sensitive to the particular redox environment that is used.[4] Prairie et. al.[1-2] demonstrated that reduction of metal ions on titania surface follows a Tafelian behavior[5] where the reduction rate depends exponentially on the difference between the conduction-band potential and the reaction potential as long as the later falls within the bandgap. It was argued that for the hard-to-reduce metal ions, in spite of the reaction potentials falling within the bandgap of TiO_2, slow photoreduction is observed because the difference between the conduction-band-electron potential and the reaction potential does not exceed the overpotential (*cal.* 0.5 V) that is required for the reaction to take place.

In the third year of this LDRD project, our approach was to modify the conduction band potential as well as the effective bandgap of a binary photocatalytic system to extend the set of metals to which photocatalysis can be applied. This involved combining TiO_2 and SiC to produce a photodiode with a conduction band at about -1.4 V (vs. NHE) while retaining the strong oxidizing potential of the valence band of TiO_2. According to this hypothesis, organic oxidation reactions will occur at the TiO_2 valence band and metal reductions at the SiC conduction band, with electrons flowing from the TiO_2 conduction band to the SiC valence band to close the circuit (see **Figure 1.8**). Thus, with two UV (~3.0 eV) photons, we achieve a photocatalyst with an

apparent bandgap of ~4.5 eV. Our ultimate goal was to form small binary particles that could be suspended in contaminated samples for water treatments.

Mills and coworkers have published a series of kinetic studies using CdS to reduce methyl orange.[6-8] In their investigations, the two-electron photoreduction of methyl orange (MO) to its colorless doubly-reduced form was monitored as a function of the concentration of the dye and the sacrificial electron donor Na_2EDTA. The electron donor reacts with photogenerated hole and goes through an irreversible oxidation process and, thus, termed as sacrificial agent. It was found that the kinetics of dye reduction fit a proposed reaction scheme assuming the formation of steady-state concentrations of photogenerated holes and electrons upon irradiation of the system. In this report, we extend the kinetics of MO photoreduction, sensitized by SiC, using the same sacrificial reductant. We have performed systematic kinetic photo-experiments on aqueous suspensions of SiC and TiO_2 powders using the reduction of methyl orange as a probe. The goal was to develop a simple method for evaluating the effectiveness of TiO_2, SiC and other photocatalytic systems.

Methyl orange is a typical azo dye, and its color and structure strongly depend on pH.[6-8] Only a few interconvertible structures of this dye make it a good spectroscopic probe for monitoring a rather simple photoredox process involved in a complex heterogeneous system. Two well characterized absorption peaks for oxidized and reduced peaks at 464 nm and 272 nm, respectively, with a single isosbestic point are reported in the literature.[6-8]

Since it is well known that titanium dioxide alone is capable of oxidizing many different organic compounds, but is limited in its ability to reduce metals, the silicon carbide counter electrode was added to the photoelectrochemical experiments to help in reducing some of the less

easily reducible metals (see above). As a first step, an electrochemical system was built using single-crystal electrodes. The electrodes were placed into a cell that could be illuminated or kept dark. Subsequently, measurements to find the illumination current, dark current, and the photocurrent (by difference) of the system in question were undertaken along with open circuit potential readings.

Some of the promising semiconducting properties of SiC are variable bandgaps, high thermal conductivity, high saturation drift velocity for electrons (~2 x 10^7 cm/s) and high breakdown field strength.[9,10] Although SiC has been examined extensively during the past decade with respect to its use for high temperature devices, only very few investigations of the photoelectrochemical properties have been published to date. One probable reason is the inferior quality of the SiC crystals that have been available.

Bandgaps of silicon carbide fall in the range from 2.2 to 3.2 eV depending on the crystal phases and modifications. The crystal packing of CSi_4 units can either form cubic (β-modification) zinc blend or hexagonal (α-modification) wurzite lattices. The bandgap of SiC is associated with the 'hexagonality' of the material.[11] The cubic lattice has the smallest bandgap, phases with more hexagonal structure exhibit higher bandgaps. It can be made in both p- and n-doped forms. SiC is almost as hard as diamond but much easier to synthesize. The raw materials carbon and silicon dioxide for the production of silicon carbide are available in virtually unlimited quantities. Furthermore, SiC is absolutely non-toxic due to its chemical inertness. Bockris et. al.[12] calculated the flat band potentials of SiC from linear Mott-Schottky curves: 1.4 V (pH 14) and 1.7 V (pH 0); the photocurrent density was very low (<9 $\mu A/cm^2$). A later report by Morisaki et. al.[13] showed strong irreversible changes in the flatband potential after illumination.

Conflicting theries about anodic corrosion[14-16] and current doubling[17] at SiC-electrodes are also present in the literature.

The results obtained with single crystal SiC in this work revealed limitations. The material was expensive and gave rise to poor photoelectrochemical efficiency. Such behavior may be due to the high doping level ($5x10^{18}$ to 10^{20} cm^{-3}) employed to lower the internal resistance of the crystal. The high doping level generates a very narrow space charge region where a field exists that can sweep electrons to the surface. Consequently, much of the photogenerated carriers may recombine prior to their reaction with species in solution although the narrow field strength may still be strong enough to pull the carriers apart. Hence, we chose to examine the theoretical effect of various properties of p-SiC on the basis of an earlier theory to understand the influence of various factors in each semiconductor.[18,19] Is SiC the best choice for being the partner of TiO_2? Theoretical modeling on electrode matching, kinetics and their photoefficiencies was used to address this question.

The model, developed under this LDRD project, accounts for the properties of the p-type and n-type semiconductors and the external parameters including light intensity and metal ion interaction with the semiconductors. Model calculations were carried out to establish energy requirements and to optimize relevant parameters for a binary photocatalytic system which consists of a combination of n-TiO_2 and either bare p-SiC or its platinized form. Model calculations were carried out for the reduction of few metal ions (e.g., Hg^{2+}, Cu^{2+}, Ag^{+}, Cd^{2+}, Ni^{2+}, and Pb^{2+}). Comparisons of cell current densities and cell efficiencies between calculated and experimental values were made for the TiO_2/SiC binary system.

4.1. Experimental

The photoresponses of powder and pellet forms of SiC were characterized in this project with an ultimate goal of combining the material with corresponding forms of TiO_2 for developing the proposed binary photocatalytic system. In the following sections, we will discuss the findings and limitations of the SiC photocatalyst.

4.1.0. Materials

4.1.0.0. Crystal Structures of TiO_2

As mentioned in **section 1.1**, there are three crystal phases of TiO_2: rutile, anatase, and brookhite. Electrochemical work, using TiO_2 single crystals, reported are exclusively with rutile. Single crystals of anatase are not large enough for performing the reported electrochemical experiments. However, polycrystalline TiO_2 electrodes can be anatase, rutile, or a mixture of both. Octahedral (TiO_6) structures of TiO_2 tetragonal unit cells are shown in **Figure 4.1.** Detail information on crystallographic parameters for both anatase[20] and rutile[21] are available in the literature.

The bond lengths for rutile and anatase are similar, but anatase exhibits a greater distortion in bond angles and, thus, contains a structure with lower density than that for rutile. Small ions can migrate through channels in both of these lattices and rapid migration of cations and anions affects the uniformity of doping and the density of recombination centers. The channels in rutile and anatase lie parallel and perpendicular, respectively, to the c axes of the crystal structures. The energetics of TiO_2 crystal structures and their bandgaps are described in **section 1.1.** Nevertheless, anatase can be converted to rutile at temperature higher than 500 °C.[22,23]

4.1.0.1. Crystal Structures of SiC

More than 180 modifications of SiC are known. As mentioned in the introductory **section 4.1**, there are two widely used polycrystalline structures of SiC: cubic zinc blend (β-form) and hexagonal wurtzite (α-form). In all crystal forms, every Si-atom and every C-atom are surrounded by four covalently linked next neighbors, thus, SiC crystals are built out of either SiC_4- or CSi_4-tetrahedrons (see **Figure 4.2**).

For building a three dimensional structure of SiC tetrahedrons, one can either put the second layer parallelly or antiparallelly with respect to the first one. Both of these arrangements are shown in **Figure 4.2:** cubic zinc blend (β-form) and hexagonal wurtzite (α-form).[24,25] In the case of cubic modification all tetrahedron layers are parallel, but in the hexagonal modification all combinations are possible.

The above mentioned two lattice types are realized in the two simplest SiC-modifications The first modification is 3C-SiC (β-form); it has cubic symmetry and corresponds to zinc blend structure. In this case, the second tetrahedron layer is oriented parallel to the first one in a way that the center atoms are placed on the top of the voids of the first layer. In 3C-SiC structure, the sequence of atomic planes is ABC, that is, the fourth layer is identical to the first one. The second modification is 2H-SiC (α-form), it has hexagonal symmetry and corresponds to wurtzite structure. In α-modification, the third layer can either be identical to the first layer (leading to the most hexagonal 2H-modification) or it can follow to the second layer, thus, forming an antiparallel layer. The same is true for subsequent layers. The simplest 2H-SiC has the sequence AB, but in some of the more complicated modifications 50 or more different layers can be stacked on top of each other before one corresponds the first layer.[9]

The hexagonality of a SiC lattice is inversely related to the Si/C ratio[26] and the increase in hexagonality corresponds to the increase in the bandgap of the material. The bandgap of cubic 3C-SiC is reported to be 2.2 eV, in the case of hexagonal 6H-SiC it is 2.9 eV, and hexagonal 4H-SiC has a bandgap of 3.3 eV.[9] The bandgap of the 'most hexagonal' 2H-SiC form does not fit into this pattern because of applying a different method in bandgap estimation.[9]

Thermodynamically, the cubic modification of SiC is the most stable one, it is also known as the low temperature modification because it is formed at 1400 °C. At higher temperatures starting at 2200 °C, it is initially transformed into the 2H- and then into 6H-modification. Although the 6H-SiC appears to be the most stable modification at high temperatures, but because of the small energy differences between the modifications the formation of mixed crystals during a fabrication is common.[14]

4.1.0.2. Silicon Carbide Powders

Several silicon carbide powders were obtained for use in photocatalysis experiments. The first powder was Norton FCP-15-NLC α-SiC (batch 34/92) which is a 0.7 μm average particle size powder designed for sinterability. The second powder was a p-doped α-SiC powder from Carbalon. Finally, because of concerns about the purity and dopant contents of these two powders, we obtained two SiC powders from Dr. John Haggerty's lab at MIT. These powders were made by a vapor phase, laser-induced reaction of methane and silane and were composed of sub-micron β-phase particles. Because of the special synthesis process, we hoped that these powders would have high purity. One of the two powders was doped with boron by using a silane tank that had a diborane (B_2H_6) content of 0.08% which should give a boron content in the

powder of about $3x10^{19}$ B atoms/cm^3 ans also provide p-type SiC. The other powder was not doped with boron. Both powders were synthesized at a silane to methane ratio of one.

The Norton and Carbalon powders were gray while the MIT powder was black. The MIT powder was coated with graphite (see **Figure 4.3(a)**) as analyzed by X-ray Diffraction (XRD). After heating in air for 2 hour at 1000 °C the MIT powder turned gray, indicating that the surface graphite had been removed by oxidation, however, it was still in the β crystal phase. The MIT powder was then converted to the α-phase by heating them in gettered argon to 2000 °C for 2 hour. The conversion was verified by powder XRD (see **Figure 4.3(b)**).

Before using any of the SiC powders in a photoexperiment, it was treated with 50% HF solution for two hours under an anaerobic atmosphere in a Teflon beaker. Argon gas was used with a constant flow to remove ambient oxygen from the HF-treatment bath. After decanting the supernate HF solution from the Teflon bath, the remaining SiC material was rinsed copiously with deareated deionized water. This pretreatment procedure was necessary to remove the passive silica overlayer and bring out the photoactive SiC surface. Fresh SiC sample, after similar HF-treatment, was used for each of the pot reactions. Investigation of SiC powders with transmission electron microscopy (TEM), performed at the University of New Mexico, has also confirmed that the HF-treatment removed an amorphous SiO_2 layer from the surface. A TEM picture of HF-treated SiC is shown in **Figure 4.4(a)** which is not obtainable in presence of a silica overlayer.

A composite of TiO_2/SiC was prepared at the laboratory of Prof. Abhaya K. Datye of the University of New Mexico by thermochemical deposition of TiO_2 onto SiC powder.[27] An amorphous titania layer was formed from a thermal decomposition of ethanolic solution of titanium n-butoxide when refluxed and then heated overnight at 110 °C. In the composite

mixture, the material ratio between TiO_2 and SiC was calculated to be 0.25 using an X-ray fluorescence technique. A high resolution TEM picture of the composite is shown in **Figure 4.4(b)**. We also tested the photoactivity of this composite using a method described in **Section 4.1.1.0**.

An impurity analysis was performed on all four powders using semiquantitative ion microprobe mass spectroscopy (SIMMS) as shown in **Figure 4.5**. This type of analysis is complicated by the fact that different elements have secondary ion yields that vary by over 4 orders of magnitude and that depend on the matrix that they are in. The analysis indicated that in terms of p-type dopants, the Carbalon powder had only Al, the Norton powder had trace amounts of both B and Al, the undoped MIT powder had a small amount of Al and the B-doped MIT powder had small amounts of both B and Al. In terms of impurities, the Carbalon powder had significant amount of Na and K present, whereas the MIT powders had 10 to 20 times less of these elements. The Norton powder had small amounts of Ti and possibly V, whereas the MIT powders had these two impurities plus a trace amount of Cr. The Carbalon powder also had Ti, V and Cr, and in addition had Zr and possibly Ba, La, and Ce and several unidentified peaks. Overall, the Carbolon form of SiC powder exhibited the highest purity.

4.1.0.3. Silicon Carbide Pellets

Single crystal SiC sheets with an area of 1 cm^2 were procured from CREE Research Inc., Durham, North Carolina. After initial photocatalysis experiments with p-doped α-SiC single crystals indicated some photocatalytic activity, similar experiments with polycrystalline SiC pellets were attempted for several reasons. First, photocatalysis experiments can be performed more readily on bulk samples than on powders. Second, ohmic contact can be made to bulk samples

more easily than to powders. Finally, since the bulk samples would be made from powders that we eventually hoped to use in powdered form, these experiments might indicate whether SiC of the purity available as commercial powders would be photocatalytically active. Therefore, we hoped to be able to fabricate bulk α-SiC pellets that had the proper p-dopant concentration, had no open porosity, and no second phases, especially ones that were interconnected that would isolate the SiC grains.

Unfortunately, we could not produce samples that met all of the above requirements simultaneously. This was due to the difficulty of densifying SiC: in order to obtain a high density after sintering or even after hot pressing, a p-dopant concentration of several tenths of a weight % is necessary. This is more than ten times that desired for photocatalytic activity. Also, excess carbon is required for densification which may result in a carbon-rich grain boundary phase after heat treatment. Recognizing these potential problems, we decided to fabricate some pellets and determine their photocatalytic behavior.

Two different commercial silicon carbide powders were used: Norton FCP-15-NLC and Carbalon. Prior to use, the powders were chemically treated to remove any oxide surface layer either by boiling for 3 hours in an 8 wt% NaOH solution or by washing for 3 hours in a concentrated HF solution at 80°C. In either case, the powder was thoroughly rinsed with deionized water and then dried. Several sources of carbon were used including (poly)isobutylene (which most likely decomposed without leaving any carbon behind) to graphite powder to

Table 4.1. Compositions and conditions used for hot-pressing SiC pellets.

	Carbon	**Boron**	**Aluminum**	**Pressure** (psi)	**Time** (min)
A	2.5 wt% from (poly)isobutlyene	0.3 wt% Eagle Picher Natural Xtalline Boron	0.3 wt% Fisher Finest Powder	4000	60
B	3.0 wt% Aquablack Graphite	0.5 wt% Callery Sub-Micron Boron		4000	60
C	5.0 wt% Ultracarbon Graphite		0.5 wt% Fisher Finest Powder	4000	60
D	5.0 wt% from Phenolic Resin		0.5 wt% Fisher Finest Powder	4000	60
E	5.0 wt% from Phenolic Resin	0.01 wt% Callery Sub-Micron Boron		6000	120

phenolic resin (which leaves a known amount of carbon behind after decomposition). As mentioned above, the use of carbon source was necessary for obtaining a dense material to be able to manufacture SiC pellets. The SiC, carbon source and dopants were weighed in various ratios as shown in **Table 4.1** and then mixed together prior to hot pressing. All hot pressing was done with soak temperature of 2050°C in gettered argon. Typical pressures and times are also given in the table. After hot pressing, samples that contained several tenths of a percent of B and/or Al reached nearly theoretical density while sample E with only 0.01 wt % B reached only 78% of theoretical density. Analysis of the samples by x-ray diffraction indicated that they were 6H α-SiC (see **Figure 4.5**). Ohmic contacts were applied to one surface of the pellets by evaporating on a thin coating of Si-Al eutectic alloy using a vacuum evaporation coater. The pellets were heated to 950°C for 10 minutes in gettered argon to form the ohmic contact between the SiC and the coating. This procedure was also demonstrated to be effective for producing an ohmic contact on single-crystal test specimens.

4.1.1. Methods

4.1.1.0. Pot Reactions with SiC and TiO_2 Powders

We have used the same pot reactor as described in **Section 2.1** (see also **Figure 2.3**) for monitoring kinetic photo-experiments on aqueous suspensions of SiC and TiO_2 powders using the reduction of methyl orange as a probe. Different grades of commercial and laboratory samples of SiC and P25 grade of TiO_2 were used for these photo-experiments. All SiC powders were pretreated for 2 hours in 50% HF at room temperature and then rinsed with deareated deionized water to remove any surface oxide layers prior to their use in photocatalysis experiments.

Kinetic information for the reduction of methyl orange (MO) was obtained from concentration versus time data for various initial concentrations of MO and Na_2EDTA, a hole scavenger. To obtain these data, we used an argon-purged, if not mentioned otherwise, batch reactor to perform the photoreduction of MO in the presence of Na_2EDTA and either SiC or TiO_2 powder. For each experiment, a 300-mL aqueous suspension of SiC or TiO_2 with reactants at appropriate concentrations and with prior pH adjustment was placed into the reactor.

During each reaction, reaction temperature was held constant at 20.0 ± 0.1 °C and the reactor contents were stirred constantly under a continuous flow of argon. The reactor is covered externally with aluminum foil to reduce light losses.

During each experiment, 2-mL samples were collected at specified times with an air-tight valve and syringe. Samples are filtered through 0.2-μ Teflon syringe filters to remove the catalyst before spectral analysis with a UV-visible diode-array spectrophotometer calibrated for different MO concentrations.

All chemicals were reagent grade. Cr(VI) was analyzed colorimetrically using diphenylcarbazide.[28] The light source used was a 100-W UV spot lamp (Sylvania Par 38 mercury bulb) having an integral output (12 cm away) of 39 mW/cm^2 between 300 nm and 390 nm.

In addition to a series of kinetic photocatalysis experiments, we also performed a study of the adsorption of MO onto SiC. This was done to quantify the magnitude of adsorption and to provide data that might be useful in understanding the kinetics on SiC. The amount of MO adsorbed is calculated from the analyses of MO contents in the samples before and after the addition of SiC using UV-Vis absorption. For these tests, the chemical components were added

to 300 mL of carbon filtered and deionized water (~1 μmho - cm) in the order of MO and SiC. Adsorption usually reaches steady state within 15 minutes of SiC addition.

4.1.1.1. Photoelectrochemical Cells with SiC and TiO_2 Electrodes

The experimental set-up consisted of a small electrochemical cell, which could be filled with solution and nitrogen-purged to eliminate the presence of oxygen if necessary. The bottom of the cell was a quartz crystal lens, covered by a shutter which would either permit or prevent the ultraviolet light's illumination of the electrode surfaces. The cell had a water-cooled jacket that was kept at a constant temperature of 20 ^{o}C for all experiments. This cooling eliminated possible differences or errors which might have been caused by thermal effects. The actual electrodes were inserted through a rubber stopper and suspended in the solution alongside one another. The design of the photoelectrochemical cell insured an approximately equal light intensity on both semiconductor electrode surfaces (see **Figure 4.7**).

The electrodes were cleaned between each run with aqua regia (HNO_3 and HCl mixed in a solution in a 3:1 ratio) for both of the electrodes and the SiC electrode was etched with 50% HF for 2-4 minutes before and after each run to insure the removal of any silica overlayer formed on the electrode surface. After the acid-treatment, the electrode surfaces were cleaned with isopropyl alcohol if they had been exposed to organics (salicylic acid), and then each electrode was rinsed in deionized water and put into storage for subsequent usage.

Open Circuit Voltages and Short Circuit Currents: The first experiment involved connecting the TiO_2/SiC cell to a multimeter and measuring the open circuit voltage and short circuited current for both illuminated and non-illuminated electrode systems, using a platinum wire as a reference electrode. The values were taken by connecting the multimeter to the

electrodes, always having the negative lead hooked to the silicon carbide electrode and the positive lead connected to the titanium dioxide electrode.

For measurement, the system was allowed to reach a pseudo-steady state (no change in current or potential) and readings were then taken of short circuit current and open circuit voltage. This was done for all of the metals in the series of gold, platinum, palladium, chrome, nickel, cadmium, copper, mercury, and silver in 0.5 mM solutions with salicylic acid.

Current/Potential Curves Using Potentiostat: This set of experiments were run in a similar fashion to the multimeter experiments. The working electrode was chosen by using the following order of preference: silicon carbide, titanium dioxide, then platinum. Therefore, if silicon carbide were in a system, it was always the working electrode. Platinum was always used as the reference electrode. Standard calomel electrode (SCE) was also used as a reference electrode. An SCE was fabricated and tested for use in conjunction with the TiO_2/SiC diode system. This was done in an attempt to negate any possibility of reaction taking place at the reference electrode.

From this setup, current vs. potential curves were obtained, using a chart recorder, for both illuminated and dark electrode systems. This allowed not only the measurement of the open circuit voltage and short circuit potential, but also the measurement of current as a function of changing the applied voltage to the system. This provided further information about how the system was responding to illumination.

Photodiode Efficiency: In order to measure the potential/current curves for the TiO_2/SiC diode couple, a variable resistor was connected to an ammeter in series with the electrodes, adjusting the resistance to obtain a series of data. This data consisted of current through the resistor, which was measured by the ammeter. The values of the resistance and current were then

used to determine the voltage output (or drop across the resistor) for the cell. A schematic representation of this setup is shown in **Figure 4.8**.

SiC Pellets: A series of monolithic SiC wafers were obtained and used as electrodes to determine their photoactivities. These SiC wafers included electrodes doped with boron, carbon, and a polymeric organic compound. The testing involved etching the surfaces with HF, and then exposing them to a solution of deionized water with $CuSO_4$ present and measuring the current and potential of the system with a potentiostat connected to a chart recorder.

4.2. Results and Discussions

4.2.0. Kinetic Studies on Photoreduction of Methyl Orange

A series of kinetic experiments for the photoreduction of MO under variety of conditions are shown in **Figures 4.9 - 4.14**. It is clear from **Figure 4.9** that etching SiC powder with 50% HF solution for a period of two hours is necessary before significant photoreduction can occur. Photoreduction experiments in **Figure 4.9** were performed at pH 4.4, in presence of 0.2% Carbolon SiC and an excess of EDTA (10 mM). Initial MO concentration for all of the pot reactions was 60 μM. EDTA is known to be an efficient hole scavenger and, thus, forces the photoreduction to occur at its maximum rate (see below). The pretreatment with HF enhanced the initial rate of photoreduction of methyl orange (to its hydrazine derivative) on SiC by an order of magnitude when compared to that of untreated SiC. As noted in the previous section, investigation of SiC powders with transmission electron microscopy has confirmed that the HF-treatment removed an amorphous SiO_2 layer from the surface.

The dependence of initial photoreduction rate of MO on pH (0.2-wt% Carbolon SiC) is shown in **Figure 4.10**. The initial rate of MO photoreduction is shown to decrease with

increasing pH (for the range 4.4 - 9.0). This observation can be related to the decrease in concentration of a specific form of methyl orange as well as its decreased adsorption on SiC at higher pH (see **Figure 4.11**). The dependence of initial photoreduction rate of MO on EDTA (0.2-wt% Carbolon SiC) is shown in **Figure 4.12**. The initial MO photoreduction rate is enhanced by an order of magnitude when EDTA concentration is increased from zero to 10 mM. However, it should be noted here that initial photoreduction rates are practically similar and insignificant for untreated and HF-treated powders if no EDTA is added to the reaction mixtures.

Photoreduction of MO on different grades of SiC (Carbolon and Norton), TiO_2 (P25 and Tioxide), and TiO_2-coated SiC are shown in **Figure 4.13**. Several observations are made from this figure. First, Carbolon grade is a better photocatalyst than Norton grade SiC. Second, the MO photoreduction by SiC is slower by over an order of magnitude than that by any of the TiO_2 grades. Finally, TiO_2-coated SiC shows comparable photoresponse to those of TiO_2 which is probably because of the predominant photoactivity by the TiO_2 overlayer. However, the presence of SiC made the TiO_2 photoactivity slower than its normal photoactivity and this lower photoactivity may be attributed to an overall lower loading of TiO_2 (dispersed on SiC) when compared to that of bare TiO_2.

In spite of a poor photoreductive capacity of all of the SiC powders in compared to that of TiO_2, we have found that Carbolon SiC can be used to remove Cr^{+6} from aqueous solution in the presence of Na_2EDTA (see **Figure 4.14**). However, P-25 grade TiO_2 outperforms SiC for photoreduction of Cr^{+6}. For both cases of SiC and TiO_2, higher Cr^{+6} photoreduction rate is

Table 4.2. Initial rate for the photoreduction of methyl orange in presence of 10 mM Na_2EDTA at pH 4.4.

Photocatalyst	**Initial Rate** (μmoles/min)	**Photoefficiency** (%)
None	0.006	0.002
Untreated SiC:		
0.2% Carbolon[a]	0.006	0.002
0.2% Carbolon[b]	0.027	0.01
0.2% Carbolon	0.027	0.01
50% HF-treated SiC:		
0.2% Carbolon	0.138	0.04
0.1% Carbolon	0.105	0.03
0.2% Norton	0.036	0.01
TiO_2:		
0.1% P25	6.84	1.95
0.1% Tioxide	8.25	2.35
TiO_2-coated SiC (Carbolon):		
0.1% TiO_2 (SiC)	1.05	0.30

[a]Room light; [b]ambient oxygen, all others were Ar-purged.

Table 4.3. Initial rate for the photoreduction of Cr^{+6} in the presence of 1 mM Na_2EDTA at pH 4.4 and 2.0. All experiments were performed under Ar-purged conditions.

Photocatalyst	**pH**	**Initial Rate** (μmoles/min)	**Photoefficiency** %
50% HF-treated SiC:			
0.2% Carbolon	4.4	0.58	0.17
0.2% Carbolon	2.0	3.64	1.04
TiO_2:			
0.1% P25	4.4	10.90	3.12
0.1% P25	2.0	36.12	10.33

observed with the increase of pH. Our observations indicate that the redox processes on SiC most likely occur via processes similar to those known for TiO_2.

Based on the results shown in **Figures 4.9 - 4.14**, calculated % photoefficiency on SiC and TiO_2 powders are shown in **Tables 4.2** and **4.3** for MO photoreduction and Cr^{+6} photoreduction, respectively. The best case of MO photoreduction rate on SiC (0.1% Carbolon with 10-mM EDTA at pH 4.4) shows 0.03 % photoefficiency whereas Tioxide TiO_2 shows 2.35 % photoefficiency under similar experimental conditions; a difference of about two order of magnitude in their photoactivities. A similar conclusion can be made from their activities for the photoreduction of Cr^{+6}. If we consider the relative positions of the conduction bands (at pH 4.4) for TiO_2 (- 0.22 V vs. NHE)[2] and SiC (- 1.72 V vs. NHE)[29] in relation to the reduction potentials of MO (- 0.06 V vs. NHE)[4] and Cr^{+6} (1.33 V vs. NHE),[5] a higher photoreduction rate is expected for the case of SiC when compared to those for TiO_2 In contrast, our results show an opposite trend. To be able to understand these counterintutitive observations, similar experiments with other metal ions like Cd^{+2}, Ni^{+2}, Ag^{+}, Hg^{+2}, etc. need to performed.

4.2.1. Photoelectrochemical Experiments With TiO_2/SiC System

4.2.1.0. Multimeter and Potentiostat Measurements with Pt Reference Electrode

Both the multimeter testing and the potentiometer results showed that the electrode system seemed to be working to a marginal degree on most of the metals. The only exceptions to this were the results obtained for the noble metals (Au, Pt, Pd) and chromium (Cr). For these metals, very little current was seen in the potentiostat readings, especially where the silicon carbide electrode was involved. The observed small current responses are believed to be partially due TiO_2's ability to reduce these metals. It may have been the case that the metals quickly

deposited on the surface of the electrodes (SiC or TiO_2) and then blocked any additional light from the surface, thereby reducing the current that was observed. However, for the most part, the results of the two sets of experiments seemed to reinforce each other (see **Figures 4.15** through **4.22**). From the data, it is reasonably obvious that the system was reducing the metals in question. Also visual inspection verified the deposition of some of the metals, Cu and Ni, on the SiC surface.

4.2.1.1. Potentiostat Measurements with SCE Reference Electrode

For these tests, only copper, nickel, and mercury ions were chosen to be evaluated for their reduction currents on the electrode systems. It was observed that for the silicon carbide electrode, the amount of current for a given applied voltage decreased when salicylic acid was introduced into the system, and depended only slightly upon which metal was present in the electrolyte solution (see **Figure 4.23**). An opposite effect was dominant in the TiO_2/Pt electrode couple(see **Figure 4.24**). The presence of salicylic acid in the TiO_2 system was found to be significant in determining the amount of photocurrent seen and also depended on the metal in solution. The photocurrent-potential results are presented in **Figures 4.23** and **4.24** for TiO_2 and SiC photoelectrochemical systems, respectively.

In general, the results which were obtained using the SCE as a standard reference electrode showed larger current densities than in the Pt reference case. This difference was on the order of several hundred microamps. It is believed that this was due to the "floating" nature of the platinum electrode and its susceptibility to reaction on its surface.

4.2.1.2. Photodiode Efficiency of SiC/TiO_2 by Measuring Current/Potential

The final test was to use a variable resistor to measure the cell efficiency by plotting potential versus current. The variable resistor worked well in the determination of a potential versus current diagram which showed the efficiency of the cell as well as the open circuit potential for the illuminated cell (see **Figure 4.25** - a semilogarithmic plot). Overcurrent voltages for the respective electrochemical systems are listed at the top of the figure in a chronological order as shown by the ligends at the right side of the figure. From these results, one can conclude that the SiC/ TiO_2 diode cell efficiency was mostly independent of the type of metal ions used, but the pH of the solution (systems with deionized water only) had a significant effect on the cell efficiency as well as on maximum cell voltage and current density. The increase of the solution pH shifted maximum current density, open circuit voltage, and overall cell efficiency to higher values. The efficiency of the cell can be viewed from the squareness of the curves.

Additionally, considering the observations from TiO_2/SiC diode system in conjunction with those from SiC/Pt and TiO_2/Pt, it is clear that the reaction occurring on the SiC electrode is the rate limiting for the diode. The current density for TiO_2/Pt is in the thousands of microamps, whereas that for SiC/Pt is on the order of 50-100 microamps (see **Figures 4.23** and **4.24** for comparison). From **Figure 4.25**, although the photo-responses seem to be dependent on the solution pH, no clear correlation between cell efficiency and metal ion type is evident especially since the curves of each of these metals follow nearly identical paths.

The primary problem with the SiC/ TiO_2 photodiode system lies in keeping an active SiC surface where reaction can take place. SiC has a tendency to form SiO_2, and the electrode had to be etched with 50% HF after every run to insure that the surface remained active. Additionally,

tests done with monolithic SiC electrodes show that the activities in single crystal SiC electrodes do not transfer well to their multicrystalline (sintered) analogs. Additionally, the system seemed to be limited by the current through the SiC electrode. Furthermore, if one examines at the plots of standard redox potential vs. photocurrent density of all three TiO_2/Pt, SiC/Pt, and TiO_2/SiC systems, TiO_2 shows a relatively clear pattern to its response to metal types, whereas SiC shows a relationship which is less easily discerned (results not shown). It can be seen, moreover, that the TiO_2/SiC couple resembles the SiC/Pt far more than the TiO_2/Pt couple.

4.3. Theoretical Modeling for n-p Photodiodes

4.3.0. Theory

A schematic diagram for the proposed dual photoelectrode system involving p-type and n-type semiconductors is given in **Figure 1.8**. For the model calculations in this part of the project, the reactions at the photocathode and the photoanode are described below.

At Photocathode (e.g., p-SiC):

$$M^{2+} + 2e^- \rightarrow M°_{ads} \quad (1)$$

At Photoanode (e.g., n-TiO_2):

$$OH^- + h^+ \rightarrow OH\bullet \quad (2)$$

$$\text{Organic} + OH\bullet \rightarrow \text{Products} \quad (3)$$

or

$$\text{Organic} + h^+ \rightarrow \text{Organic}^+ \quad (4)$$

or in the absence of oxidation of organics,

$$4OH^- + 4h^+ \rightarrow O_2 + 2H_2O. \quad (5)$$

4.3.0.0. Cell Photocurrent Density Involving Dual Semiconducting Electrodes

Using the procedure of Kainthla et. al.[19] one can write an equation for the cell photocurrent density (including various important properties of both n-type and p-type semiconductors) for a dual semiconductor photoelectrode system as

$$I_{cell} = 2\, I_d^P\, I_d^n \{(I_d^P + I_d^n) + [(I_d^P - I_d^n)^2 + 4\, I_d^P\, I_d^n \cdot \exp[-(Ea^A + Ea^D)/kT]\, \xi \exp(e_o\, V_{cell}/2\, kT)]^{1/2}\}^{-1} \quad (6)$$

where, photocurrent density at p-type semiconductor electrode (I_d^P) is expressed as

$$I_d^P = e_o\, (N_a/N_t) \int_{v1}^{v2} \{(1-R_v)\, (I_v) \cdot [1 - (e^{-\alpha_v W})/(1 + \alpha_v L_D)(1 + G/L_D) - (G\, e^{-\alpha_v W})/(L_D + G)]\}dv \quad (7)$$

and I_d^n is given by an expression similar to **Equation (7)** with relevant parameters for an n-type semiconductor.

In **Equation (7)**, N_a is the number of acceptor metal ions in the unit area of the reaction plane, N_t is the total number of sites in the area of the reaction plane, R_v is the reflection coefficient of the photon at the semiconductor surface, I_v is the intensity of incident photon, α_v is the photon absorption coefficient, ν_1 (=E_g/h where h is Planck's constant) is the lower frequency limit of light corresponding to the bandgap energy (E_g) of the semiconductor, ν_2 is the upper frequency limit of the UV light source, L_D is the diffusion length of an electron, and W is the width of the depletion region that can be expressed as[18]

$$W = (2\, e_o\, \varepsilon_s\, V_{bb}^P / e_o\, N_D)^{1/2} \quad (8)$$

and the constant G for a specific semiconductor type

$$G = (\pi kT \varepsilon_0 \varepsilon_S/2 e_0^2 N_D)^{1/2} \quad (9)$$

where ε_0 is the permitivity of a vacuum, ε_S is the dielectric constant of semiconductor, V_{bb}^P is the band bending potential in the p-type semiconductor electrode.

In **Equation (6)**, the effective activation energy, E_a^A of acceptor ions in solution can be expressed as

$$E_a^A = [E_a^0 + (E_{ads,m}/2 - e_0 E_{red}^0/2)] \quad (10)$$

where

$$E_a^0 = (E_{r,i} + E_{r,o})/4 \quad (11)$$

where E_a^0 is the activation energy contribution from the reorganization energy of inner and outer solvent spheres, respectively.[30-32] $E_{r,i}$ and $E_{r,o}$ are the inner and the outer sphere reorganization energies, respectively, of the metal acceptor ions (in the absence of adsorption on the electrode surface), $E_{ads,m}$ is the adsorption energy of metal ions on semiconducting surface and E_{red}^0 is the reduction potential of the metal ion.

The term $E_{ads,m}$ in **Equation (10)** can be expressed as[33]

$$E_{ads,m} = 1/2 (D_{M-M} + D_{H-H}) + 23.06 (\chi_M - \chi_H)^2 \quad (12)$$

where D_{M-M} and D_{H-H} are the bond energies of M-M and H-H, respectively, and χ_M and χ_H are the electronegativities of M and H ions, respectively.[19]

The term E_a^D in **Equation (6)** is the activation energy of the donor species in the solution and can be expressed as

$$E_a^D = [E_a^0 + (E_{ads,OH^-}/2 - e_0 E_{ox}^0/2)] \quad (13)$$

where E_{ads,OH^-} is the adsorption energy of OH^- on n-type semiconductor surface and E_{ox}^0 is the standard oxidation potential of the donor ion. According to the report by Ruetschi and Delahay[34] the adsorption energy of OH^- can be expressed as

$$E_{ads,OH^-} = (1/2)(E_{Diss,OH^-} + E_{Diss,M=O} - E_{Diss,H-OH} + E_{solv,M=O}) \quad (14)$$

where E_{Diss,OH^-}, $E_{Diss,M=O}$, and $E_{Diss,H-OH}$ are the energies of dissociation of O-H, M=O, and H-OH bonds respectively. $E_{solv,M=O}$ is the heat of hydration of the M=O bond. For compound semiconductors like TiO_2, it has been assumed that OH^- adsorption is dominated by bonding with the metal ions present in it.

The term ξ in **Equation (6)** can be expressed as[19]

$$\xi = (S_{th}^2/S_e\, S_h)\, P_T(E_c)\, P_T(E_v)\, \delta_{sr}^P\, N_{ss}^P\, \theta_{ss}^P\, \delta_{sr}^n\, N_{ss}^n\, \theta_{ss}^n \cdot \exp[(V_s^n - V_s^P + \chi^n - \chi^P)/2kT] \quad (15)$$

where S_{th} is the thermal velocity of outcoming photogenerated electrons in the surface region of the semiconductor. S_e and S_h are the velocities of photogenerated electrons and holes respectively. $P_T(E_c)$ and $P_T(E_v)$ are the tunneling probability across the interfacial barrier and the energy of the hole at the top of the valence band at the interface respectively. δ_{sr}, N_{ss}, θ_{ss}, V_s and χ are capture cross section for surface recombination, surface density of surface states, coverage of surface states, intrinsic band bending and electron affinity, respectively, for the specific type of the semiconductor as denoted by either of the superscripts 'P' or 'n' with the terms.

In **Equation (6)**, e_o is the electronic charge, and V_{cell} is the cell voltage.

4.3.0.1. Cell Efficiency

The percentage cell efficiency (% E_{eff}) can be expressed as[19]

$$\% E_{eff} = [I_{cell} V_{cell}/2 \int_{v1}^{v2} I_v h\nu dv] \times 100 \quad (16)$$

4.3.1. Computations

This involved computation of cell current densities and efficiencies of the binary system p-SiC/n-TiO_2 with various parameters of p-type and n-type semiconductors in aqueous solution on the basis of the theoretical model given above. These computations were made with a goal to identify the best system parameters of a p-type semiconducting photoelectrodes which match energetically well with n-TiO_2 photoelectrode for an enhanced photodetoxification of aqueous samples containing a wide range of metal ions and organics. These computations were carried out using Microsoft FORTRAN 5.1. A list of parameters that were used for these semiconductors and their platinized compositions are given in **Table 4.4**. These values were supplied by the commercial producers of SiC and TiO_2 materials. Values for activation energy (E_a^0) and free energy of adsorption (on the surfaces of bare and platinized SiC) are chosen from the literature, and values for redox potential[35] for selected metal ions and those for OH^- ion in relation to the TiO_2 surface are listed in **Table 4.5**.

4.3.2. Results and Discussion

4.3.2.0. Effect of Doping Density

The results of the effect of doping density of p-SiC and platinized p-SiC (SiC(Pt)) on the maximum cell current density (which is a measure of the rate of detoxification of polluted water

Table 4.4: Properties of semiconductors used.

Properties of Semiconductors	**p-SiC (and p-SiC(Pt))**	**n-TiO_2**
Bandgap (eV)	3.0	3.0
Carrier Density (cm^{-3})	2.0×10^{18}	2.0×10^{17}
Carrier Mobility ($cm^2\ v^{-1}s^{-1}$)	60	1.1
Electron Affinity (eV)	4.21	4.1
Diffusion Length (cm)	3.12×10^{-5}	1.0×10^{-4}
Dielectric Constant	10.03	170
Average Absorption Coefficient of Light (cm^{-1})	5.0×10^4	1.0×10^4

Table 4.5: Properties of reactants in solution used in model calculations.

Reactants	Activation Energy, E_a^0 (eV)	Free Energy of Adsorption (eV)		Redox Potential (Volt)
		p-SiC	p-SiC(Pt)	
Hg^{2+}	1.2	-1.42	-1.76	0.85
Cu^{2+}	1.2	-1.83	-2.24	0.34
Ag^{+}	1.2	-1.80	-2.22	0.80
Cd^{2+}	1.2	-1.58	-2.02	-0.40
Ni^{2+}	1.2	-2.15	-2.44	-0.23
Pb^{2+}	1.2	-2.21	-2.63	-0.126
		n-TiO_2		
OH^-	1.5	-2.10		0.60

under illumination) are given in **Figures 4.26(a)** and **4.26(b)**, respectively. These calculations are based on the assumption that the origin of current is solely from the desired oxidation reaction (see **Equations (7) and (8)**). Results from these figures indicate that with the increase in doping density the rate of reduction and, thus, deposition of metal ions decreases considerably for both SiC and SiC(Pt) systems. Similar patterns on the dependence of cell current density on the metal type are also followed, Ni^{+2} being the most active and Ag^{+} being the least active metal. These patterns are in direct contrast with previously observed experimental results especially for the case of TiO_2. Additionally, the doping density has minimal affect on cell current density in the presence of Ag^{+} ion and this may be due to a combination effect from a high adsorption free energy and a high redox potential for this specific metal ion. A doping density above 10^{16} cm^{-3} is shown to greatly lower the cell current density in unplatinized SiC, while at platinized SiC this lowering of cell current density is weak except at higher doping densities (by 2-3 order of magnitudes). These results suggest that a doping density closer to 10^{14} cm^{-3} would be more favorable for higher cell current density in presence of metal ions.

4.3.2.1. Effect of Diffusion Length

Curves a and b in **Figure 4.27** show the % efficiency (see **Equation (7)**)of SiC photocells as a function of selected values of electron diffusion length (which depends on diffusion coefficient and lifetime of photoexcited electrons) in the space charge region of SiC for two doping densities of 10^{14} cm^{-3} and 10^{18} cm^{-3}, respectively. These calculations of % efficiency are performed for the case when lead (Pb^{+2}) ion is present in the ambient solution for SiC photoelectrode. It is observed that the effect of diffusion length on cell efficiency is negligible for both cases of doping densities. A negligible decrease in cell efficiency is observed only when the

diffusion length for the conduction band electron is in the range of hundredth of a millimeter. However, the choice of doping density obviously made a significant effect on the values of % efficiency.

4.3.2.2. Effect of Free Energy of Adsorption

The effects of free energy of adsorption of photodeposited metals on p-SiC and platinized p-SiC from aqueous solution on calculated maximum cell current density (see **Equations (6) and (10)**) are shown in curves a and b, respectively, in **Figure 4.28**. For these calculations, doping density was 10^{14} cm^{-3} for both cases. It is observed from curve a that the influence of adsorption energy on maximum cell current density is considerable for bare SiC even though no trend for dependence could be identified. This can be attributed to the fact that E_a^A in **Equation (10)** contains other terms such as E_a^0 and E_{red}^0 and these have contributed to the net maximum cell current density. However, for the platinized SiC (curve b), the variation of maximum cell current density with free energy of adsorption is negligible. In other words, the assumed pre-deposition of platinum islets on SiC (platinized SiC) surface provides the higher limit of the maximum cell current density probably because of its higher energy of adsorption than any other metals tested within the scope of this project.

4.3.2.3. Effect of Redox Potential

Figure 4.29 illustrates the effect of the redox potential on maximum cell current density for SiC when theoretical doping densities are 10^{14} and 10^{18} cm^{-3} (see **Equations (7) and (8)**). For comparison, the experimentally obtained points are also shown where doping density is 10^{18} cm^{-3}. Although there is an agreement in changes of pattern of these curves, the experimental values are lower than those of theoretical ones especially for the cases of copper and silver ions.

In general, the theoretical values of maximum cell current density are calculated to be higher than the experimental ones, except for Ni^{2+} and Cd^{2+}.

4.3.2.4. Effect of Electrodeposited Pt Metal

The dependence of cell current density (see **Equations (7) and (10)** on cell voltage for different metal ions in the absence and presence of Pt metal islets on p-SiC surface is given in **Figures 4.30(a)** and **4.30(b)**, respectively. It is important to note that the presence of Pt islets improves the cell current density considerably at a certain cell voltage with in the range of tested potentials perhaps due to its higher free energy of adsorption. This suggests that platinized p-SiC should be used for better photoresponse for the reduction of metal ions present in polluted water. Alternatively, Pt metal islets on the surface may serve as catalytic centers on its own. This ambiguity cannot be addresses unless additional calculations and experiments are performed.

4.3.2.5. Effect of Light Intensity

The dependence of cell efficiencies with UV light intensity for the photoreduction of Pb^{+2} on SiC and SiC/Pt are shown in **Figures 4.31** for doping densities of 10^{14} and 10^{18} cm^{-3}. Over the range of UV light intensity, platinization of p-SiC sample at doping density 10^{18} cm^{-3} gives a ten fold increase in cell efficiency when compared to bare SiC. It is observed that at this low doping density (10^{14} cm^{-3}), there is no notable difference in cell efficiencies between bare and platinized SiC samples.

4.3.2.6. Effect of Activation Energy Contribution, E_a^0 from Solvent Reorganization

The influence of a variable term that was not computed is the activation energy contribution from reorganization of the solvent, E_a^0 (see **Equations (10) and (11)**). This term was taken as a parameter in our computation keeping it at a constant value of 1.2 eV for all metal

ions. However, because this value appears in the exponential term in **Equation (6)**, it will have lartge contribution on cell current density. Activation energy normally has a range of 0.5 eV to 1.5 eV. If the value of activation energy increases towards 1.5 eV, there will be a drop in cell current density; however, if the activation energy value approaches 0.5 eV, there will be a considerable increase in cell current density. This suggest that it is important to ascertain the actual values of activation energy for the individual metal ions in solution. However, at this time, there is no simple theoretical expression for estimating the activation energy of metal ions that are deposited on an electrode.

4.4. Conclusions

4.4.0. Powders

We performed kinetic photo-experiments on aqueous suspensions of SiC and TiO_2 powders using the reduction of methyl orange as a probe. An effective combination of these materials is expected to provide a larger range of redox potentials for oxidative and reductive photoprocesses when compared to the redox potentials provided by either of these individual materials.

We found that etching SiC with 50% HF solution for a period of two hours is necessary before significant photoreduction occurs. Investigation of SiC powders with transmission electron microscopy has confirmed that the HF-treatment removes an amorphous SiO_2 layer from the surface. The initial rate of photoreduction of methyl orange (to its hydrazine derivative) is found to decrease with increasing pH (for the range 4.4 - 9.0). This can be related to the relative unavailability of a specific form of methyl orange as well as its decreased adsorption at higher pH.

The photoreduction of methyl orange by SiC is slower by over an order of magnitude than that by TiO_2. Nevertheless, it can be used to remove Cr^{+6} from aqueous solution in the presence of Na_2EDTA. Our observations indicate that the redox processes on SiC most likely occur via processes similar to those known for TiO_2. Separate electrochemical investigations on single crystal TiO_2 and SiC proved the concept of the binary photodiode system.

4.4.1. Pellets/ Single Crystals

The study of titanium dioxide coupled with silicon carbide as a photodiode system for the reduction of metals and simultaneous oxidation of organics was undertaken during the summer of 1993. This was done to determine the photodiode's possible feasibility for water purification systems involving sunlight. The project progressed through several stages during the course of the summer.

First, measurements were taken with a multimeter of the open circuit voltage and short-circuit current against a platinum reference electrode. This was done for solutions of various metals mixed with salicylic acid in deionized water solutions of approximately 0.5 mM concentrations. These tests showed initially positive results for the metals studied, but did not provide a large amount of information about the diode system. Therefore, a second series of tests was run, this time using a potentiostat.

The potentiostat was used with the various types of metals, again with a platinum reference electrode and salicylic acid. From this series of tests, potential vs. current curves were obtained for both dark and illuminated systems of electrodes. This series of tests revealed that a standard reference electrode, such as an SCE (Standard Calomel Electrode) was needed to insure

that there was no reaction occurring at the reference (Pt) electrode. This, in turn, led to the third portion of the study -- the potentiostat with an SCE Electrode.

The standard calomel electrode (SCE) was used to measure the titanium dioxide and silicon carbide potential/current curves against a platinum auxiliary electrode. For the TiO_2/SiC couple, a variable resistor was used to plot a voltage versus current graph which yielded information about the diode system.

This information showed that the amount of current generated by the titanium dioxide portion of the electrode (1000's of $\mu A/cm^2$) was far greater than that of the silicon carbide electrode (50-100 $\mu A/cm^2$). Additionally, it was found that the current/potential plots for this diode system were nearly independent of metal type, but were found to be pH dependent. This led to the conclusion that the silicon carbide electrode was limiting the rate of reaction of the system, as the SiC/Pt photocurrent density curve was seen to be very similar to the SiC/TiO_2 curve.

4.4.2. Modeling

The efficiency of p-SiC/n-TiO_2 dual system improves considerably if one uses an optimum doping density in p-SiC. This value should be close to $1.0x10^{14}$ cm^{-3} or $1.0x10^{15}$ cm^{-3}. Among the other factors which strongly influence the efficiency of the p-SiC/n-TiO_2 binary system are the adsorption energy of metal ions on the semiconductor surface, the reorganization energy contribution to activation of metal ions in solution, and the redox potential of metal ions. However, the last two factors are the intrinsic properties of species in solution which cannot be controlled. It is possible to improve the adsorption energy species if a better electrocatalyst such as Pt in the form of islets is predeposited on the p-type semiconductor surface. Hence, one should

use platinized p-SiC in combination with n-TiO_2 for better photoresponse for the reduction of metal ions present in polluted water.

A remarkable improvement of cell efficiency of p-SiC/n-TiO_2 system occurs only when the intensity of the UV light source can be improved. This suggests that one should use a low bandgap platinized semiconductor that will absorb a higher intensity of light including the UV and visible spectrums. It should be noted that a bare, low bandgap p-type semiconductor without platinization may not be effective due to poor adsorption energy of metal on itand also due to corrosion.

4.5. Recommendations

Overall, the TiO_2/SiC photodiode system is capable of reducing metals that have been tested and also to oxidize salicylic acid, a model organic compound. This project helped understanding of what obviously is an extremely complicated photo-electrochemical system. It is now known that the SiC is the rate-limiting electrode and in the presence of organics, such as salicylic acid, it slows down the reduction process at the SiC electrode. Additionally, it is found that cell efficiency appears to be independent of metal ion type, but does have a pH dependence. However, ionic strength might have played a significant role at two extreme pHs of 3 and 14. Additionally, multicrystalline SiC electrodes show that there are still significant problems to be overcome in developing the process as a potentially cost-effective application for use in metals reduction.

Some suggestions for future work in this area include, but are not limited to:

1. Test overall solution ionic strength to determine its effect, if any, upon cell efficiency.
2. Look for a method of simultaneously cleaning and experimenting with silicon carbide, thereby, eliminating the need for etching with HF between runs.
3. Extend the project to use powder slurries of SiC and TiO_2.
4. Surface modification of SiC to stabilize it against oxidation while retaining catalytic ability.
5. Alternative semiconductors with similar bandgap and band potentials should be tested in place of SiC since it is not a competitive photocatalyst when compared with TiO_2.

4.6. Figures

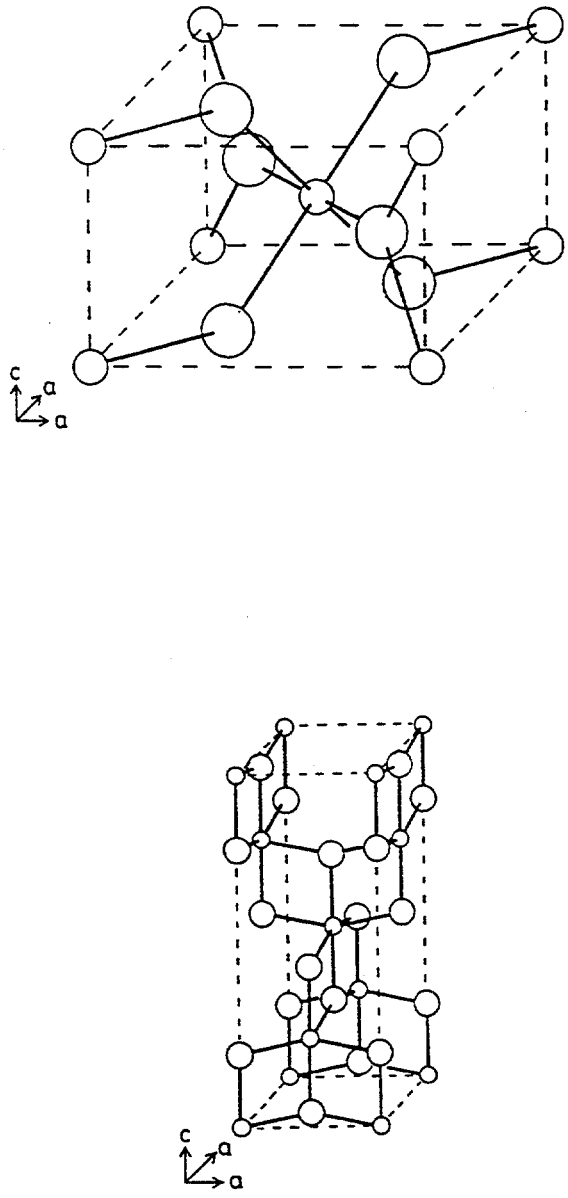

Figure 4.1. Unit cells for (a) rutile and (b) anatase. The small circles are the Ti cations and the large circles are the O anions.

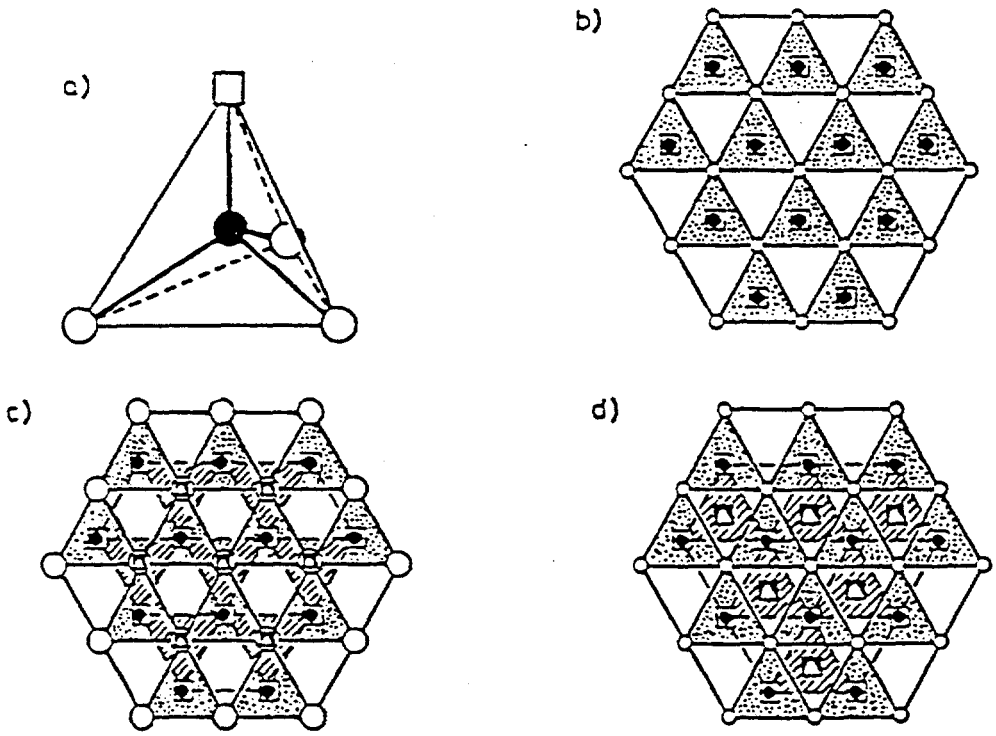

Figure 4.2. Model of the two simplest SiC lattices built from CSi_4-tetrahedons. o: first Si-layer, •: first C-layer, □: second Si-layer, ■: second C-layer, Δ: third Si-layer. **(a)** CSi_4-tetrahedrons perpendicular to the c-axis. **(b)** Monolayer of CSi_4-tetrahedrons perpendicular to the c-axis. **(c)** Two layers of CSi_4-tetrahedrons at 2H-SiC (hexagonal wurtzite structure). **(d)** Two layers of CSi_4-tetrahedrons at 3C-SiC (cubic zinc blend structure).

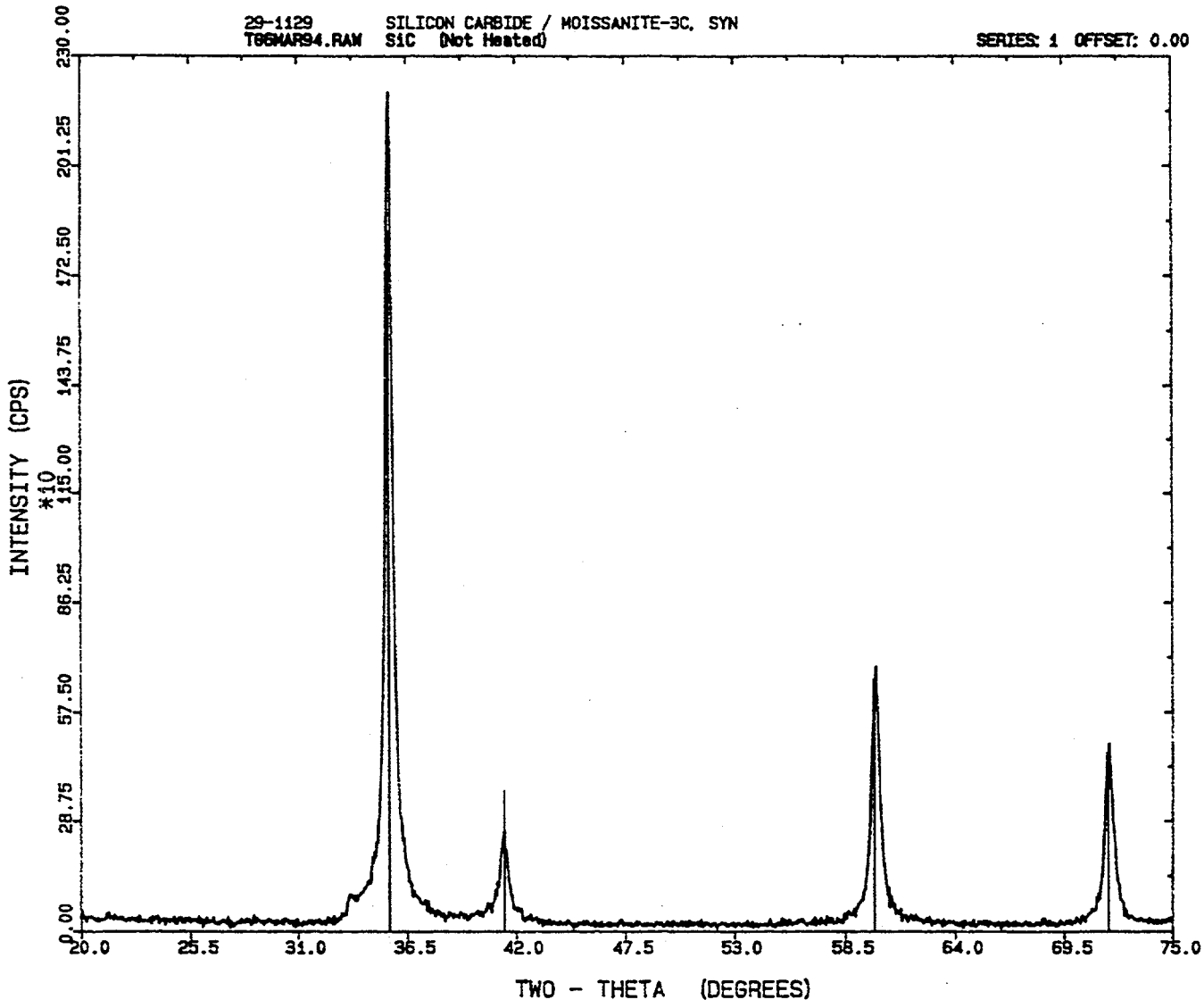

Figure 4.3(a). X-ray diffraction (XRD) analysis of a black MIT SiC powder as received.

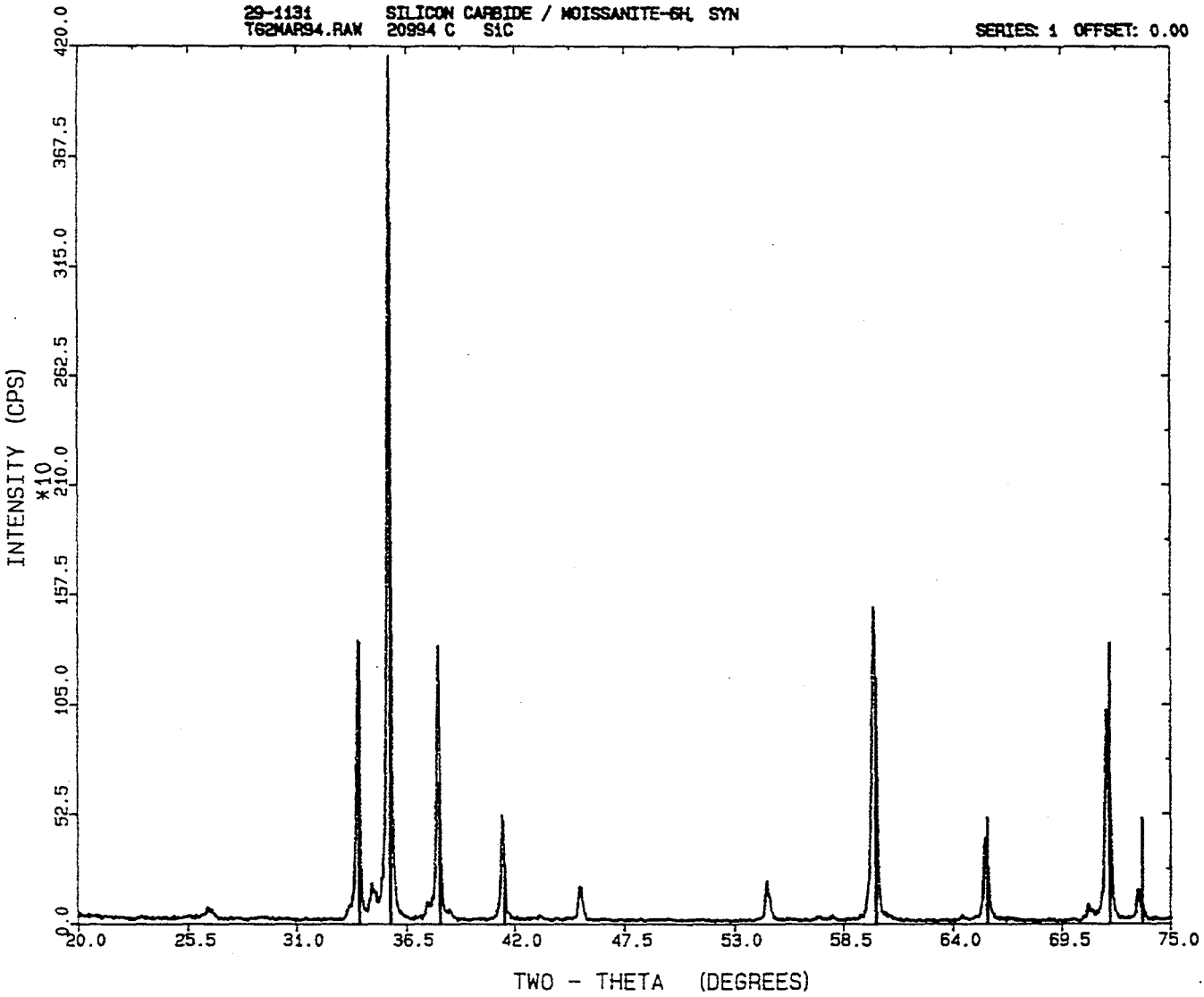

Figure 4.3(b). X-ray diffraction (XRD) analysis of a gray MIT SiC powder after heat treatments: first in air for 2 hours at 1000 °C and then for 2 hours at 2000 °C.

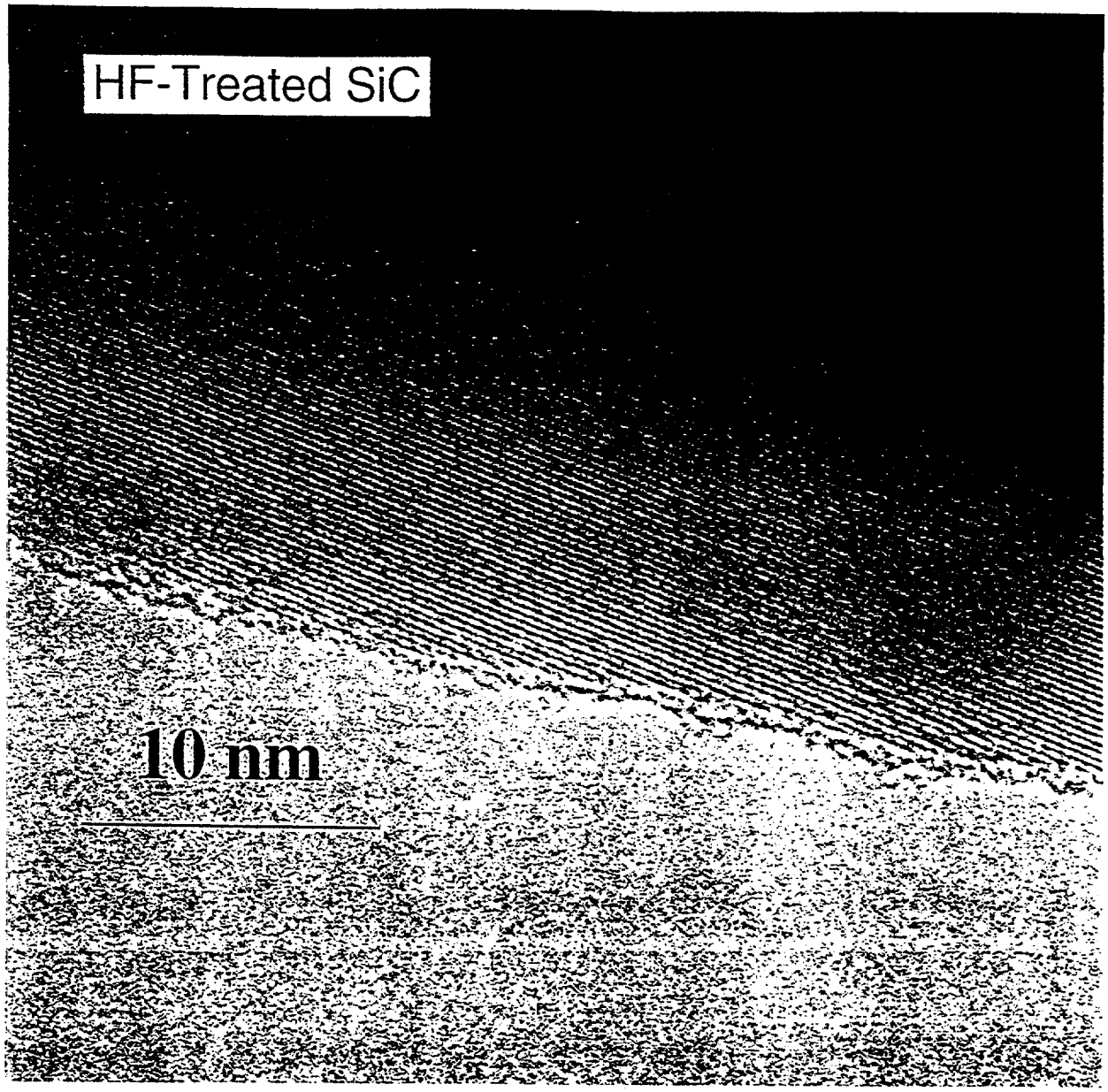

Figure 4.4(a). A high resolution picture of a HF-treated Carbolon SiC powder taken by transmission electon microscopy (TEM) with a magnification of 250,000 times.

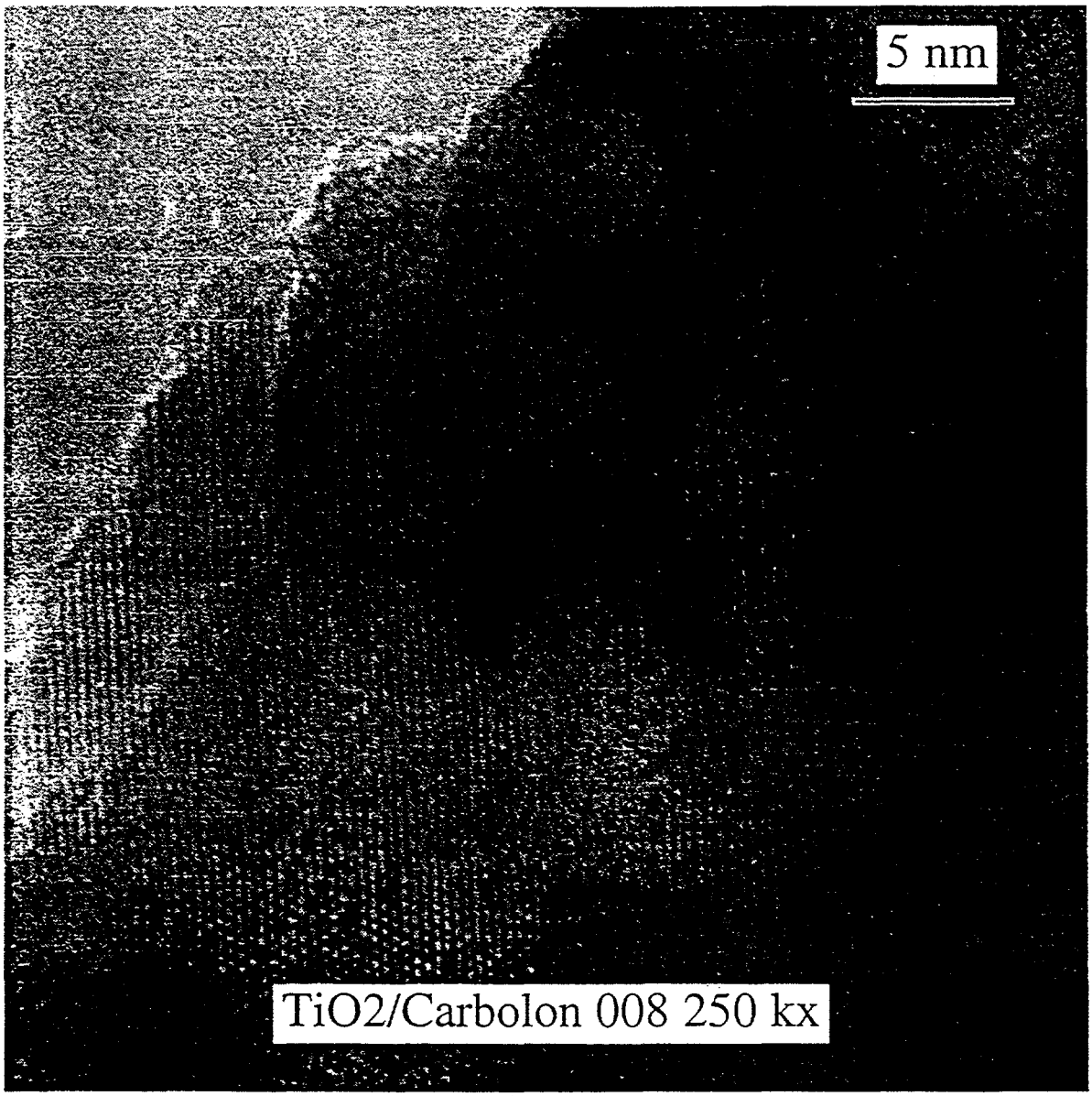

Figure 4.4(b). A high resolution picture of a TiO_2/SiC composite powder taken by transmission electon microscopy (TEM) with a magnification of 250,000 times.

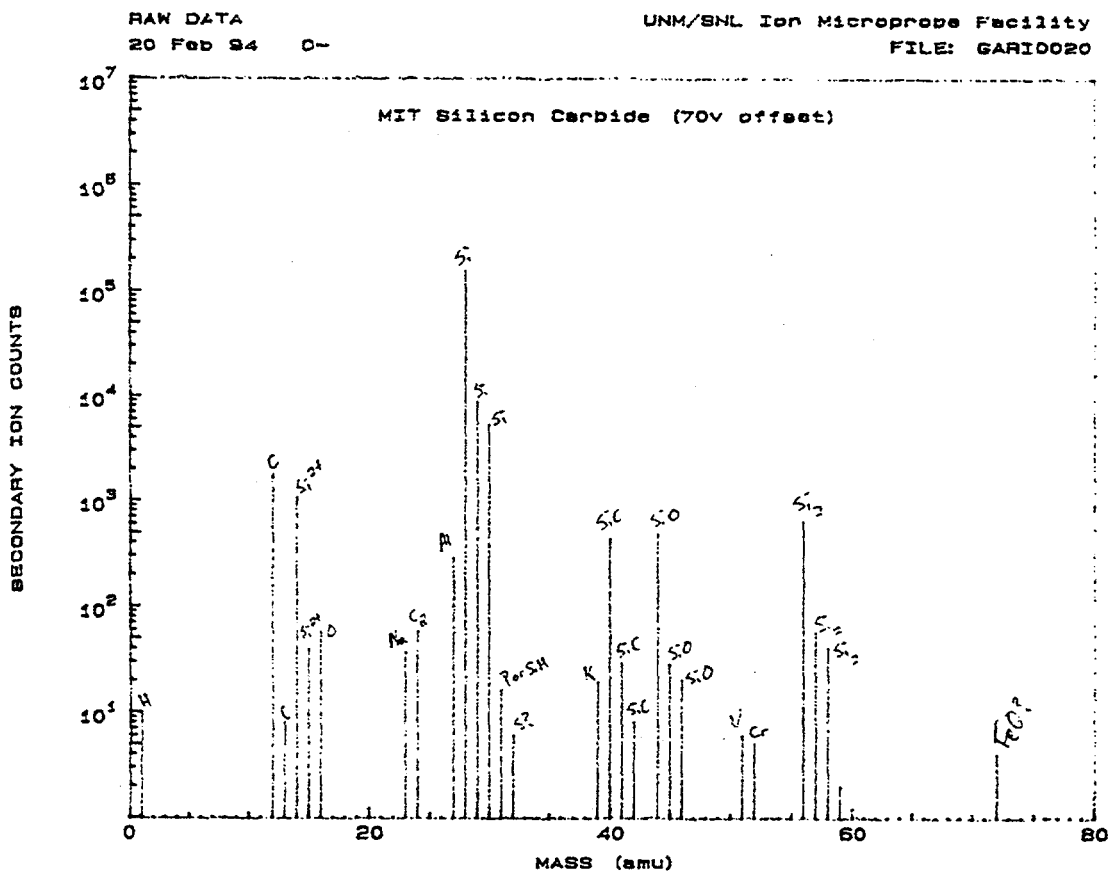

Figure 4.5(a). An impurity analysis of an **MIT SiC** sample using semiquantitative ion microprobe mass spectroscopy (SIMMS).

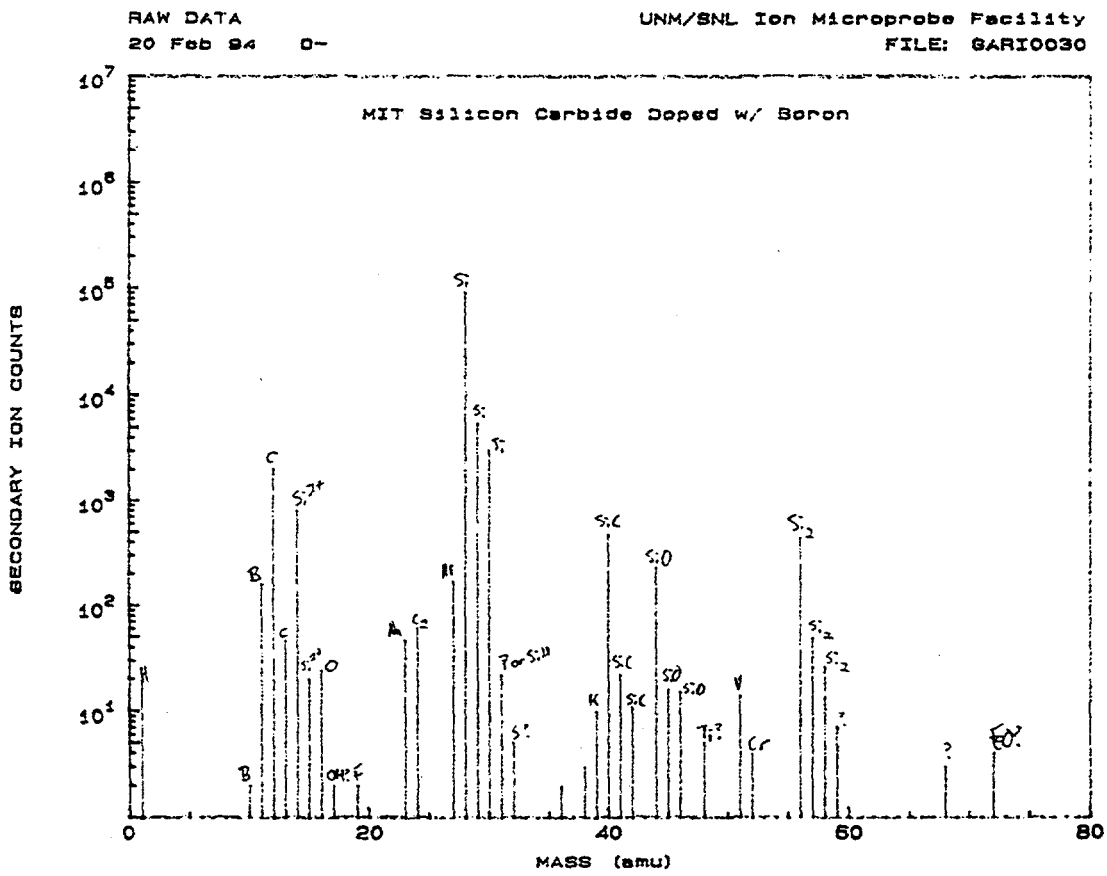

Figure 4.5(b). An impurity analysis of a **boron-doped MIT SiC** sample using semiquantitative ion microprobe mass spectroscopy (SIMMS).

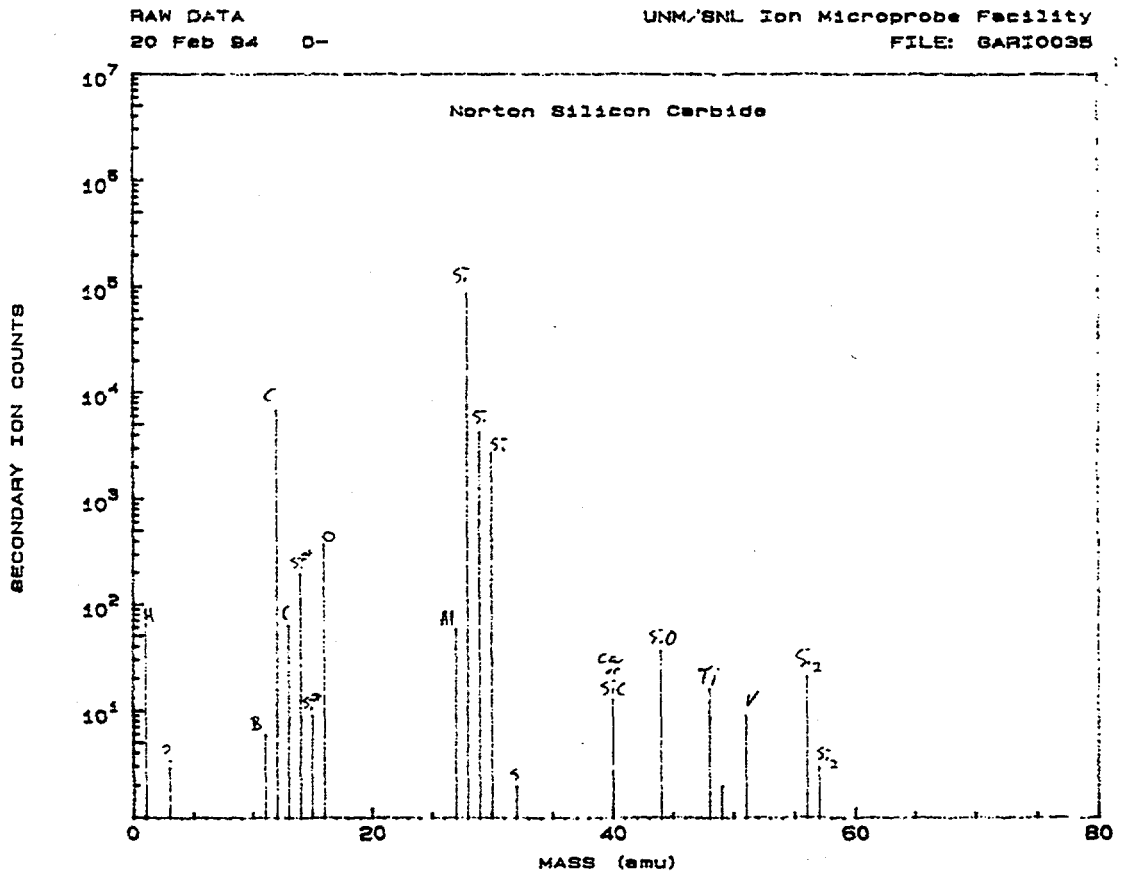

Figure 4.5(c). An impurity analysis of a **Norton SiC** sample using semiquantitative ion microprobe mass spectroscopy (SIMMS).

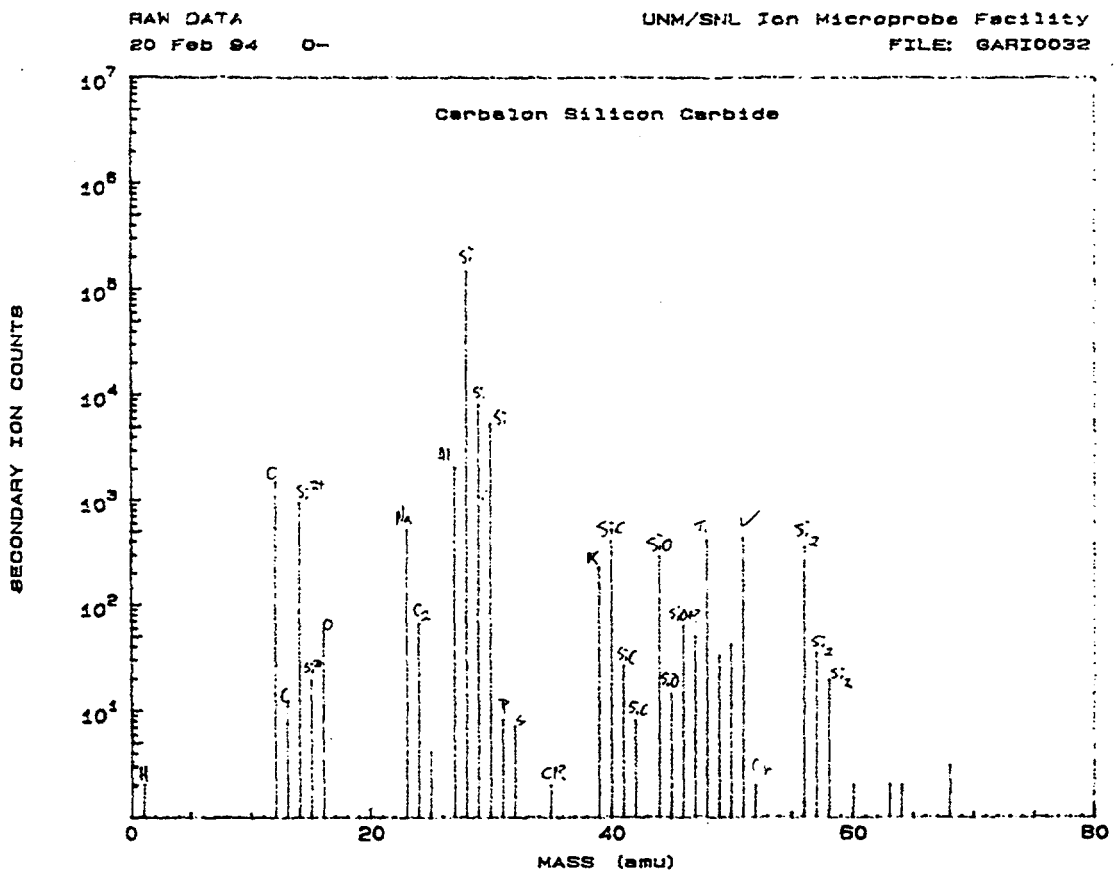

Figure 4.5(d). An impurity analysis of a **Carbolon SiC** sample using semiquantitative ion microprobe mass spectroscopy (SIMMS).

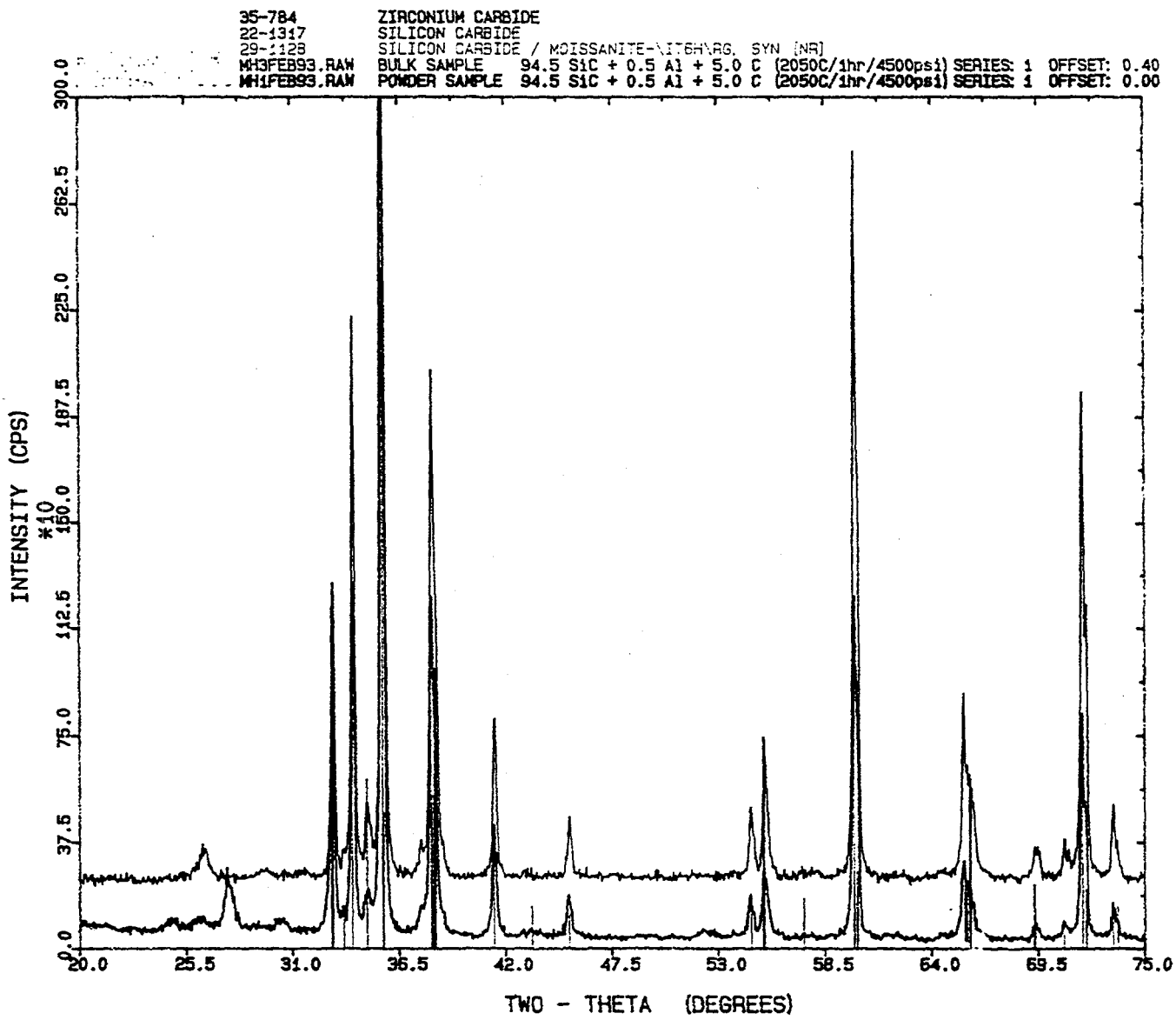

Figure 4.6. X-ray diffraction (XRD) analysis of a hot-pressed **boron-doped SiC** pellete in compare to that of a SiC powder.

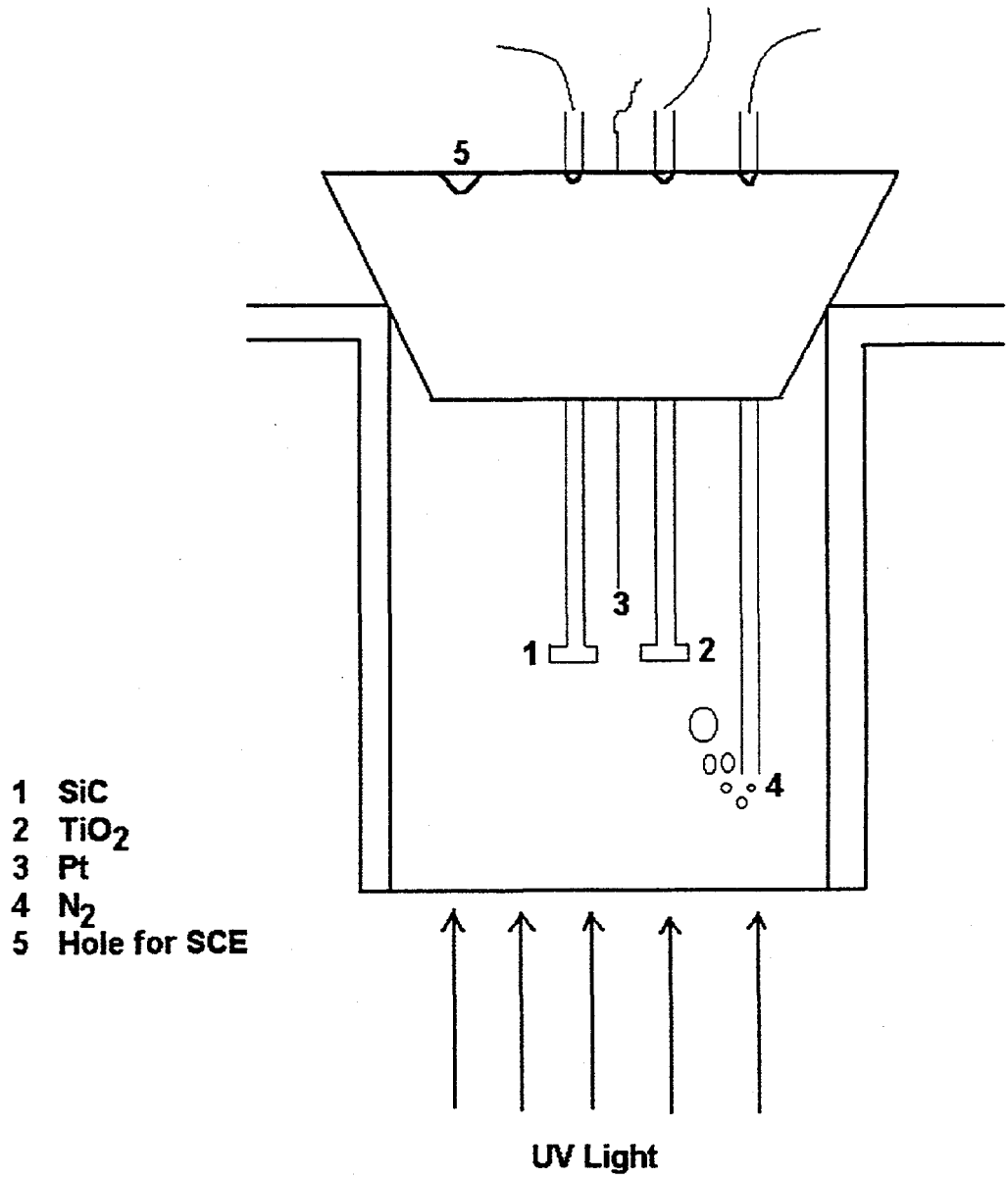

Figure 4.7. A schematic diagram of a photoelectrochemical cell using SiC and TiO_2 as photoelectrodes. A standard calomel electrode (SCE) was used as the reference electrode. The photoelectrodes were illuminated from the bottom of the cell.

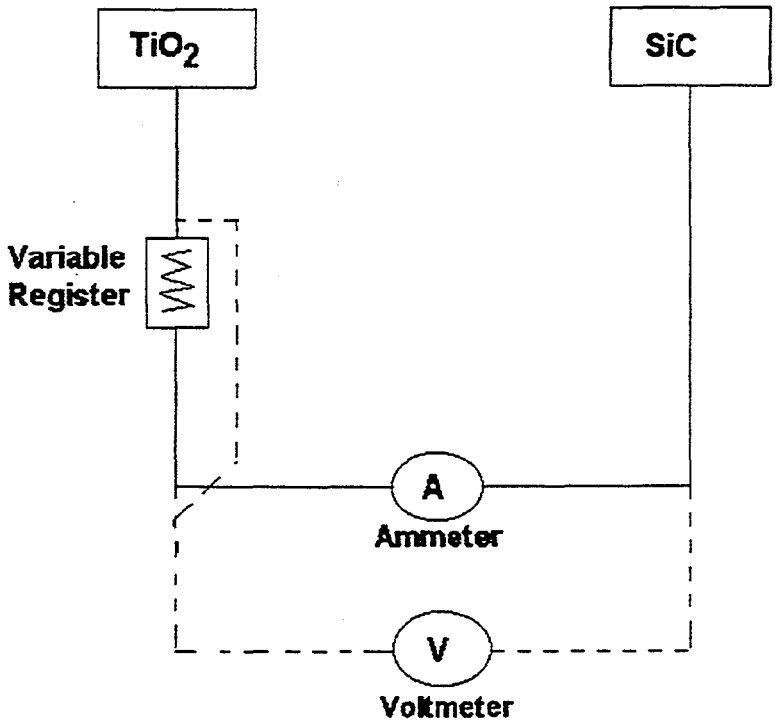

Figure 4.8. A schematic diagram of the setup for measuring photodiode efficiency for TiO_2/SiC diode couple. A variable resistor is connected to an ammeter in series with the electrodes, adjusting the resistance to obtain a series of data.

Etching of SiC with 50% HF for 2 hours Increases its Photoreduction Ability

(0.2% SiC/ 10-mM EDTA/ pH 4.4/ ambient or Ar-purged)

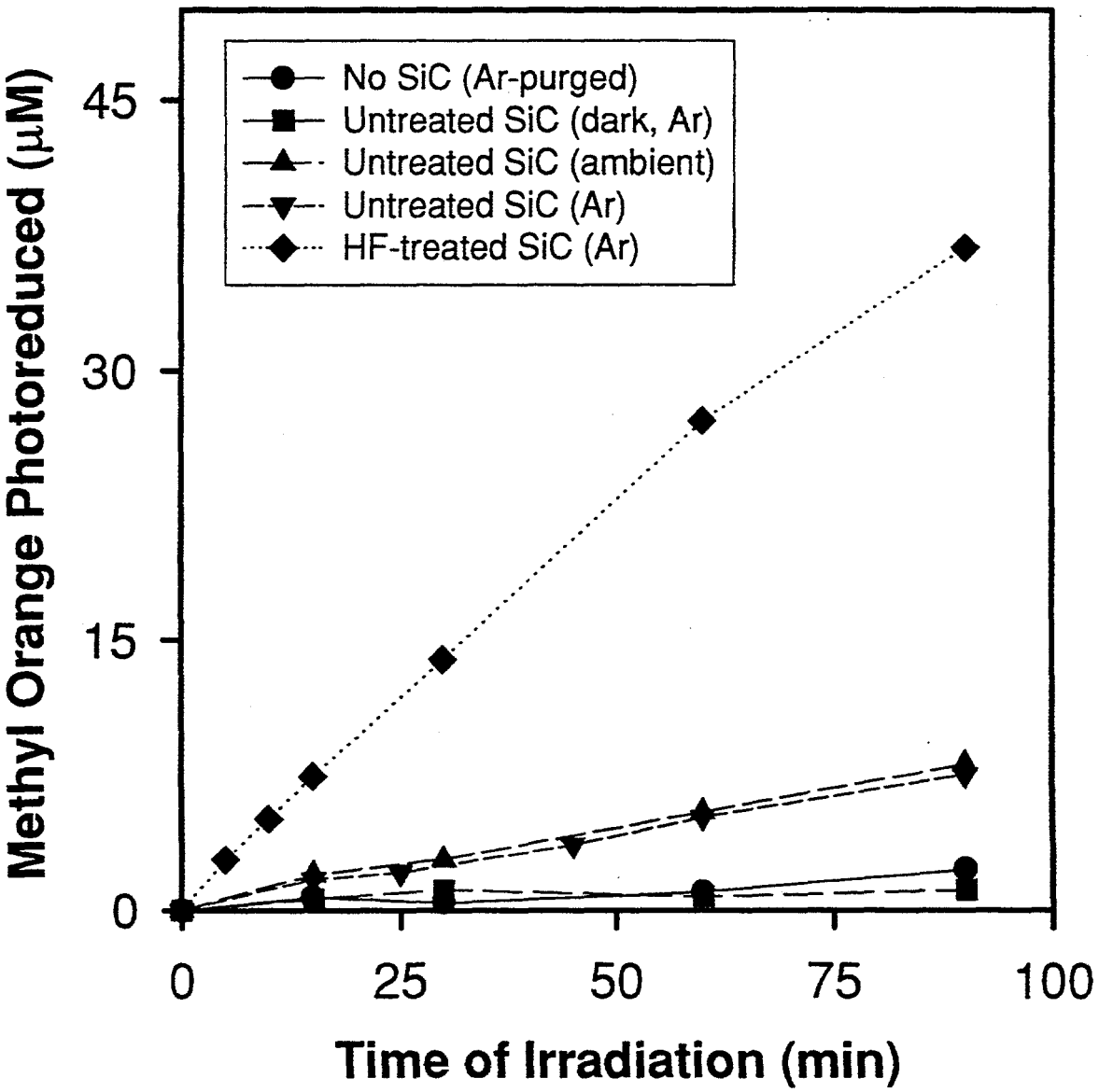

Figure 4.9

sic6.spw

Lowering the pH (<6.5) Increases the Photoreduction Ability of SiC (HF-treated for 2 hours) Significantly

(0.2% SiC/ 10-mM EDTA/ Ar-purged)

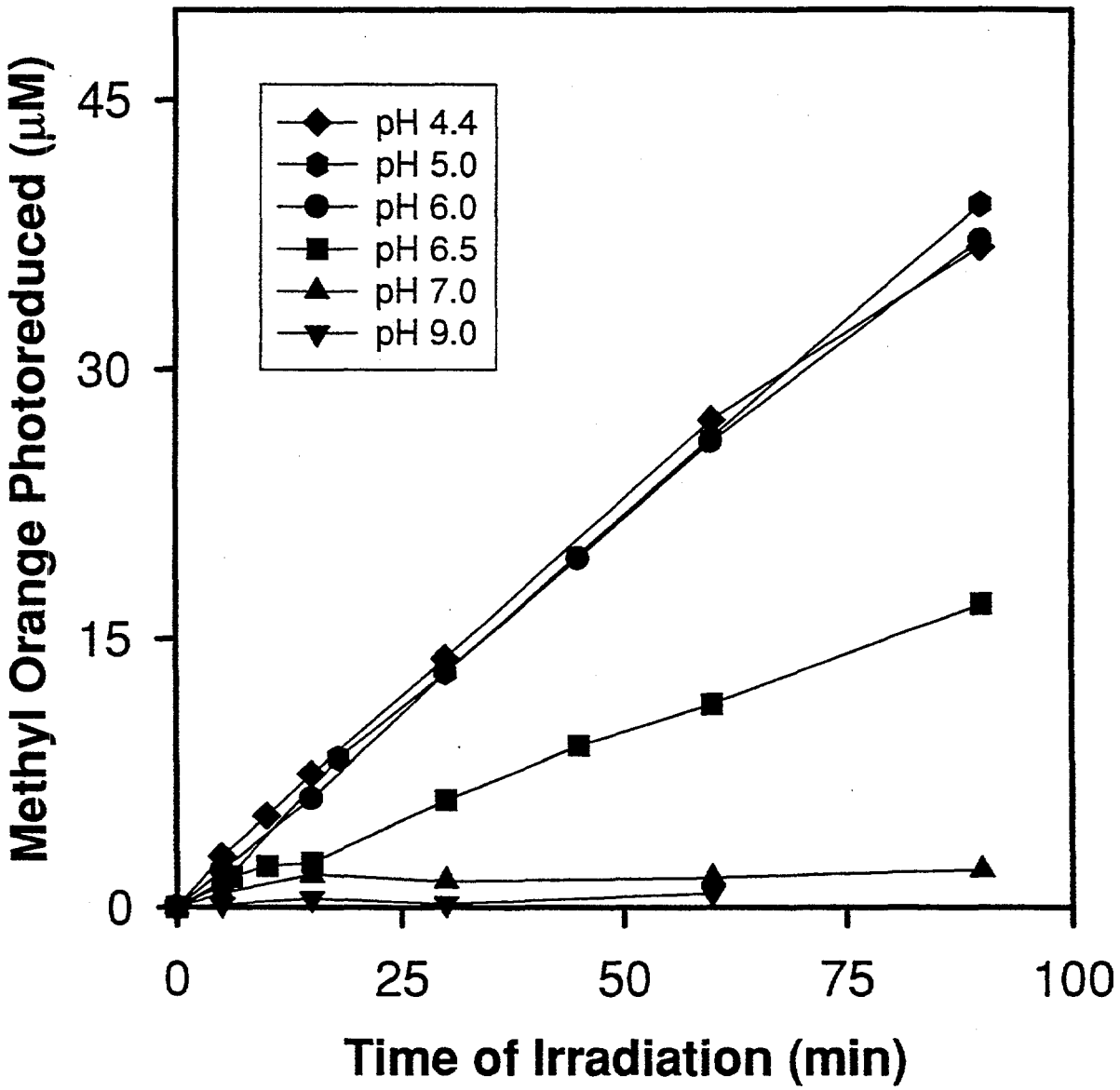

Figure 4.10

sic1.spw

Photoreduction of Methyl Orange (MO) Seems to be Correlated with Adsorption of MO at Different pH

(0.2% SiC/ 10-mM EDTA/ Ar-purged)

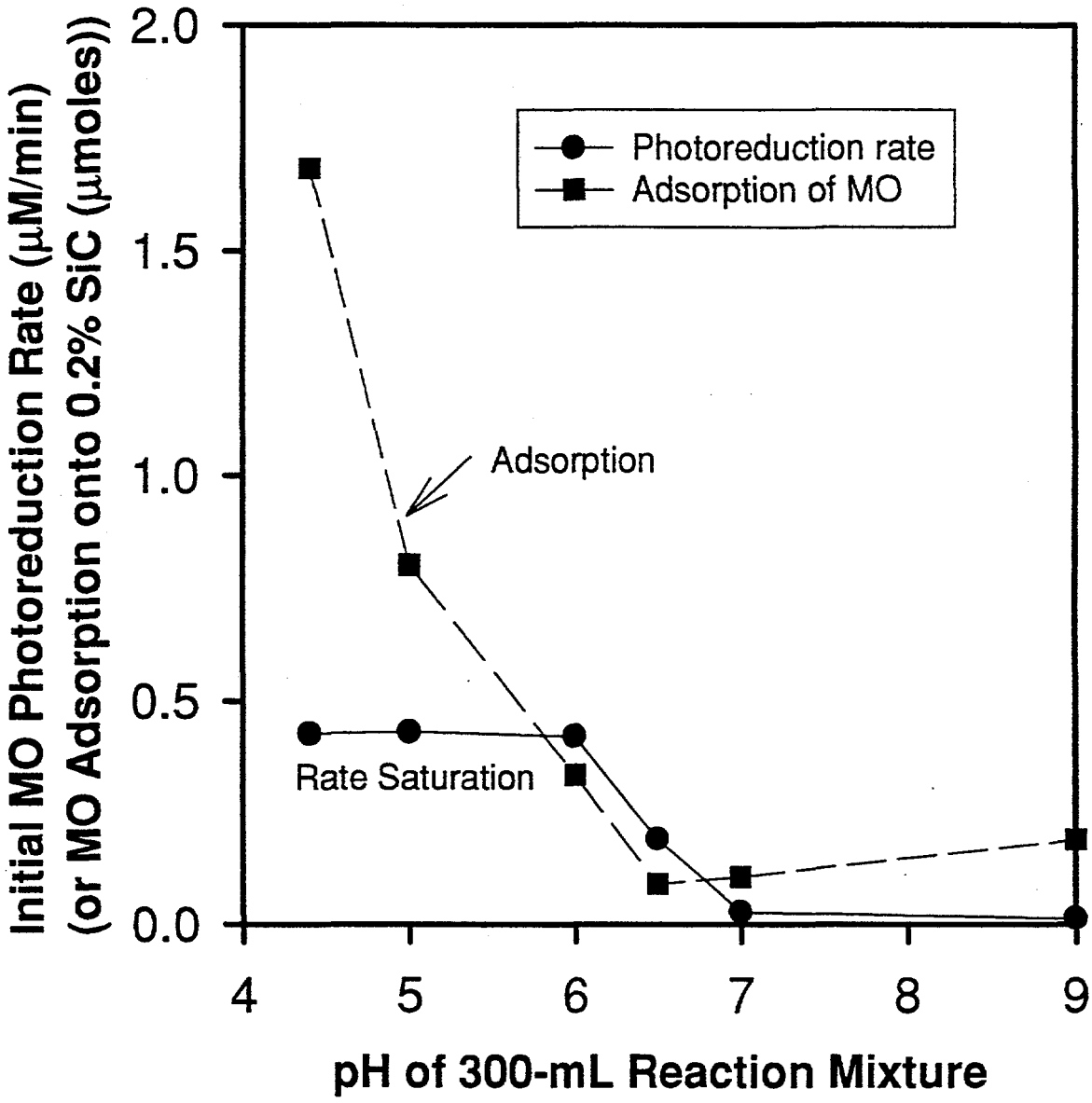

Figure 4.11

sic2.spw

Photoreduction Rate Exhibits 1st Order Kinetics

Dependence on Concentration of Hole Scavenger

(0.2% SiC/ pH 4.4/ Ar-purged)

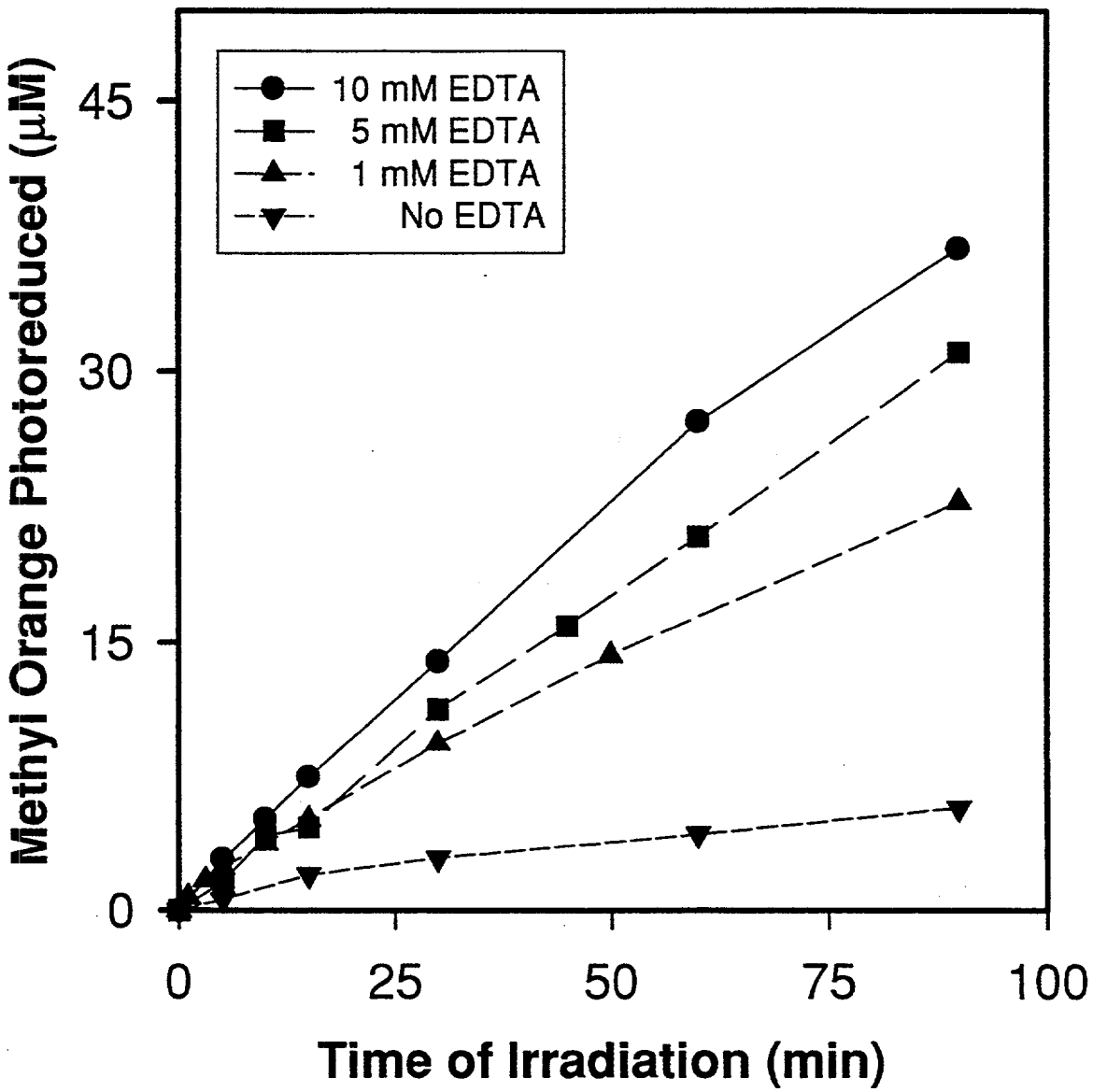

Figure 4.12

sic3.spw

TiO_2 is a much better Photocatalyst than SiC

(10-mM EDTA/ pH 4.4/ Ar-purged)

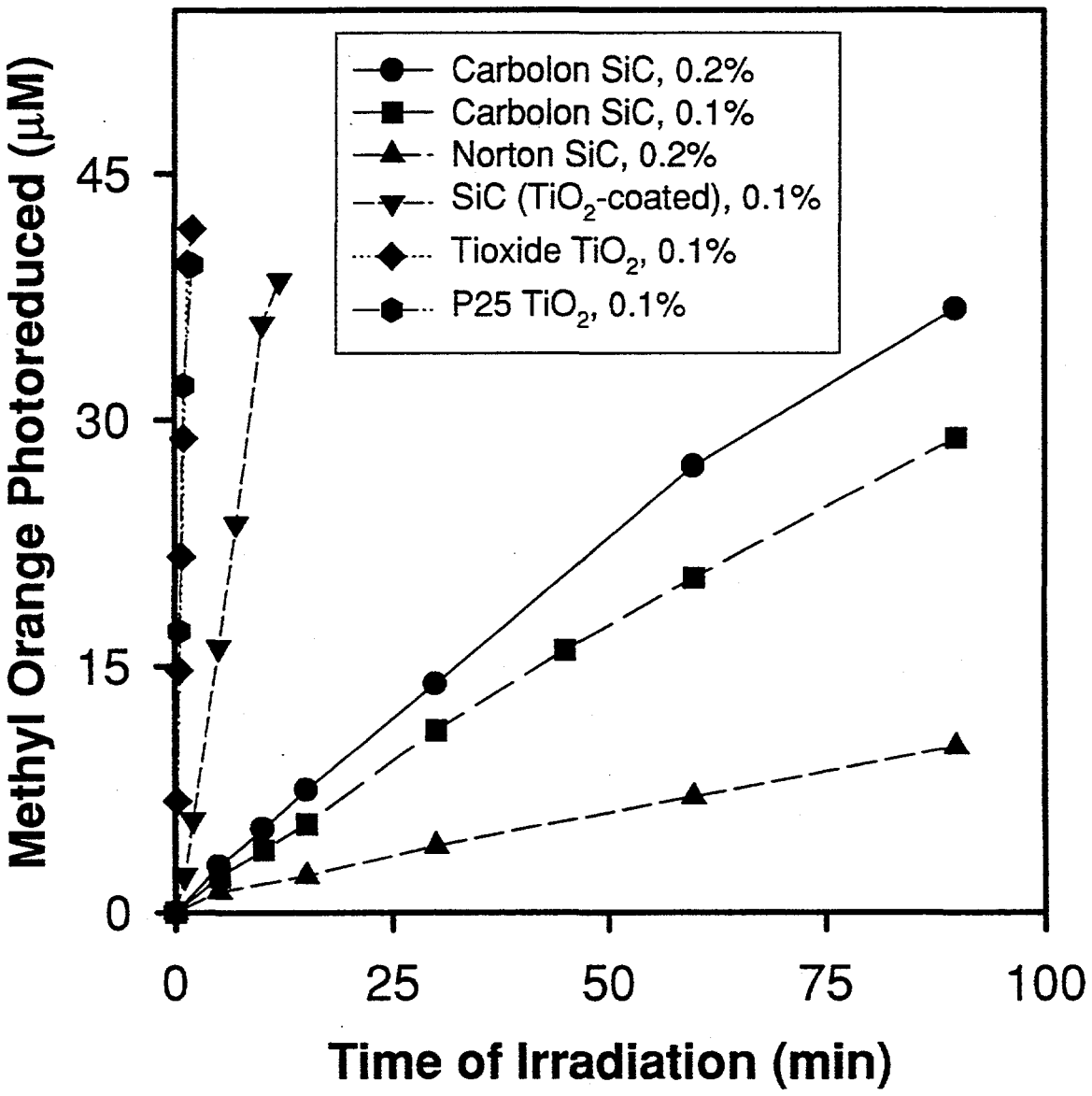

Figure 4.13

sic5.spw

TiO_2 Outperforms SiC for Photoreduction of Cr^{+6}

Lower pH Enhances the Photoreduction Rate

(1-mM EDTA/ Ar-purged)

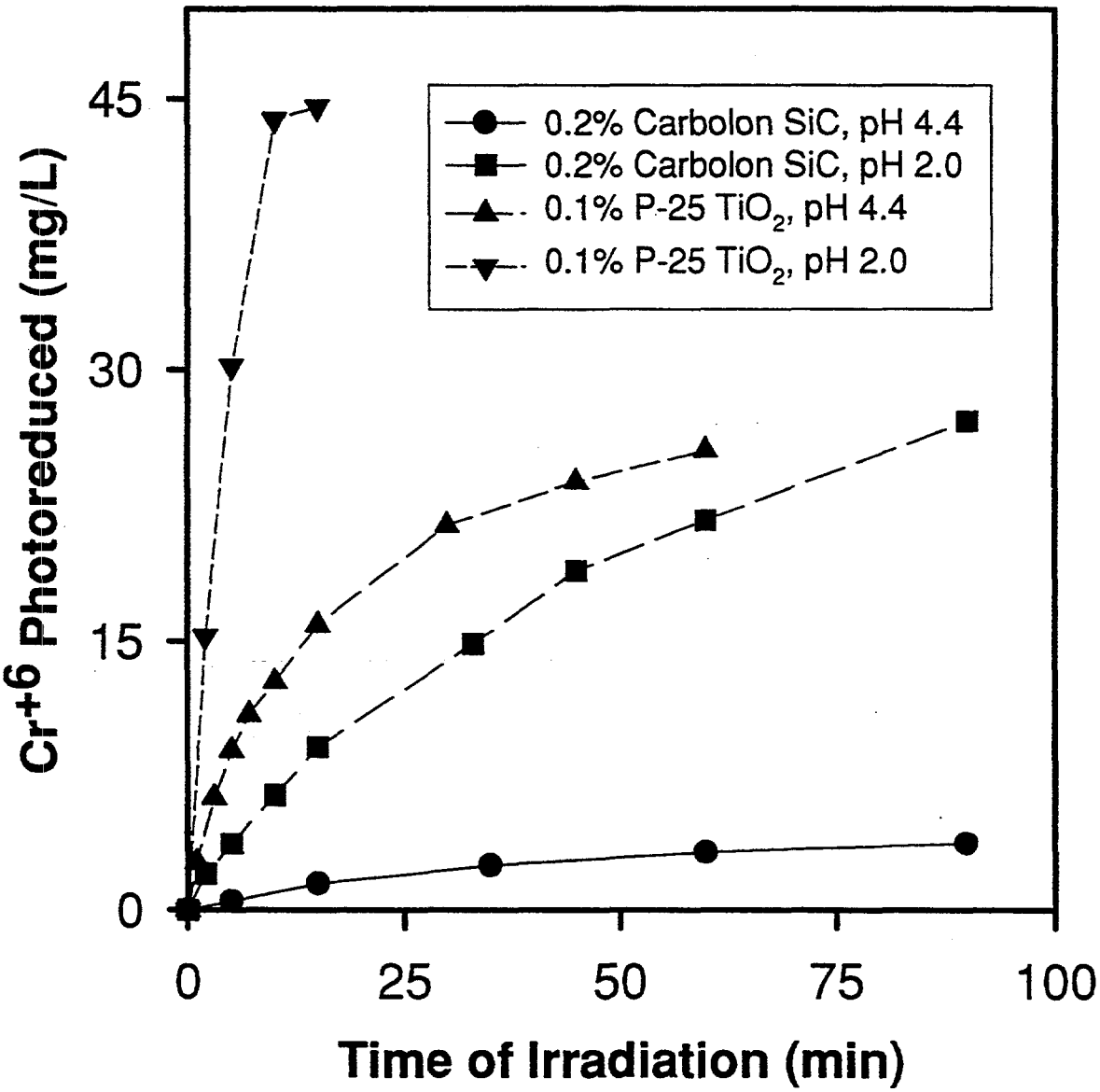

Figure 4.14

sic7.spw

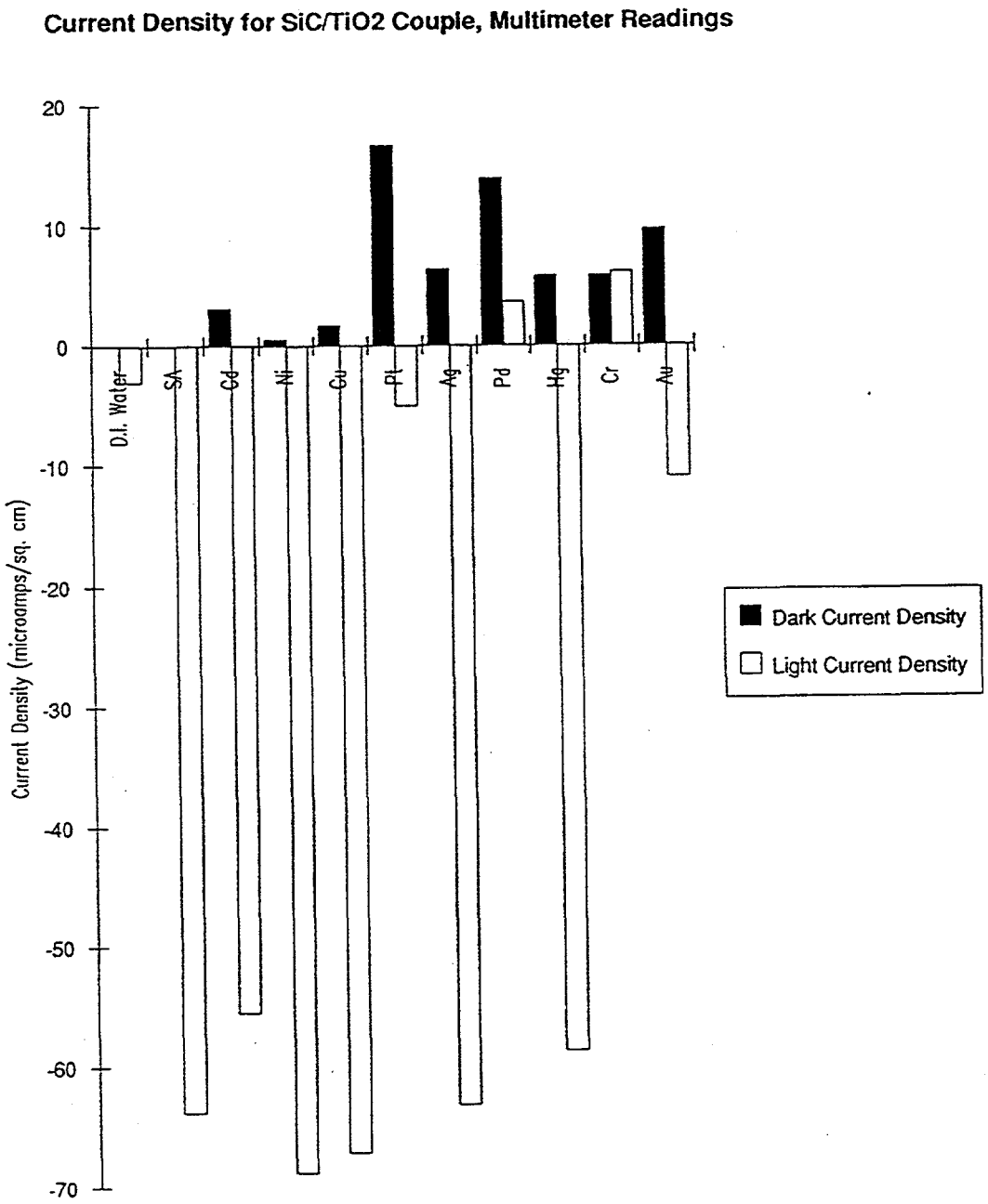

Figure 4.15. Observed current density under both dark and illumination conditions for SiC/TiO_2 photodiodes using a multimeter. The metal (or deionized water only) that is used for a specific reaction system is indicated.

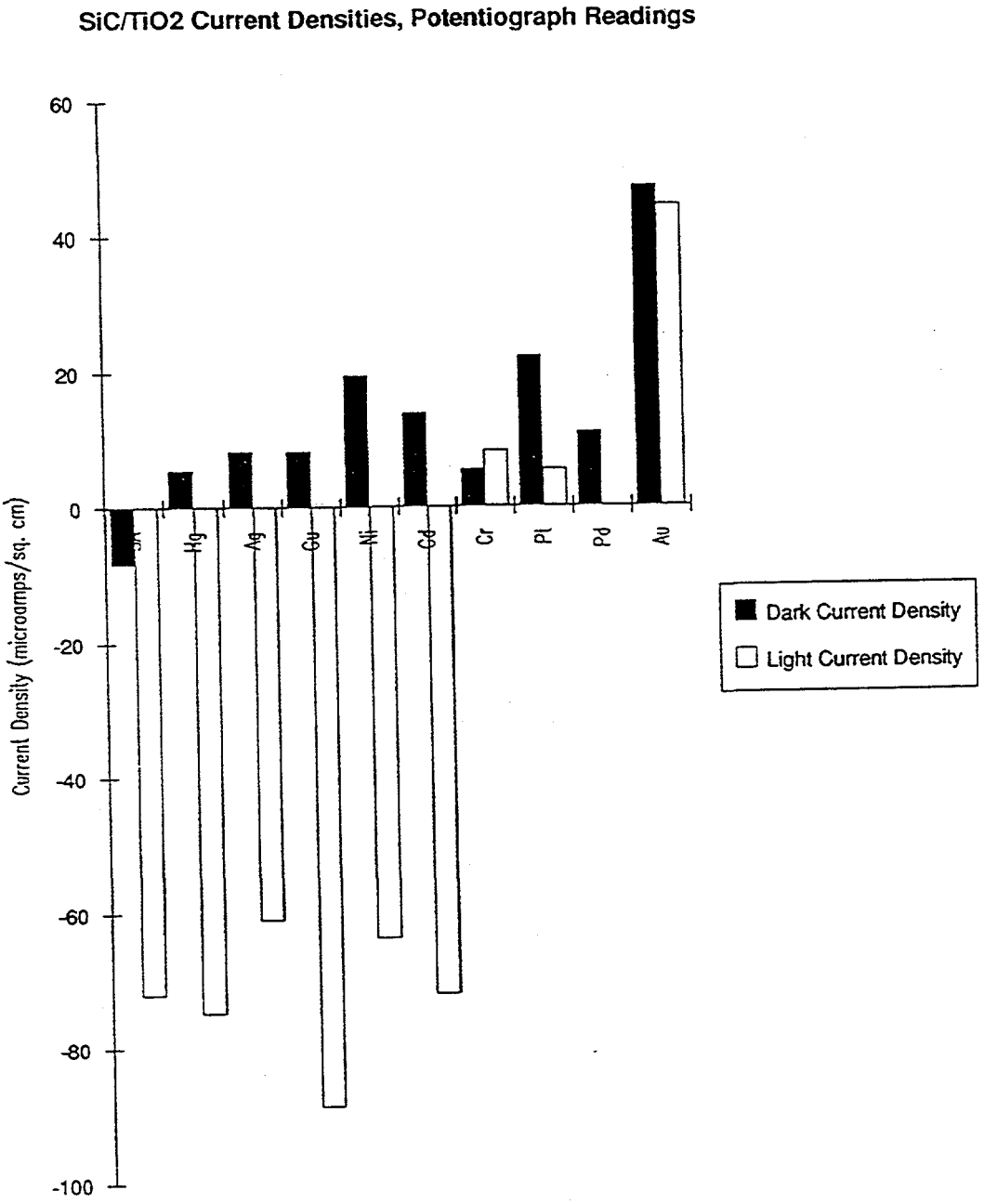

Figure 4.16. Observed current density under both dark and illumination conditions for SiC/TiO_2 photodiodes using a potentiostat. The metal that is used for a specific reaction system is indicated.

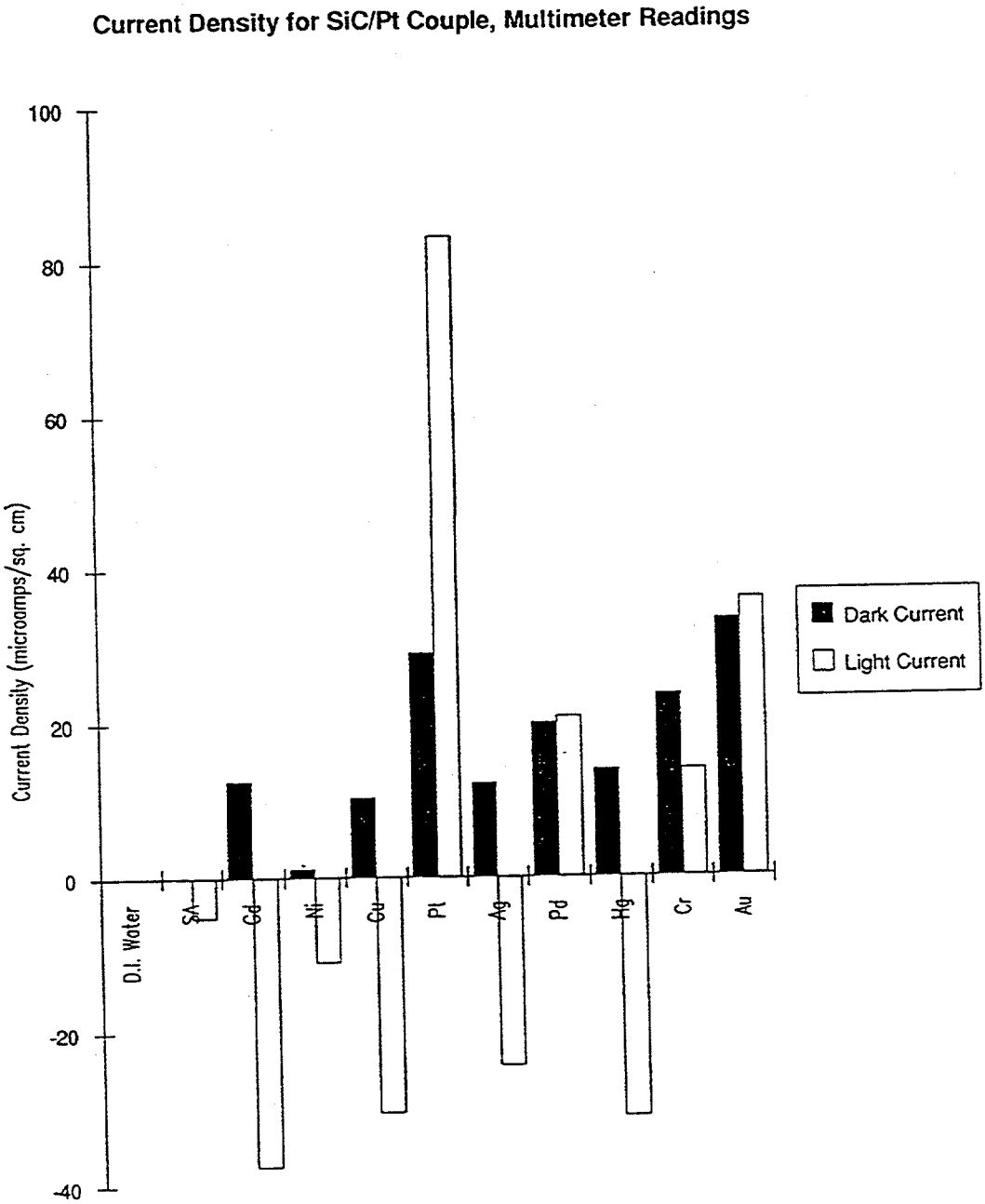

Figure 4.17. Observed current density under both dark and illumination conditions for SiC/Pt couples using a multimeter. The metal (or deionized water only) that is used for a specific reaction system is indicated.

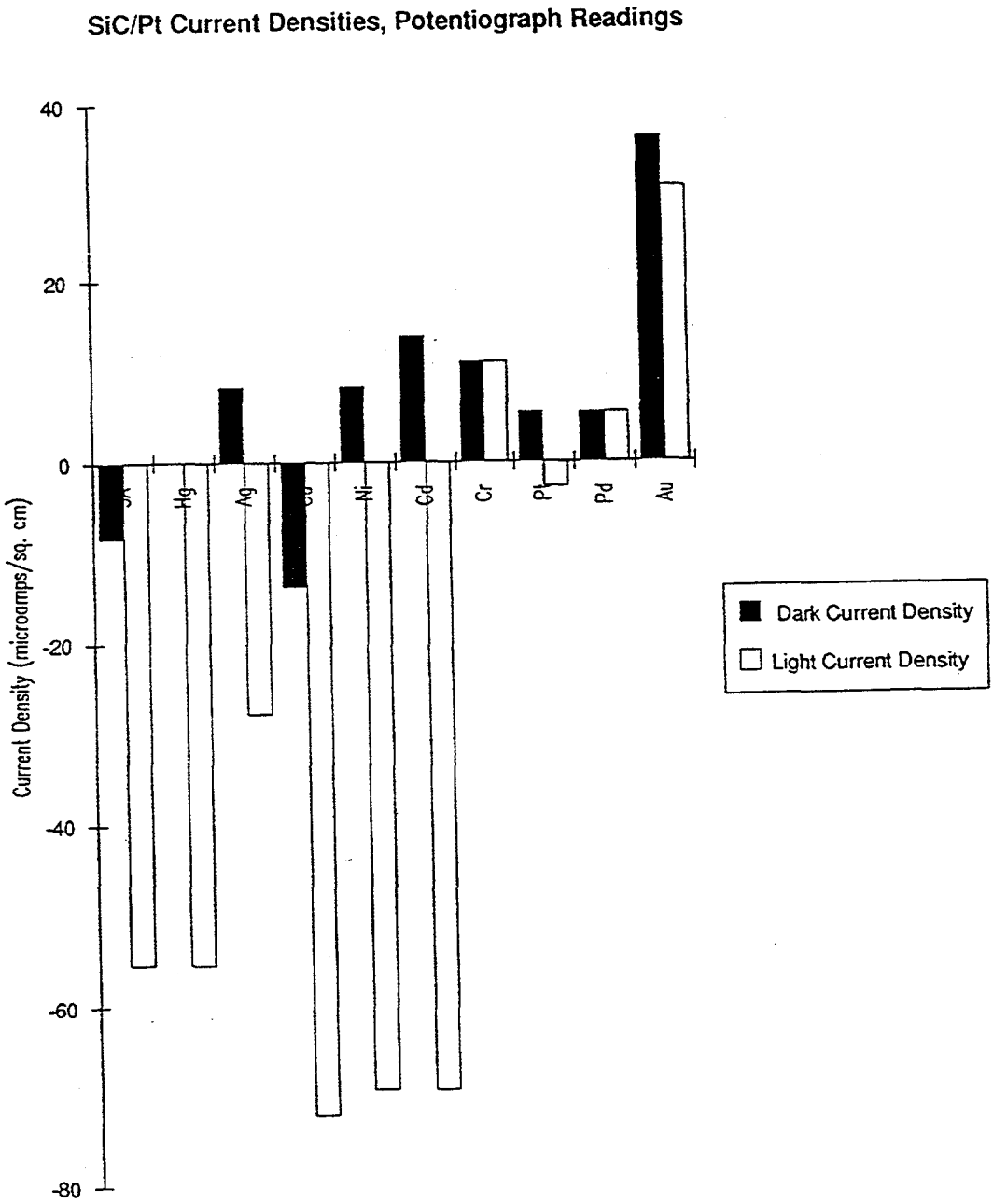

Figure 4.18. Observed current density under both dark and illumination conditions for SiC/Pt couples using a potentiostat. The metal that is used for a specific reaction system is indicated.

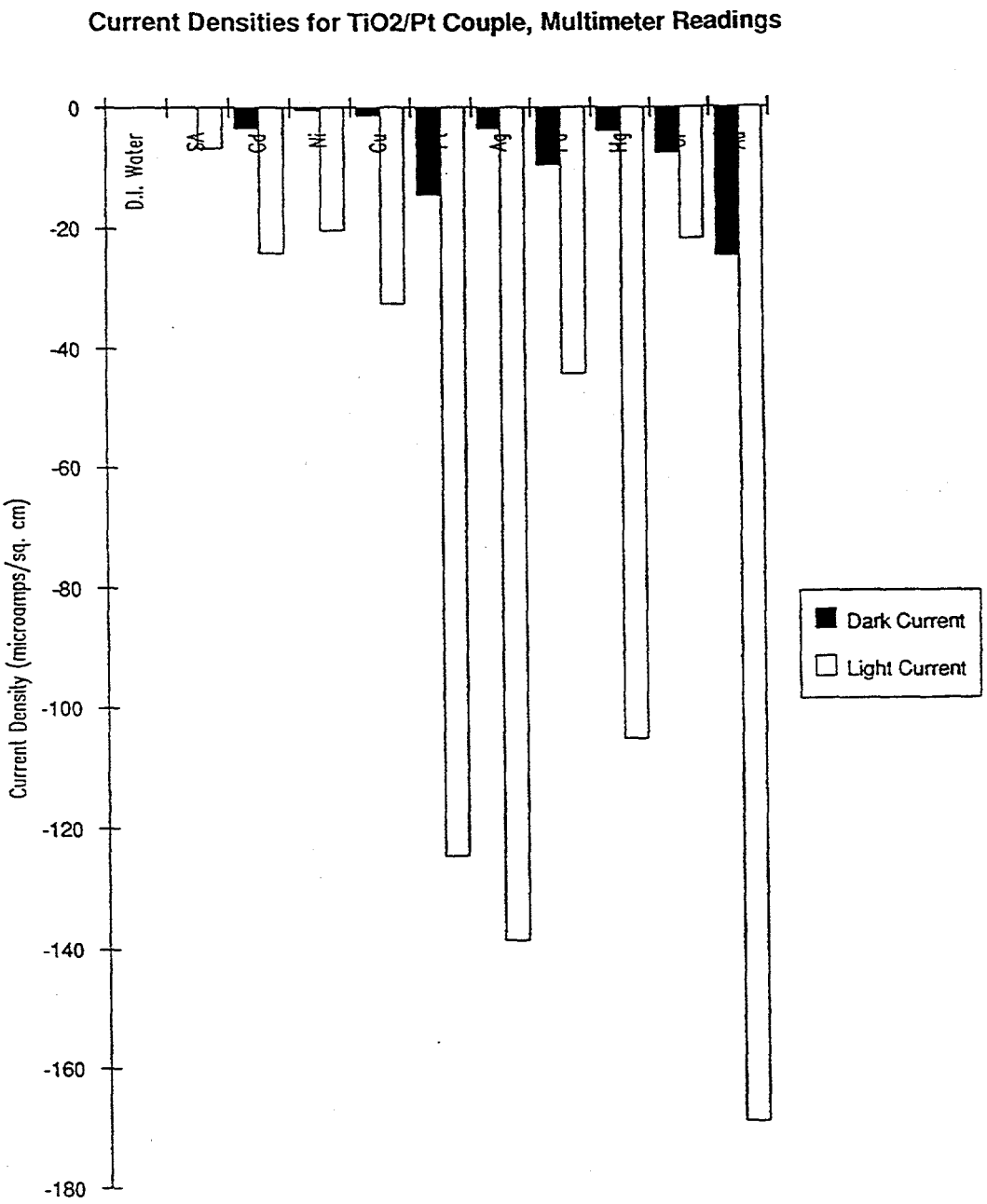

Figure 4.19. Observed current density under both dark and illumination conditions for TiO_2/Pt couples using a multimeter. The metal (or deionized water only) that is used for a specific reaction system is indicated.

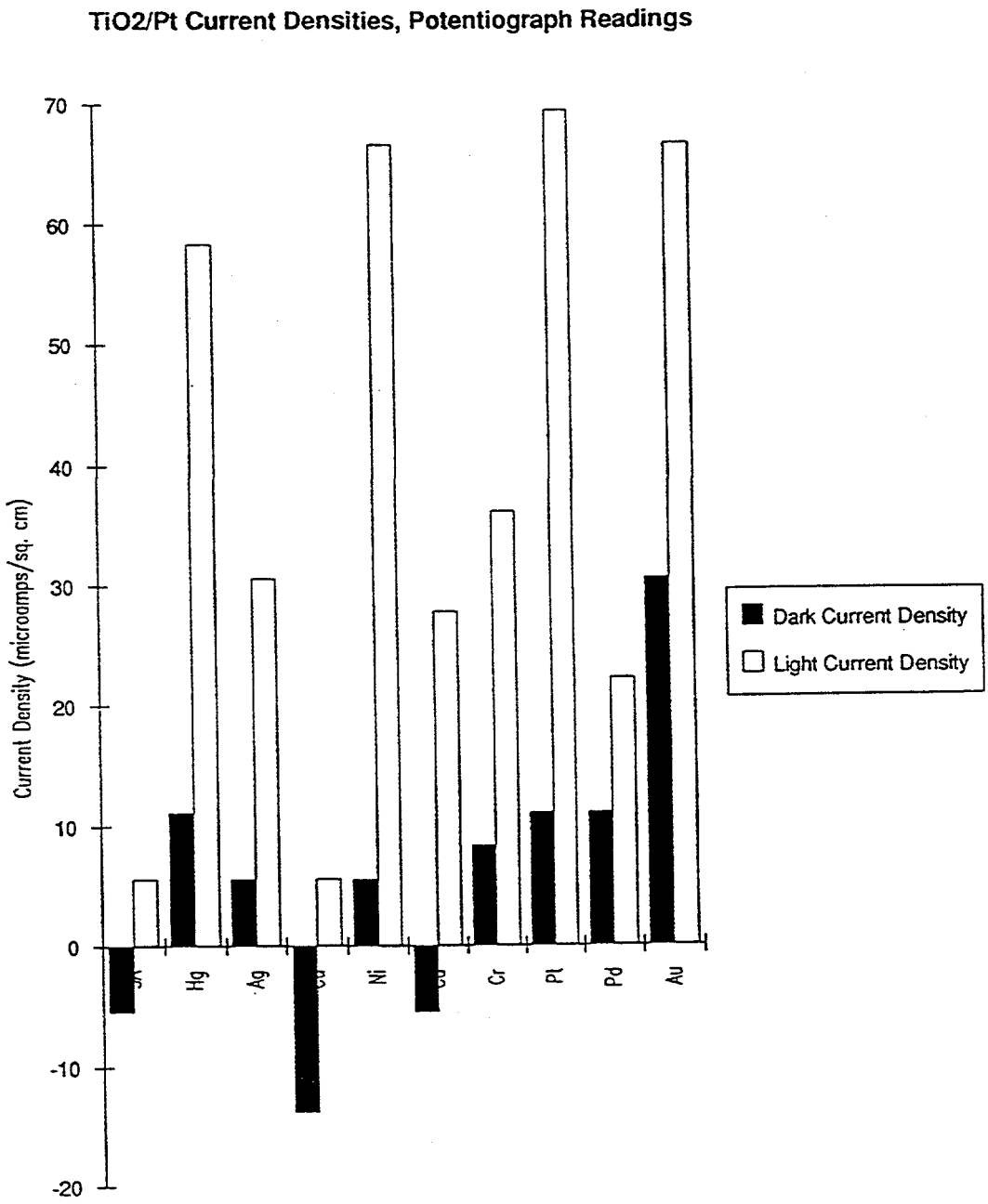

Figure 4.20. Observed current density under both dark and illumination conditions for TiO_2/Pt couples using a potentiostat. The metal that is used for a specific reaction system is indicated.

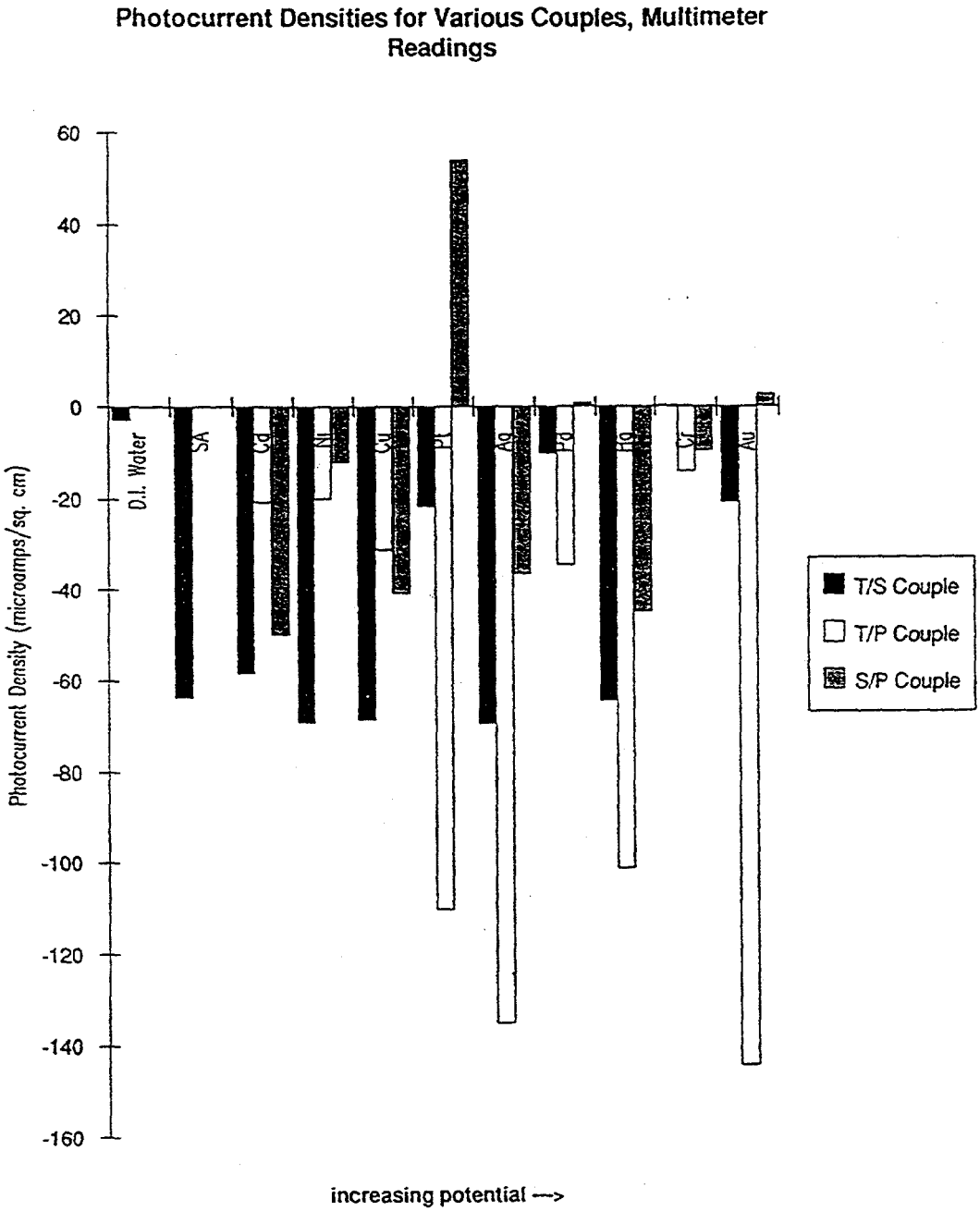

Figure 4.21. Observed photocurrent density for various couples using a multimeter. Photocurrent responses are shown in black, white, and gray for the couples TiO_2/SiC (T/S), TiO_2/Pt (T/P), and SiC/Pt (S/P), respectively. The metal (or deionized water only) that is used for a specific reaction system is indicated.

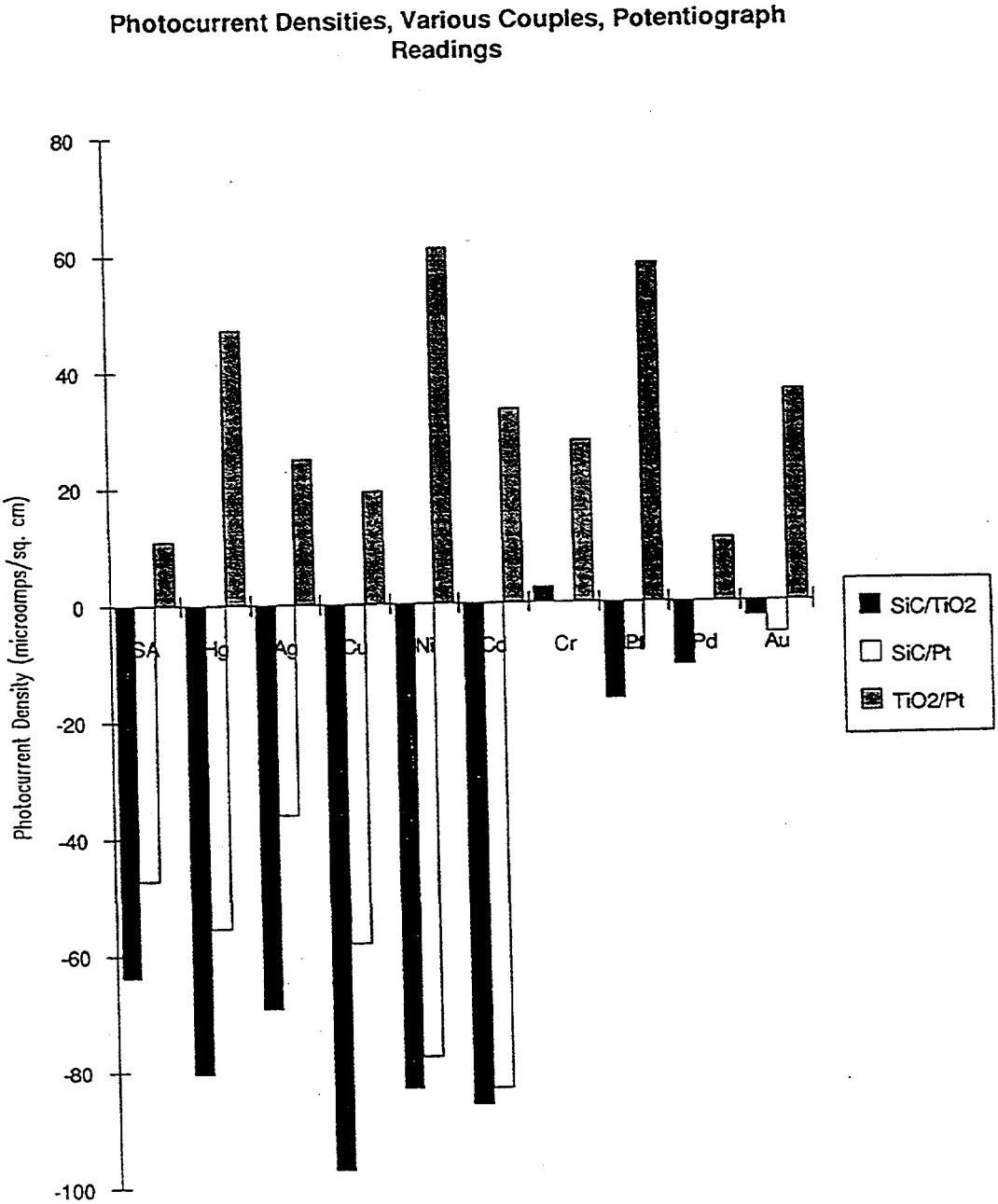

Figure 4.22. Observed photocurrent density for various couples using a potentiostat. Photocurrent responses are shown in black, white, and gray for the couples SiC/TiO_2, SiC/Pt, and TiO_2/Pt, respectively. The metal that is used for a specific reaction system is indicated.

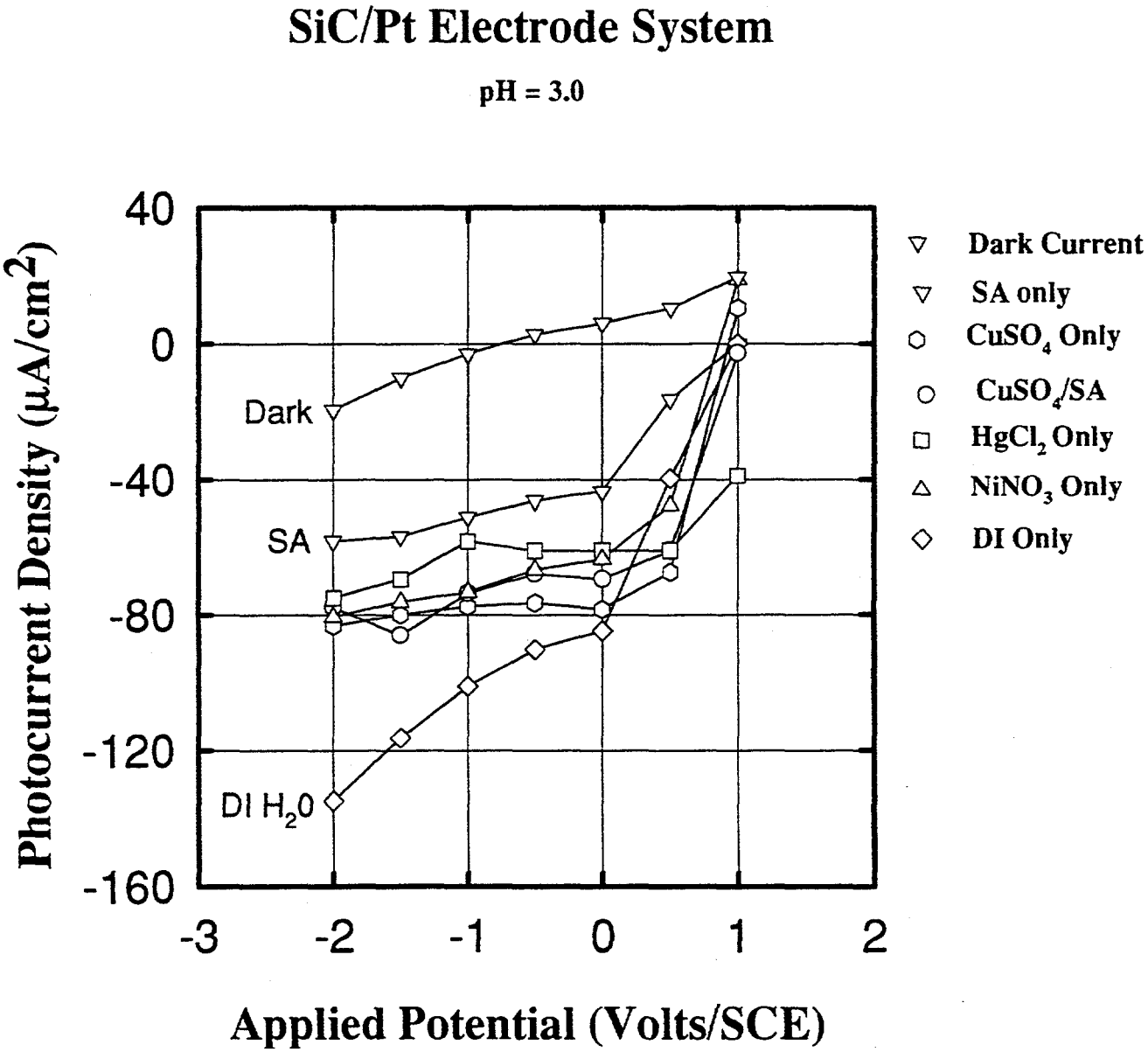

Figure 4.23

gail3.spw

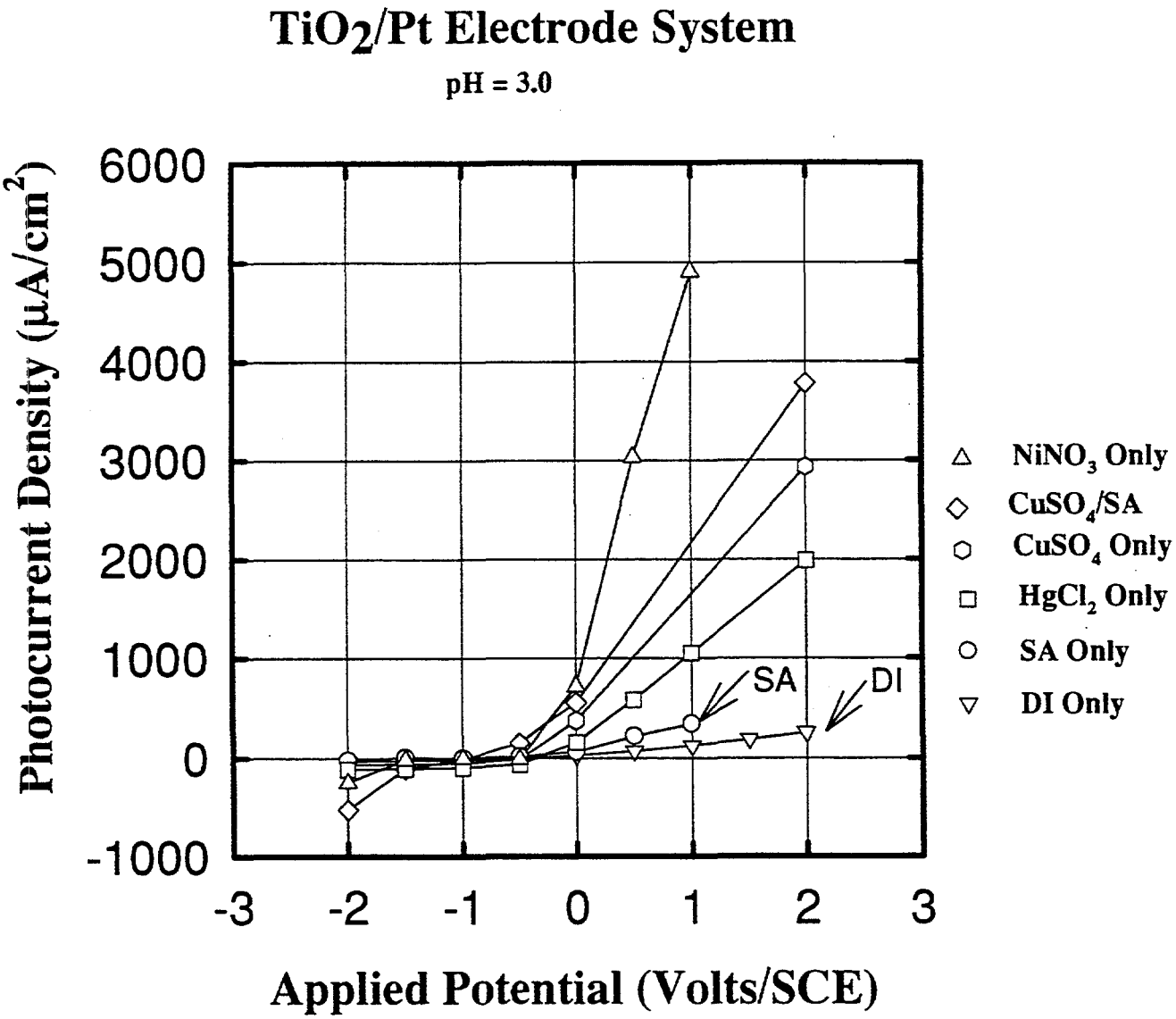

Figure 4.24

gail2.spw

TiO_2/SiC Electrode System

Overcurrent Voltage = 1.08, 1.3, .97, 1.2, 1.08, 1.04, 1.03, 1.2, 1.1 V

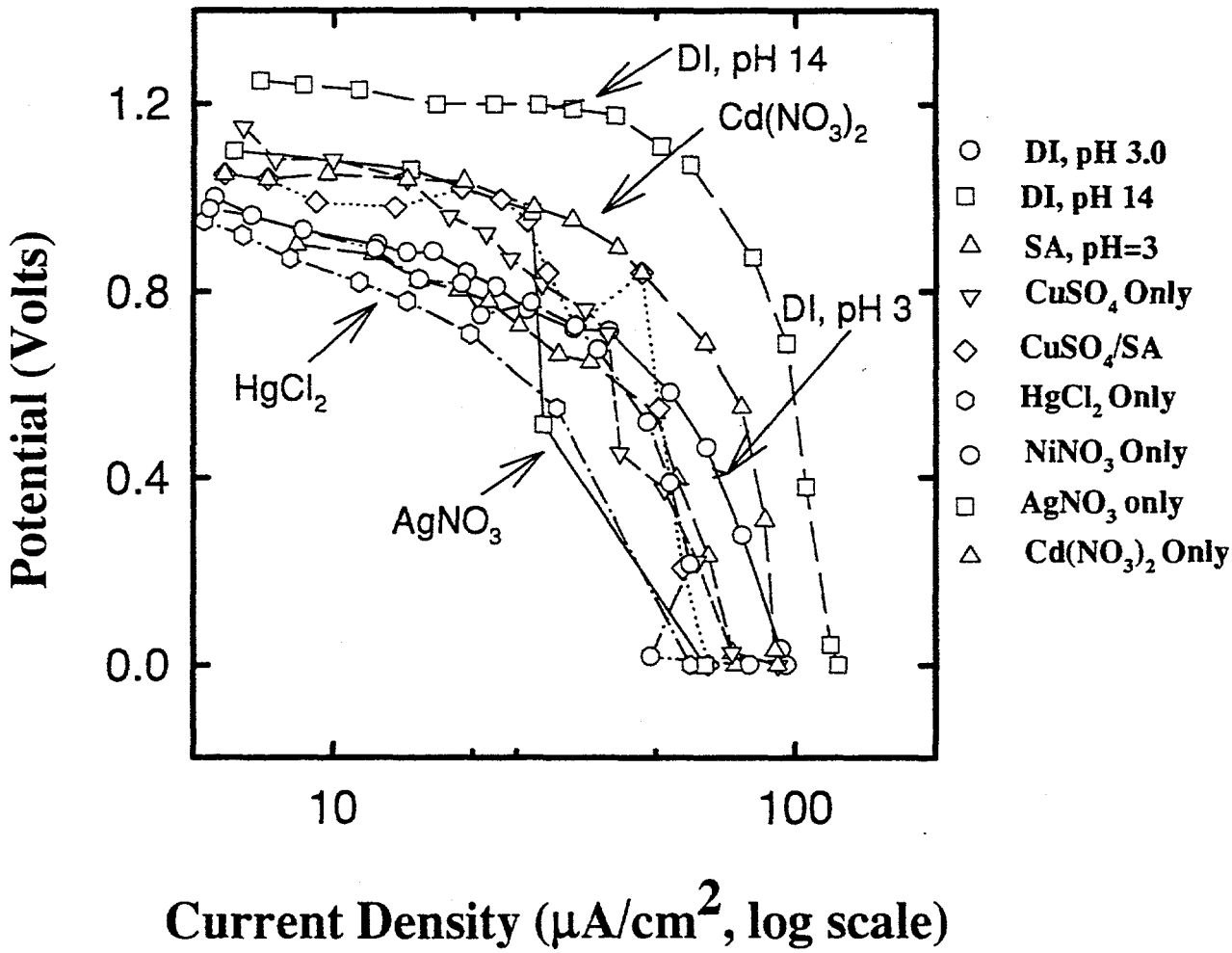

Figure 4.25

gail1.spw

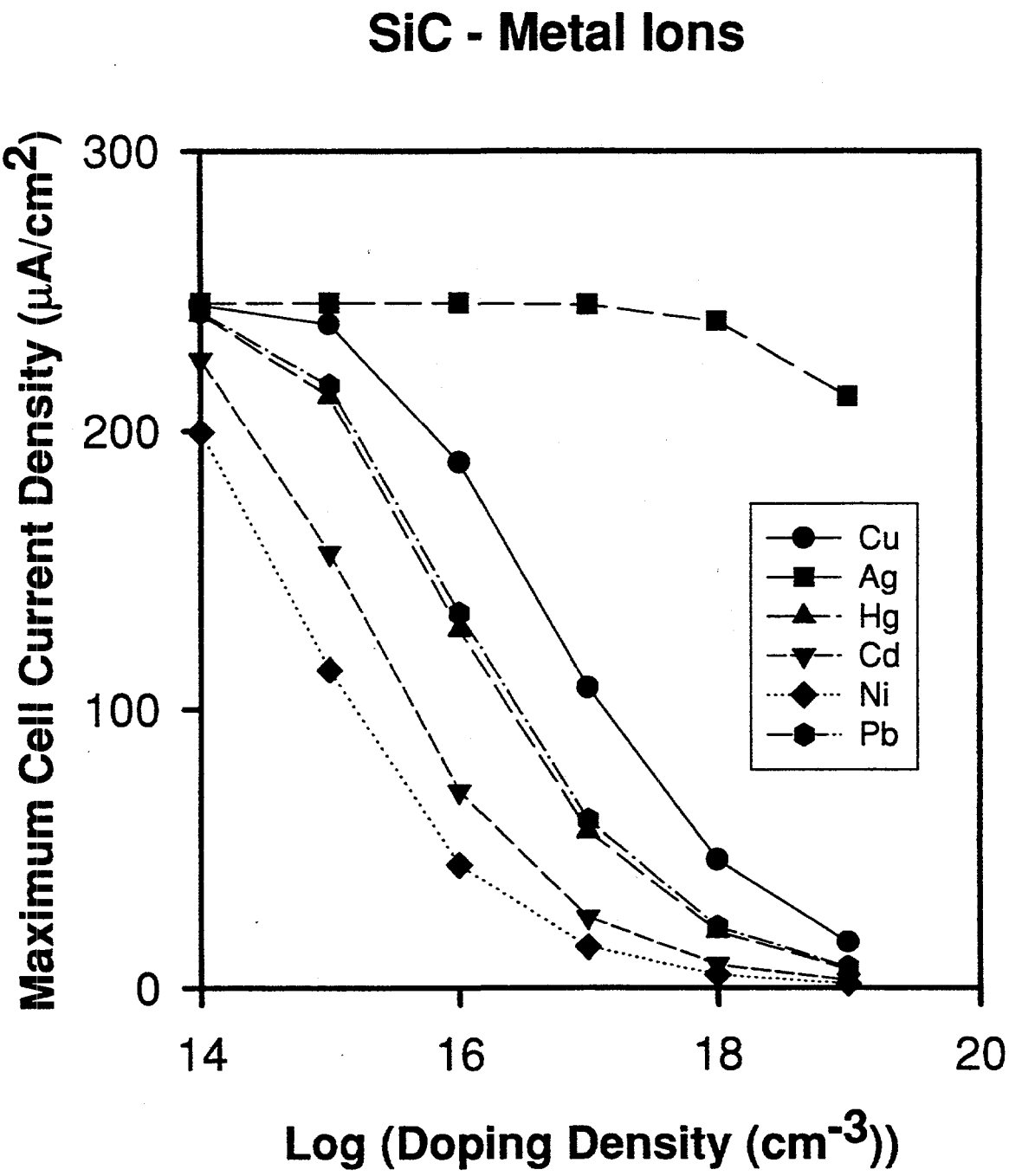

Figure 4.26(a)

khan2a.spw

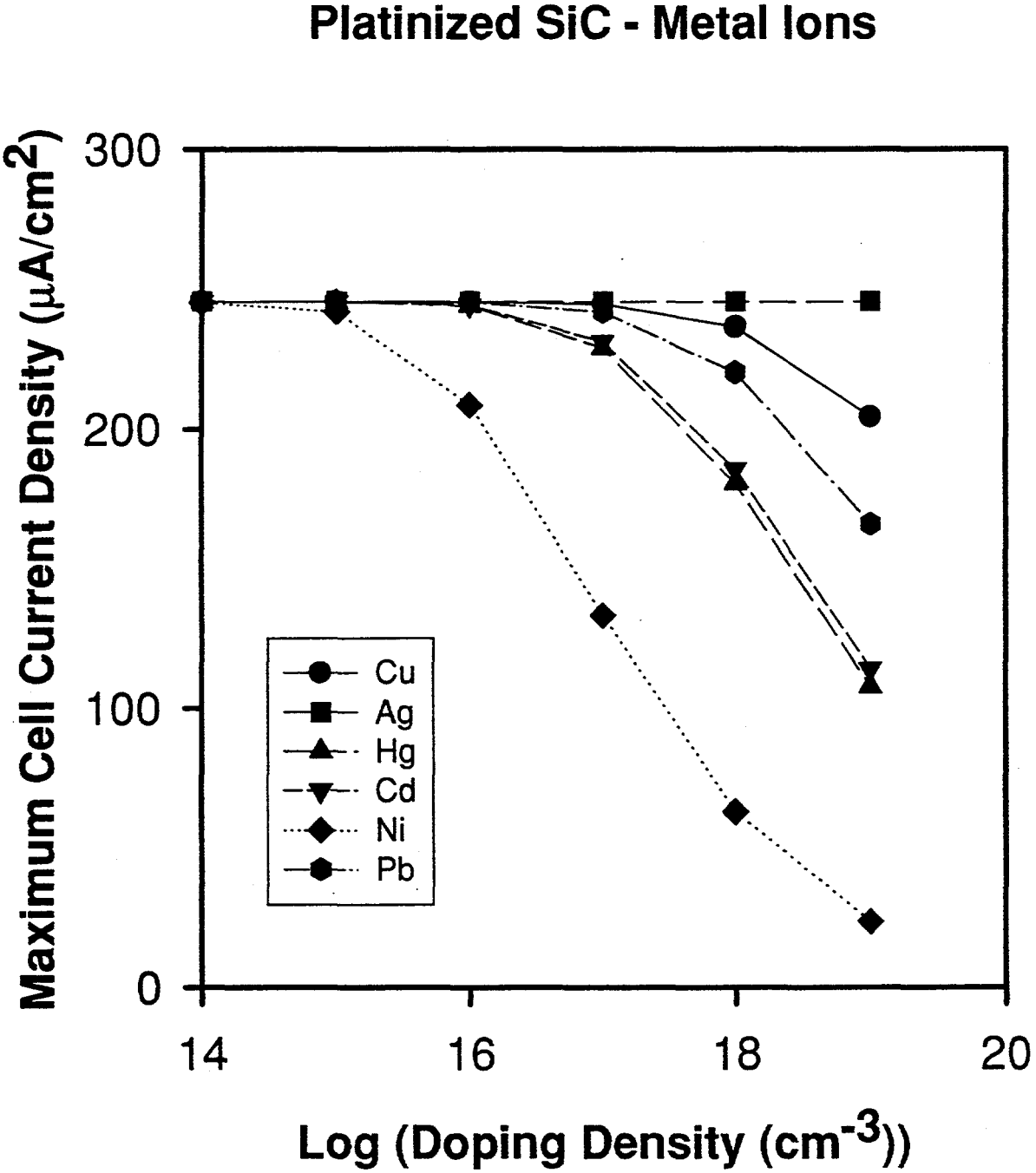

Figure 4.26(b)

khan2b

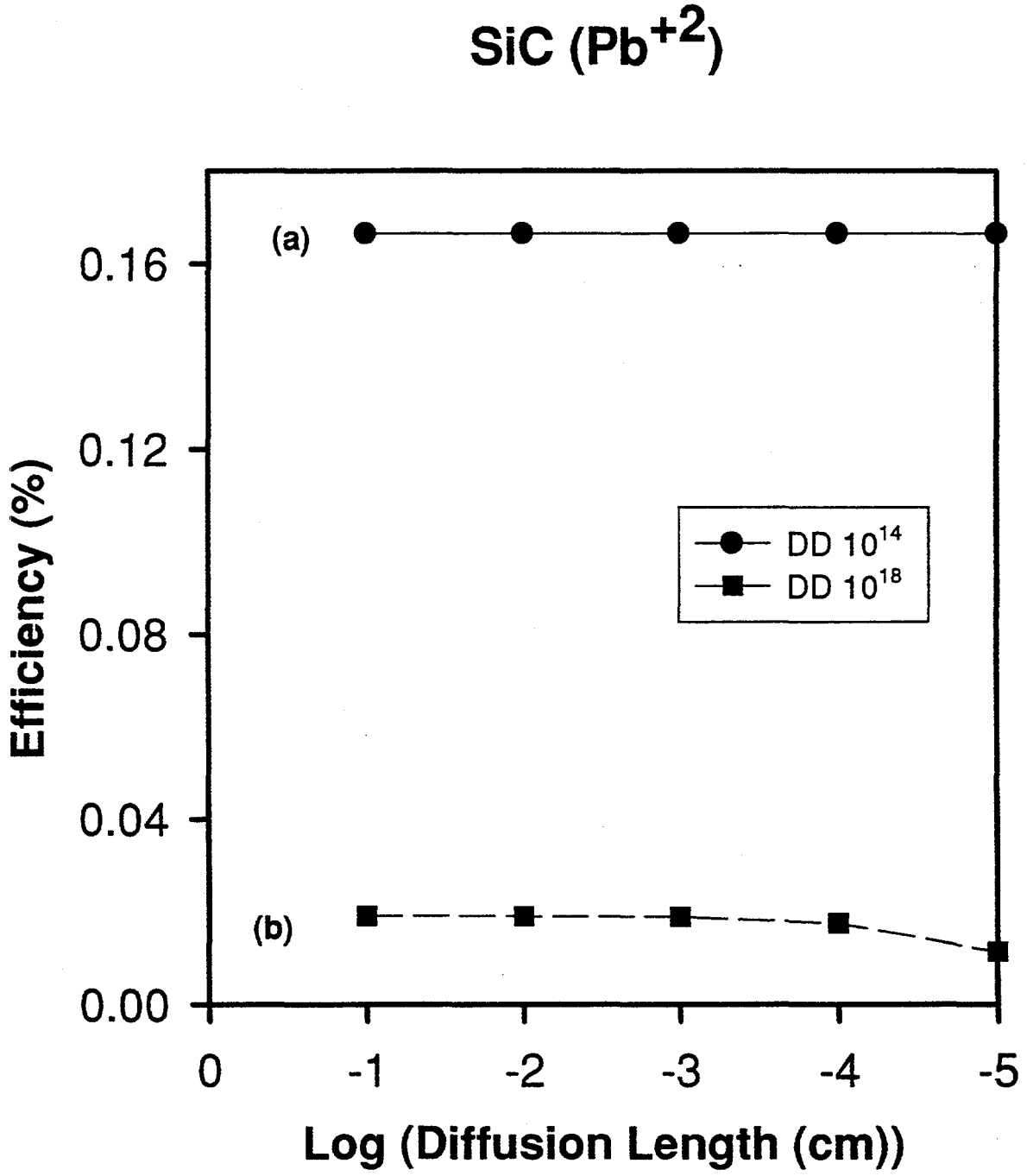

Figure 4.27

khan3.spw

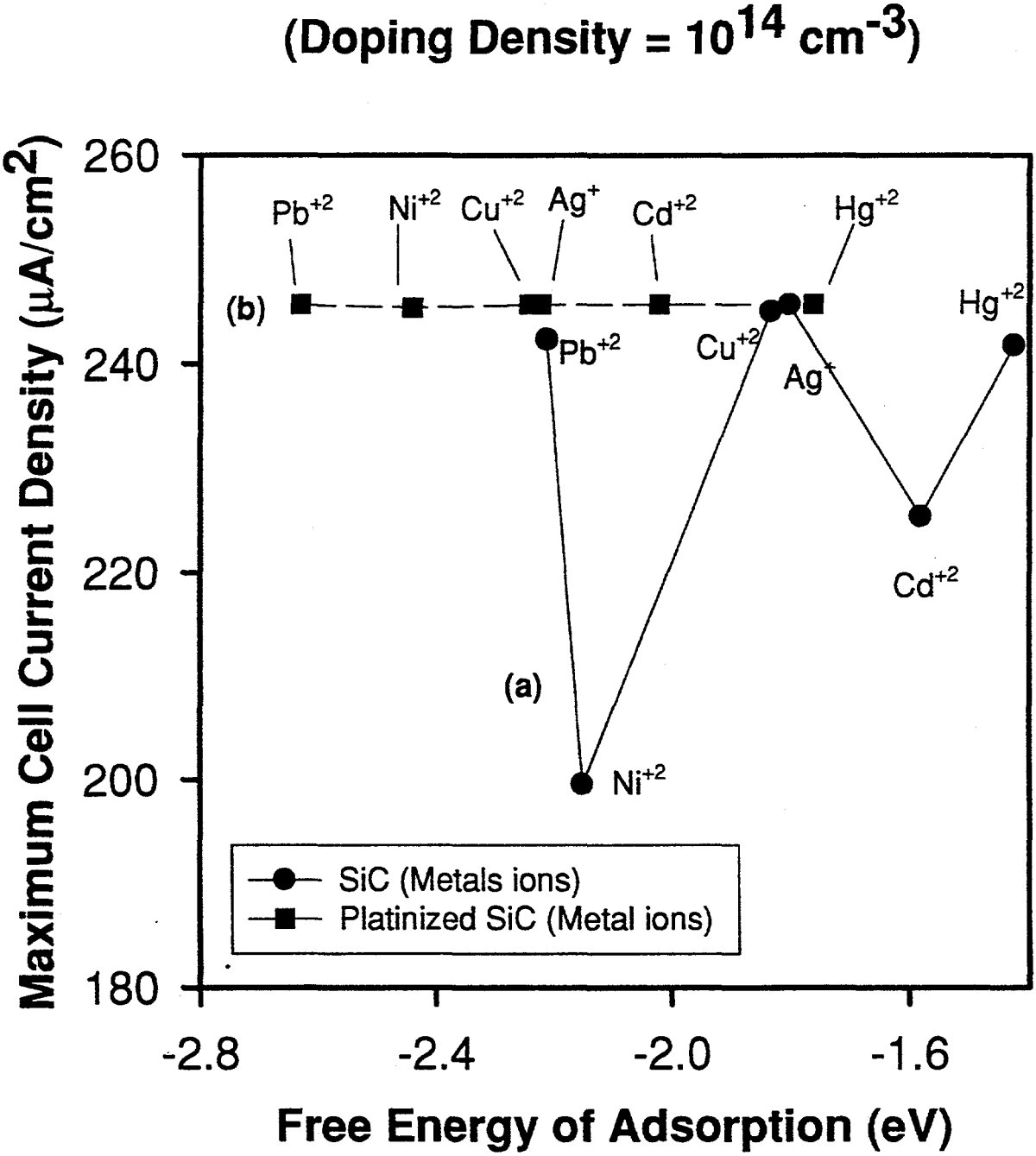

Figure 4.28

khan4.spw

SiC - Metal Ions

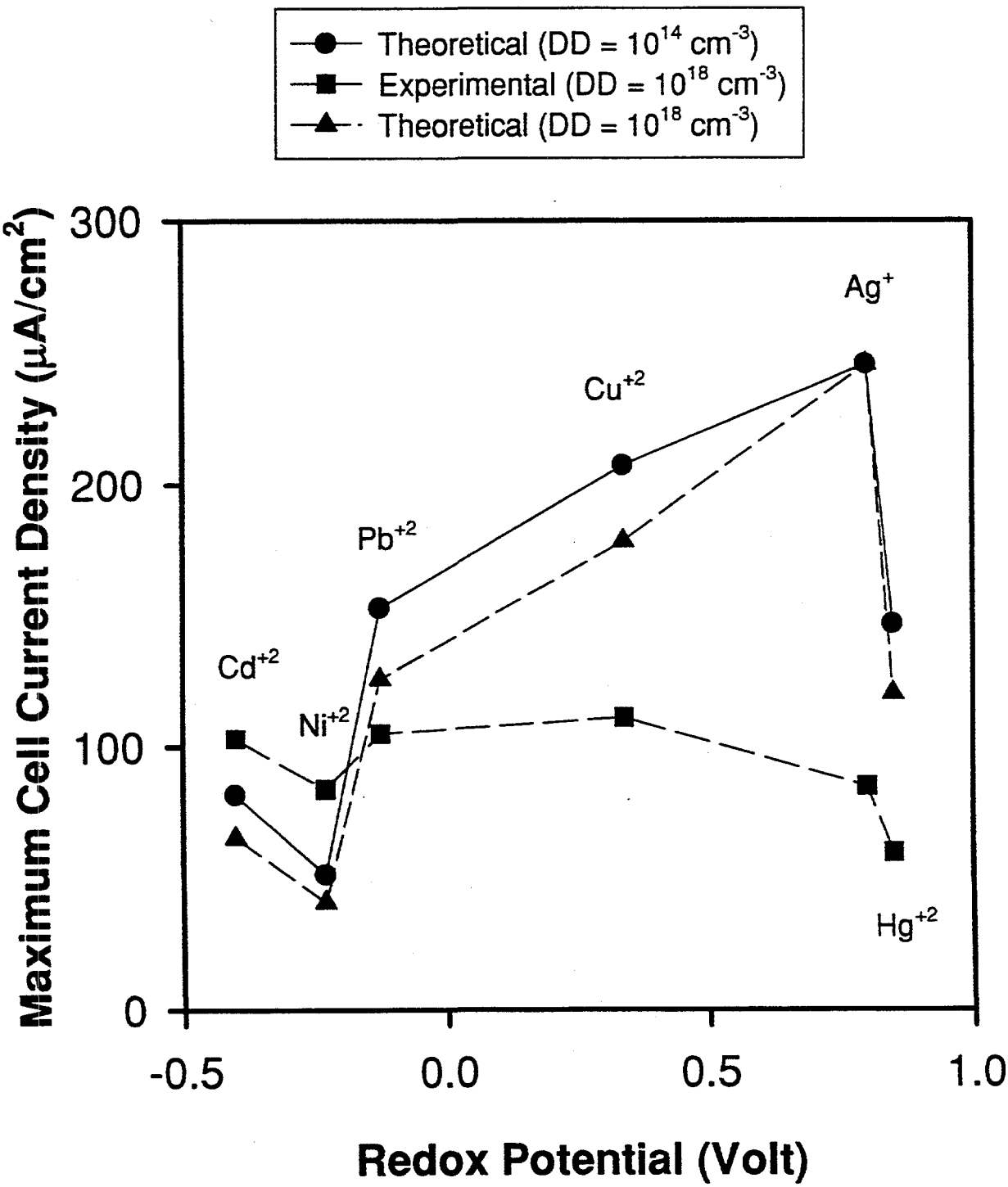

Figure 4.29

khan5a.spw

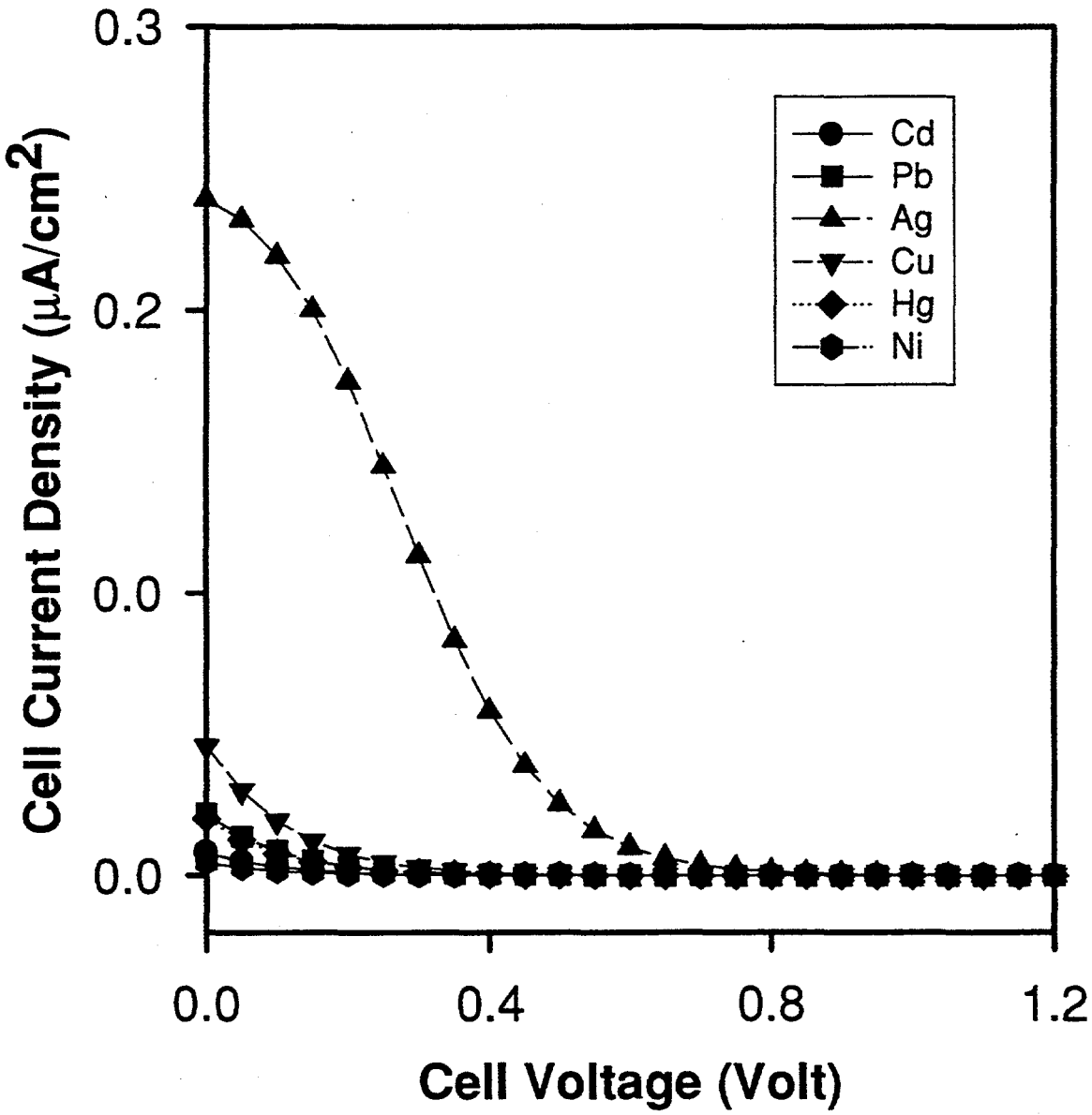

Figure 4.30(a)

khan6a.spw

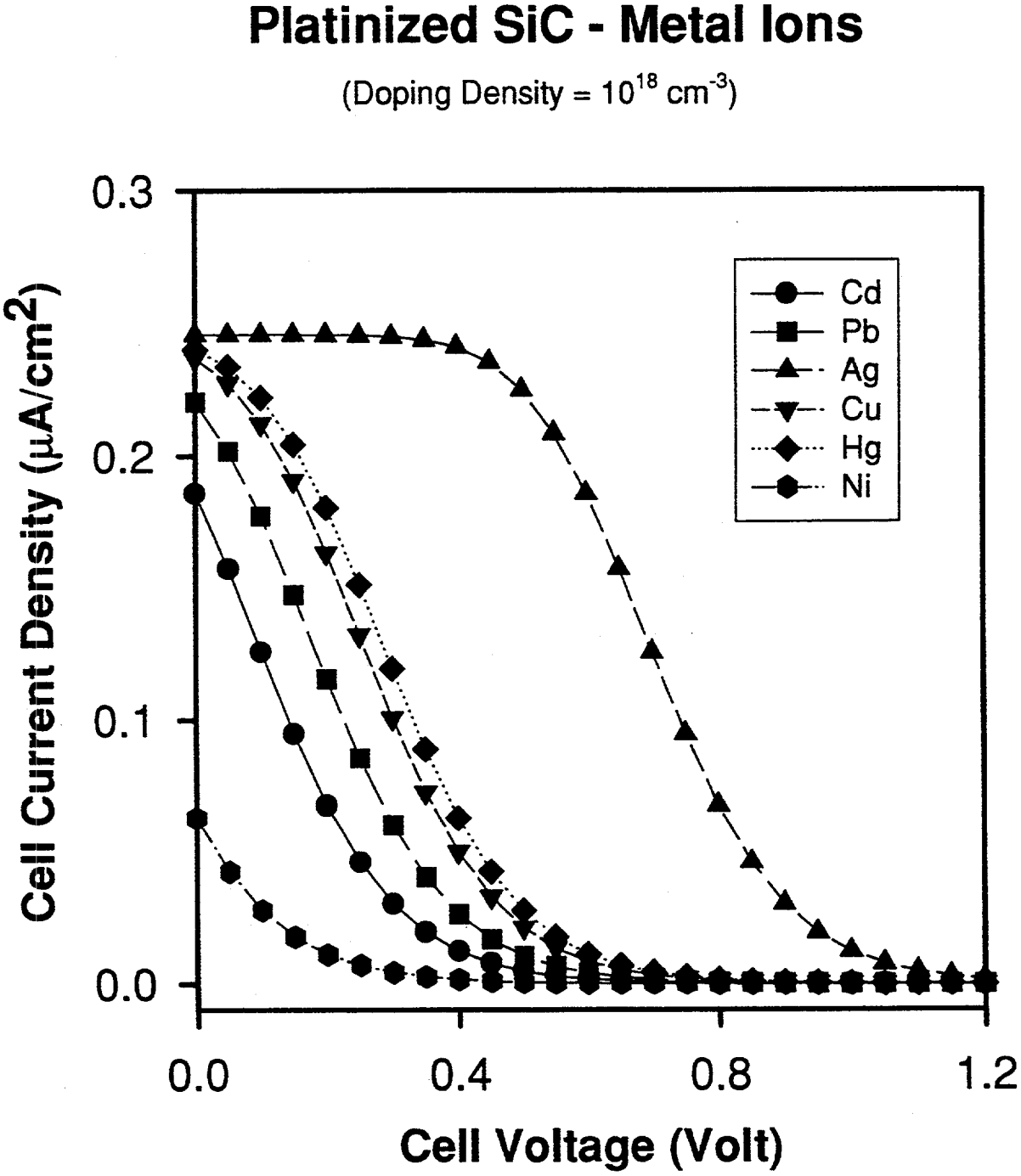

Figure 4.30(b)

khan6b.spw

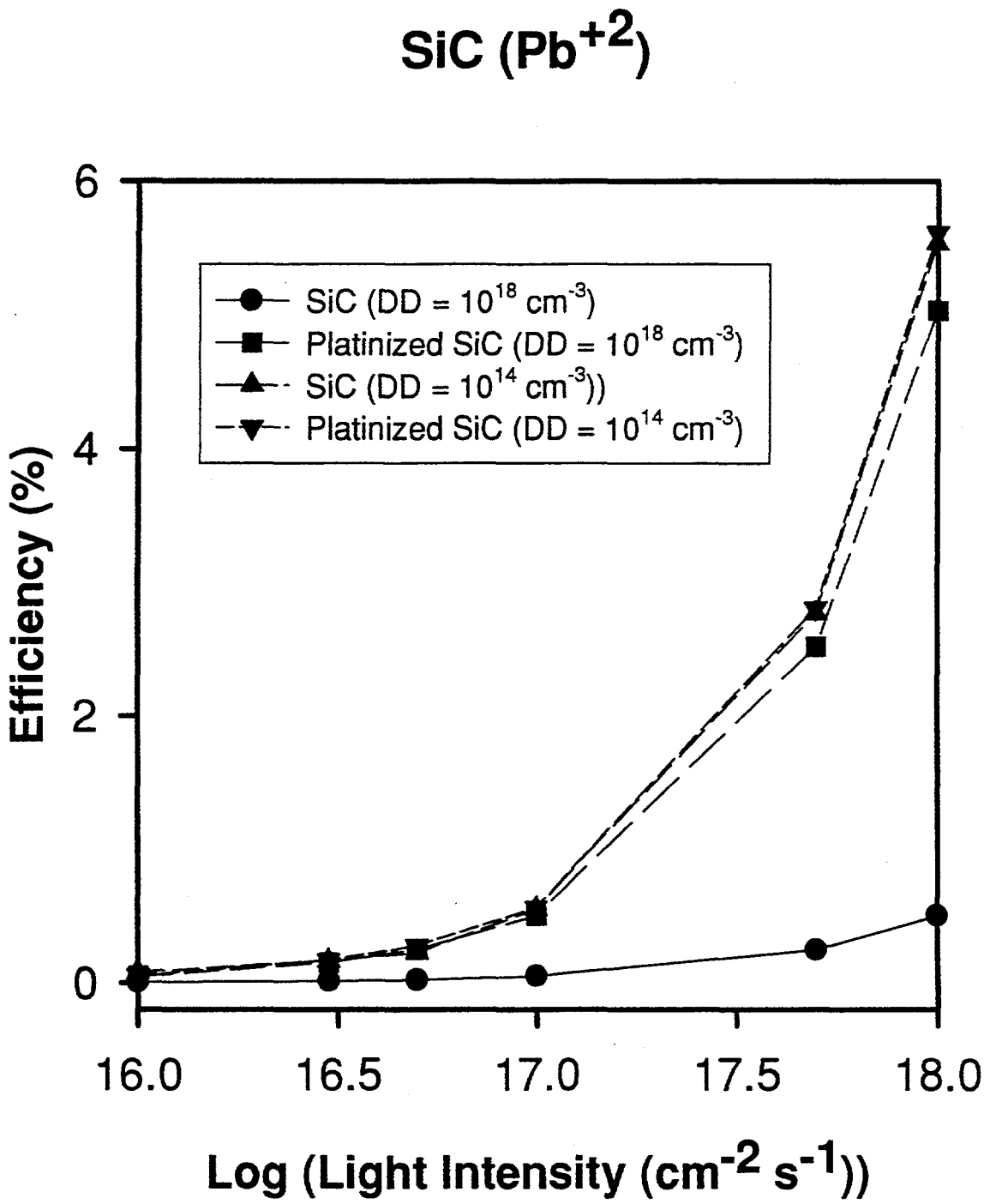

Figure 4.31

khan7.spw

4.7. References

1. Prairie, M.R.; Evans, L.R.; Stange, B.M.; and Martinez, S.L. *Environ. Sci. & Technol.* **1993.**

2. Prairie, M.R.; Pacheco, J.E.; and Evans, L.R.; In *Solar Engineering*; Stine, W.; Kreider, J; and Watanabe, K., Eds.; Am. Asso. Mech. Eng. Book No. G0656A, **1992**, 1.

3. Madden, T.H.; Considerations in the Treatment of Metal-EDTA Complexes using TiO_2 Photocatalysis, *Masters Thesis*, University of New Mexico, **1996**.

4. Foster, N.S.; Koval, C.A.; and Noble, R.D. *Environ. Sci. & Technol.* **1993**, *27*, 350.

5. Bard, A.J.; and Faulkner, L.R.; In *Electrochemical Methods*; John Wiley & Sons, Inc., New York, **1980**.

6. Mills, A.; Williums, G *J. Chm. Soc., Faraday Trans. I* **1987**, *83*, 2647.

7. Mills, A.; Green, A. *J. Photochem. Photobiol. A: Chem.* **1991**, *59*, 199.

8. Peral, J.; Mills, A. *J. Photochem. Photobiol. A: Chem.* **1993**, *73*, 47.

9. Munch, W.V.; "*Silicon Carbide*" in Landolt-Bornstein: Numerical Data and Functional Relationships in Science and Technology, Semiconductors, vol. 17a, Springer-Verlag, Berlin, Heidelberg, New York, **1982**.

10. Campbell, R.B.; Chang, H.; In *Semiconductors and Semimetals*, vol. 7, chapter 9, pp 625.

11. Landolt-Bornstein: Numerical Data and Functional Relationships in Science and technology, Semiconductors, vol. 17c, Springer-Verlag, Berlin, Heidelberg, New York, **1982**.

12. Bockris, J.O'M.; Uosaki, K. *J. Electrochem. Soc.* **1977**, *124*, 1348.

13. Morisaki, H; Ono, H.; and Yazawa, K *J. Electrochem. Soc.* **1984**, *131*, 2081.

14. Lauermann, I. *The Photoelectrochemistry of Silicon Carbide*, Ph.D. Dissertation, Solar Energy Institute, Hannover, Germany, **1994**.

15. Thewissen, D.H.M.W., Tinnemanns, A.H.A.; Eeuwhorst-Reinten, M.; Timmer, K.; and Mackor, A. *Nouveau J. de Chimie* **1982**, *7*, 73.

16. Thewissen, D.H.M.W., Tinnemanns, A.H.A.; Eeuwhorst-Reinten, M.; Timmer, K.; and Mackor, A. *Solar Energy Research and Development, Eur. Comm. Ser.* **1988**, *D2*, 58.

17. Mannivannan, A.; Fujishima, A.; and Rao, G.V.S. *Ber. Bunsenges. Phys. Chem.* **1988**, *92*, 1522.

18. Khan, S.U.M.; Bockris, J.O'M. *J.Phys.Chem.* **1984**, *88*, 2504.

19. Kainthla, R.; Khan, S.U.M.; and Bockris, J.O'M. *Int. J. Hydrogen Energy* **1987**, *12*, 381.

20. Horn, M.; Schwerdtfeger, C.F.; and Meagher, E.P. *Z. Kristallogr.* **1972**, *136*, 273.

21. Abrahams, S.C.; Bernstein, J.L. *J. Chem. Phys.* **1971**, *55*, 3206.

22. Parfitt, G.D. *Progr. in Surf. Membrane Sci.* **1976**, *11*, 181.

23. Shannon, R.D. *J. Appl. Phys.* **1964**, *35*, 3414.

24. *Gmelin Handbook of Inorganic Chemistry*, 8th edition, supplement volume B 3; Katscher, H.; Sangster, R.; and Schroder, F. Eds.; Spring-Verlag, **1986**.

25. *Gmelin Handbook of Inorganic Chemistry*, 8th edition, supplement volume B 2 (SiC), Part 1; Katscher, H.; Sangster, R.; and Schroder, F. Eds.; Spring-Verlag, **1984**.

26. Sorokin, N.D.; Tairov, Yu.M.; Tsvetkov, V.F. *Poverkhnost* **1983**, No. 5, 97; C.A. 99 [**1983**] No. 80335.

27. Hanprasopwattana, A.; Sundarajan, S.; Sault, A.G.; and Datye, A.K. *Langmuir* **1996**, *112*, 3173.

28. Rand, M.C., Greenberg, A.E., Taras, M.J., and Franson, M.A., In *Standard Methods for the Examination of Water and Wastewater*, 14th Edition, American Public Health Association, Washington, D.C., **1975**.

29. Gratzel, M.; In *Heterogeneous Photochemical Electron Transfer*; CRC Press, Inc., Boca Raton, **1989**, p101.

30. Bockris, J.O'M.; Khan, S.U.M. *Surface Electrochemistry*, Chapter 4, Plenum Press, New York, **1993**.

31. Marcus, R.A. *J. Chem. Phys.* **1965**, *43*, 697.

32. Bockris, J.O'M.; Khan, S.U.M., *Quantum Electrochemistry*, Chapter 3, Plenum Press, New York, **1979**.

33. Conway, B.E.; Bockris, J.O'M. *J. Chem. Phys.*, **1957**, *26*, 532.

34. Ruerschi, P.; Delahay, P. *J. Chem. Phys.* **1965**, 23, 556.

35. Lide, D.R., In *Handbook of Chemistry and Physics*, CRC Press, Boca Raton, **1992**.

Appendix A - Accomplishments

1. First Year - 1992

We made substantial progress in FY92 developing engineered photocatalysts for enhanced solar detoxification of polluted water. We tested two porphyrins for their ability to capture visible light and carry out detoxification reactions and demonstrated that tin uroporphyrin (SnUroP) on alumina powder effectively destroys aniline and salicylic acid. We also used molecular modeling to design porphyrins with specific binding sites and then synthesized one specific to methylene chloride (octaethyl-tetraphenyl-porphyrin). X-ray crystallography and NMR spectroscopy showed the expected binding properties and thus confirmed the molecular graphics approach to engineering photocatalysts. This work has already resulted in several conference papers and a patent disclosure on the alumina-supported uroporphyrin catalyst. Also, the project has generated interest by DuPont and Degussa for possible cooperative R&D under CRADA.

2. Second Year - 1993

Solar photocatalytic detoxification provides an attractive new approach for the treatment of polluted water. The best available technology uses a TiO_2 photocatalyst because it is active, robust, and non-toxic. Unfortunately, TiO_2 only absorbs UV light. This limits the efficiency of solar applications to the fraction of the solar spectrum which is UV, about 5%. Also, the choice of TiO_2 limits the application of photocatalysis to only a few toxic metals. This project includes development of a new generation of photocatalysts designed to enhance solar detoxification by using (1) adsorbed porphyrin dyes to effectively capture a larger portion of the solar spectrum, (2) molecular modeling techniques to design biomimetic catalysts for isolation and detoxification of dilute toxic waste components, and (3) a novel SiC/TiO_2 photocatalytic diode for extending the

applicability of photocatalysis to a much wider range of toxic metals. Some of our more important results are described below.

We have optimized the photodestruction of salicylic acid and aniline using visible light and found the best fractional coverage of tin uroporphyrin (SnUroP) on Al_2O_3 to be 0.3. The photolabile porphyrins in aqueous solution were found to be photostable on alumina for up to 500 *min in contrast to their rapid breakdown on titania.* Also, the photocatalytic activity of the SnUroP/Al_2O_3 was found to remain active upon multiple reuse cycles. We also found that SnUroP adsorbed onto alumina exhibits a quantum efficiency of 3.8% for the degradation of aniline.

We tested a variety of different supports for SnUroP and found that (1) zirconia is not a good support, (2) magnesia is effective, in particular for the degradation of chlorophenol, and (3) zinc oxide is about as good as titania. However, like titania, ZnO is a semiconductor and has the problem of degrading the porphyrin. Furthermore, we have made progress in our attempt to design porphyrins with large binding sites and have arrived at a structure that binds Paraquat, a herbicide.

In attempt to enhance our ability to remove toxic metals photocatalytically, we carried out fundamental experiments with interconnected single crystals of TiO_2 and SiC. This system serves as a vehicle for proving the concept of utilizing small particles of TiO_2 and SiC together in one complete electrochemical system. We explored the desired chemistry under very controlled conditions using a potentiostat. These experiments verified the concept and proved that light is necessary for metal reduction to occur on the SiC cathode.

A mathematical model was developed for the dual-semiconductor system. When compared with experimental results, the model was shown to describe the qualitative behavior of the system. However, refinements are required to capture its quantitative performance. Once complete, the model will be extremely useful for system optimization without the need to perform many costly experiments.

Work on utilizing TiO_2 and SiC powders was carried out concurrently with the development and testing of the single-crystal system. Sintered electrodes comparable to our single-crystals were prepared from TiO_2 and SiC powders. While the sintered TiO_2 electrodes function as hoped, the sintered SiC electrodes do not work. The causes of failure may relate to electrical contacts, internal resistance, and grain-boundary recombination. We are continuing, with the aid of the mathematical model, to investigate these possibilities. Currently, we are leaning towards the fabrication of thin-film electrodes as a stepping stone from the single-crystal model system to a practical application of the technology.

3. Third Year - 1994

Solar photocatalytic detoxification provides an attractive new approach for the treatment of polluted water. The best available technology uses a TiO_2 photocatalyst because it is active, robust, and non-toxic. Unfortunately, TiO_2 only absorbs UV light. This limits the efficiency of solar applications to a fraction of the solar spectrum, approximately 5%. Also, the choice of TiO_2 limits the application of photocatalysis to only a few toxic metals. This project includes development of a new generation of photocatalysts designed to enhance solar detoxification by using (1) adsorbed porphyrin dyes to effectively capture a larger portion of the solar spectrum, (2) molecular modeling techniques to design biomimetic catalysts for isolation and detoxification of dilute toxic waste components, and (3) a novel SiC/TiO_2 photocatalytic diode for extending the

applicability of photocatalysis to a wider range of toxic metals. Some of our important results are described below.

In addition to using titania and alumina as supports for enhanced photoactivity of SnUroP, we have also used magnesia and manganese dioxide to stabilize and immobilize this dye which showed photocatalytic properties in homogeneous solutions. Although manganese dioxide showed no activity as a support, magnesia was quite effective specifically for the photoassisted removal of chlorophenol and salicylic acid. Unfortunately, it was discovered that the removal of these target molecules was mostly due to photoassisted adsorption onto magnesia. Porphyrins were degraded on titania because of its inherent semiconducting nature, whereas alumina was found to be the most suitable support for photolabile porphyrins. On alumina, photocatalytic properties were enhanced for photodegradation of salicylic acid and photopolymerization, hence efficient removal, of aniline. Furthermore, we have made progress in our attempt to design porphyrins with large binding sites. Accordingly, a water-soluble octaacetic-acid-tetraphenylporphyrin and its derivatives have been synthesized and characterized using spectroscopic techniques.

In an attempt to understand and thus enhance our ability to remove toxic metals photocatalytically, we carried out fundamental kinetic experiments using SiC aqueous suspensions and methyl orange as a probe. We found that etching SiC with 50% HF solution for a period of two hours was necessary before any photoreduction was possible on SiC surface. Investigation of SiC powders with transmission electron microscopy confirmed that the HF treatment removed an amorphous SiO_2 layer from the surface. Among three commercially available and three specially made SiC powders materials, Carbolon-manufactured SiC was found to be the most active. The initial rate of photoreduction of methyl orange (to hydrazine) was found to decrease with

increasing pH (for the range 4.4 - 9.0) of aqueous suspensions. This observation could be related to the relative unavailability of a specific form of methyl orange at higher pH. The photoreduction of methyl orange by SiC was slower by an order of magnitude than that by TiO_2. However, we have successfully used SiC powder to remove chromium metal from aqueous solution when Na_2EDTA was used as a hole scavenger. These observations indicate that the redox processes on SiC probably follow similar steps as observed previously on TiO_2.

Electrochemical experiments were carried out on both the unpassivated Si- and C-faces of p-type SiC crystals, and C-faces were passivated against oxide formation. These experiments demonstrated that the unpassivated SiC electrodes have greater stability than was previously recognized. This observation was encouraging because the passivating layers were found to reduce the open circuit voltage of SiC electrodes and thus turned them inactive and unstable. Experiments with cyclic voltammetry between -1V and +1V identified photooxidation and photoreduction peaks when redox species were present in the electrolyte solution. However, the results could not be used for quantitative analyses because of the problems encountered with reproducibility of data. All of the metal-sputtered (Au, Pt, Ag and Ti) SiC electrodes seemed to lose their coatings after repeated uses. It may have been the degradation of these coatings which appeared as oxidation currents in the plots rather than the oxidation of metals plated from solution. Photoelectrochemical experiments using cyclic voltammetry with gold-sputtered SiC confirmed a direct dependence of reduction current on photon intensity.

A mathematical model was developed for a dual-semiconductor photoelectrochemical system using p-SiC and n-TiO_2. When compared with experimental results, the model was shown to describe the qualitative behavior of the system. For the refinements of this mathematical model, the semiconducting parameters of p-SiC photocathode (thin film) were optimized for a

photoelectrochemical cell (PEC) in conjunction with unaltered conditions of n-TiO_2 photoanode (thin film). This model was developed to optimize the efficiency of photoreduction of metal ions present in polluted water. The model indicates that dopant density of SiC plays a crucial role in dictating the maximum cell current of the PEC. Also, the model predicts that platinized SiC may be very efficient for removing metal ions from polluted water. A cell efficiency of ~6% was calculated for removing lead from an aqueous solution when the UV light flux was 10^{18} photons cm^{-1} s^{-1}.

A composite TiO_2/SiC material was prepared by thermal deposition of TiO_2 from an ethanolic solution of titanium isopropoxide onto SiC powder (as received). The photoreduction rate of methyl orange by this composite was slower by an order of magnitude when compared to those by TiO_2 powders, P-25 and Tioxide grades. This photoactivity by TiO_2/SiC may be attributed solely to TiO_2 particles on the surface and the observed low photoreduction rate is due to low surface coverage of TiO_2 (less than 0.5) on SiC. A synthesis of a similar composite is currently underway but using HF-etched SiC.

In summary, we have completed a wide array of both theoretical and experimental studies to design and use large bandgap ($\geq$ 3 eV) semiconductor-based photocatalytic systems. We have also tested dyes like metalloporphyrins to utilize the visible photons which are the most abundant in the sun light. We have successfully demonstrated the photocatalytic ability of unpassivated SiC to reduce a simple model compound methyl orange and also to remove chromium metal from aqueous solution. A composite of TiO_2/SiC was synthesized which will lead to a new generation of photocatalysts. On the basis of the Computer Aided Molecular Design, a water-soluble octaacetic-acid-tetraphenylporphyrin and its derivatives with large binding sites have been synthesized and these porphyrins were characterized using spectroscopic techniques. The

fundamental information gathered from this project is expected to lead to significant advances in important areas of photocatalysis.

Appendix B - Impacts

1. List of Publications and Presentations Resulting from the Project

1. M Miura, S.A. Majumder, J.D. Hobbs, M.W. Renner, L.R. Furenlid, and J.A. Shelnutt, Synthesis and Spectroscopic characterization of octaacetic acid tetraphenylporphyrins, *Inorganic Chemistry 33*, 6078, 1994.

2. S.A. Majumder, Environmental Effects on Structure-Function Relationships in Metalloporphyrin-Based Catalytic Systems, *Ph.D. dissertation*, University of New Mexico, February 1994.

3. S.A. Majumder, M.R. Prairie, M.R. Ondrias, and J.A. Shelnutt. *Enhancement of Solar Photocatalytic Detoxification by Adsorption of Porphyrins onto* TiO_2. In Solar Engineering, W. Stine, J. Kreider, and K. Watanabe, Eds. Book No. G0656A-1992, American Society of Mechanical Engineers (1992).

4. M.R. Prairie, S.A. Majumder, L.R. Evans, S.L. Martinez, and J.A. Shelnutt, Recent Developments in Solar Photocatalysis for Water Detoxification, *Proceeding of the Annual Meeting of the American Institute of Chemical Engineers,* Miami Beach, Florida, Nov. 1-6, 1992.

5. S.U.M. Khan, B. Craig, M.R. Prairie, and J.E. Miller, A Model of a Dual-Semiconductor Photocatalytic System for Detoxification of Polluted Water, presented at *Electrochemical Society National Meeting*, San Francisco, CA, May 22-27, 1994

6. S.A. Majumder, M.R. Prairie, G.N. Ryba, M.R. Ondrias, and J.A. Shelnutt, Photocatalytic Degradation of Aromatic Compounds by Porphyrins Adsorbed onto Al_2O_3 using Visible Light, *manuscript in preparation.*

7. S.A. Majumder, X. Song, M. Miura, J.D. Hobbs, and J.A. Shelnutt, Resonance Raman Studies of Nickel Octaacetic-Acid-Tetraphenylporphyrins and its Derivatives, to be presented *at the 14th International Conference on Raman Spectroscopy*, Hong Kong, August 22-26, 1994.

8. S.A. Majumder, M. Miura, J.D. Hobbs, and J.A. Shelnutt, Aggregation and Complexation Properties of Nonplanar Water-Soluble Octaacetic Acid-Tetraphenylporphyrin, presented at the *38th Biophysical Society Annual Meeting*, New Orleans, LA, March 6-10, 1994.

9. Annual Summer Meeting of the AIChE, Seattle, WA, August 16-19, 1993.

10 S.A. Majumder, G.N. Ryba, M.R. Prairie, M.R. Ondrias, and J.A. Shelnutt, Visible light-initiated photocatalytic detoxification of salicylic acid and aniline by adsorption of porphyrins onto Al_2O_3, presented at the *International Waste Management Conference*, San Juan, P.R., May 1-2, 1993.

11. M. Miura, S.A. Majumder, J.D. Hobbs, M.W. Renner, and J.A. Shelnutt, Resonance Raman Studies of Octaacetic Acid-Tetraphenylporphyrins, presented *at the American Chemical Society National Meeting*, Chicago, IL, August 22-26, 1993.

12. S.A. Majumder, M.R. Prairie, M.R. Ondrias, and J.A. Shelnutt, Photocatalytic Degradation of Aromatic Compounds by Porphyrins Adsorbed onto Al_2O_3 using Visible Light, *presented at the 1992 Waste Management and Environmental Restoration Conference*, San Juan, Puerto Rico, April 9-11, 1992.

13. S.A. Majumder, M.R. Prairie, M.R. Ondrias, and J.A. Shelnutt, Photocatalytic Degradation of Salicylic Acid by Porphyrins Adsorbed onto Al_2O_3 using Visible Light, *presented at the American Chemical Society National Meeting*, San Francisco, California, April 7-10, 1992.

2. List of Invention Disclosures Resulting from the Project

1. S.A. Majumder, J.A. Shelnutt, M.R. Prairie, and M.R. Ondrias, Photocatalytic degradation of aromatic compunds by metalloporphyrins adsorbed onto Al_2O_3 using visible light, SD-113; S-75,556, March 1992.

2. J.A. Shelnutt, S.A Majumder, and M.R. Prairie, Enhancement of solar photocatalytic detoxification by adsorption of porphyrins onto TiO_2 substrates, SD-4989, S-74,101, May 1991.

3. List of Patents Resulting from the Project

1. S.A Majumder, J.A. Shelnutt, M.R. Prairie, and M.R.Ondrias, Photocatalytic conversion of substances using organo-metallic dyes and light, U.S. Patent Application Serial No. 08/042,275, April 1993.

4. List of Copyrights (for Software) Resulting from the Project

N/A

5. Information Regarding Employee Recruitment as a Result of the Project

Number of Postdocs:

One half time (Gail Ryba, 6211), 1993.

One part time (Steve Showalter, 6211), 1994.

One full time (Sabir A. Majumder, 6216), 1994 and 1995.

Number of Professors:

One faculty member on a fellowship at Sandia (Shahed U.M. Khan, Duquesne University, funded by AWU) for the Summer, 1993. Professor Khan was supported also for the Summer, 1994 for his work at Duquesne University.

Number of permanent staff hired:

None.

6. Information Regarding Involvement of Students in the Project

One graduate student at Univ. of New Mexico, NM (Sabir A. Majumder), 1992-94.

Two undergraduates on summer appointments at Sandia (Bradley Craig and Ivelisse Colon Perez), 1993.

One graduate student for the Summer at Duquesne University, PA (William B. Ingler), 1994.

Two undergraduates on summer appointments at Sandia (Ivelisse Colon Perez and Donna Waters), 1994.

7. Information Regarding Follow-On Work (New Activities, Projects, Sponsors)

A CRADA is being developed with DuPont on the kinetic modeling that was originated during this project. This work is funded by DOE (EE-222).

Distribution

Dr. Abhaya K. Datye
Department of Chemical Engineering
University of New Mexico
Albuquerque, NM 87131

Dr. Shahed U.M. Khan
Department of Chemistry and Biochemistry
Duquesne University
Pittsburgh, PA 15282

U.S. Department of Energy
Attn: Frank Wilkins, EE-11
1000 Independence Avenue SW
Washington, DC 20585

National Renewable Energy Laboratory
Attn: Dan Blake
1617 Cole Boulevard
Golden, CO 80401-3393

National Renewable Energy Laboratory
Attn: Tom A. Williams
1617 Cole Boulevard
Golden, CO 80401-3393

MS 0188	Chuck E. Meyers, 4523 (2)
MS 0188	Donna L. Chavez, 4523 (2)
MS 0702	Dan E. Arvizu, 6200
MS 0703	Craig E. Tyner, 6216
MS 0703	Michael R. Prairie, 6216 (2)
MS 0703	Sabir A. Majumder, 6216 (3)
MS 0709	Tina Nenoff, 6212
MS 0710	Gail N. Ryba, 6211
MS 0710	Gary A. Carlson, 6211
MS 0710	James E. Miller, 6211
MS 0710	John A. Shelnutt, 6211
MS 0749	Alan P. Sylwester, 6203
MS 1127	James E. Chavez, 6215
MS 1349	Terry J. Garino, 1846
MS 0899	Technical Library, 4414 (5)
MS 9018	Central Technical Files, 8523-2
MS 0619	Review & Approval Desk, 12630 (2) For DOE/OSTI